UC Berkeley
UC Berkeley Electronic Theses and Dissertations

Title
Manipulating 1D Conduction Channels; from Molecular Geometry to 2D Topology

Permalink
https://escholarship.org/uc/item/09z5w3jz

Author
Pedramrazi, Zahra

Publication Date
2019

Peer reviewed|Thesis/dissertation

eScholarship.org Powered by the California Digital Library
University of California

Manipulating 1D Conduction Channels; from Molecular Geometry to 2D Topology

by

Zahra Pedramrazi

A dissertation submitted in partial satisfaction of the

requirements for the degree of

Doctor of Philosophy

in

Physics

in the

Graduate Division

of the

University of California, Berkeley

Committee in charge:
Professor Michael F. Crommie, Chair
Professor Feng Wang
Professor Jeffrey Bokor

Spring 2019

Manipulating 1D Conduction Channels; from Molecular Geometry to 2D Topology

Copyright 2019
by
Zahra Pedramrazi

Abstract

Manipulating 1D Conduction Channels; from Molecular Geometry to 2D Topology

by

Zahra Pedramrazi

Doctor of Philosophy in Physics

University of California, Berkeley

Professor Michael F. Crommie, Chair

This dissertation is divided into two segments, both of which focus on creating and manipulating one-dimensional (1D) conduction channels in novel 1D and two-dimensional (2D) systems, characterized by scanning tunneling microscopy (STM).

The first half describes how the electronic properties of quasi-1D graphene nanoribbons (GNRs) are manipulated by controlling their width and edge geometry at the atomic scale. A bottom-up approach is used for fabricating three different armchair GNR (AGNR) systems, allowing the geometry and hence the electronic properties of resultant AGNRs to be controlled. Successful molecular bandgap engineering in 1D AGNR heterojunctions is described, as well as the electronic and topographic characterization of the concentration dependence of boron-doped AGNRs. The discovery of two new in-gap dopant states with different symmetry is described. The successful fabrication and characterization of S-AGNRs having sulfur atoms substitutionally doped at the AGNR edges is also described. Our results indicate that S-doping induces a rigid shift of the energies for both the valence and conduction bands.

The second half of this thesis describes how the 1T’ phase of monolayer transition metal dichalcogenides (TMDs) can be used as a platform to create 2D topological insulators (TIs). These novel TI systems are characterized in great detail. The successful growth and characterization of single-layer 1T’–WTe_2 is described. This material is shown to host a bulk bandgap and helical edge states at the 1T’–vacuum interface. The growth and characterization of mixed phase-WSe_2 is described. New techniques for creation and manipulation of edge conduction channels at interfaces between materials of different topologies are described.

تقدیم به این پنج نفر

Contents

Contents iii

List of Figures vi

List of Abbreviation viii

1 Introduction

1.1 Graphene Nanoribbons
1.1.1 Theory of Graphene Nanoribbons……………………………………..….1
1.1.2 Bottom-up Approach……………………………………………………..3

1.2 Topological Insulators
1.2.1 Topology...………...……………………………………………………...5
1.2.2 Topologically Trivial and Non-Trivial…………………………………....5
1.2.3 Quantum Spin Hall Insulator……………………………...………....7
1.2.4 QSH, Previous Experimental Realizations………………………….…..8
1.2.5 TMDs as a Platform……………………………………………….…8

2 Scanning Tunneling Microscopy

2.1 Quantum Tunneling Theory of STM……………………………………………11
2.2 Basic Principles of STM…………………………………………………...……14
2.3 Deposition Methods……………………………………………………………..16

3 Graphene Nanoribbon Projects

3.1 Molecular Bandgap Engineering in 7-13 Armchair GNR Heterojunction
3.1.1 Motivation.…………………………………………………………...….....22
3.1.2 Bottom-up Synthesis and Local Characterization of Electronic States……………………………………………...……21
3.1.3 Theoretical Calculations and Comparison to Experimental Results……………………………………...……….25
3.1.4 Discussion of the Height Dependence of the Electron Potential Energy…………………………………………………….....27
3.1.5 Conclusion……………………….…...…………...…………….……....29

3.2 Concentration Dependence of Dopant Electronic Structure in Bottom-up Graphene Nanoribbons
3.2.1 Abstract………………………..……………….....……………….………30
3.2.2 Freestanding Calculation…………………...…………….……….......31
3.2.3 Synthesis and Characterization of B-doped AGNRs with Different Dopant Concentrations……………..…………………………………33

3.2.4 Symmetry-Dependent Hybridization between the Dopant States and Au(111) Substrate……………..……………………………………...38
3.2.5 Conclusion………………………………..……………………...42

3.3 Bottom-up Synthesis on N=13 Sulfur-Doped Graphene Nanoribbons
3.3.1 Abstract……………………..………………...……………………44
3.3.2 Bottom-up Synthesis and STM Characterization of Local Electronic states……………………………..……...………...44
3.3.3 Theoretical Calculations and Comparison to Experimental Results……………………………………..…………………47
3.3.3.1 Computational Methods…………………..………………....48
3.2.5 Conclusion…........………………………...……..………..……….…..49

4 Quantum Spin Hall Insulator Projects

4.1 Quantum Spin Hall State in Monolayer 1T'–WTe_2
4.1.1 Introduction…………………………………..…….……….....….…51
4.1.2 Topological Phase of 1T'–WTe_2………………..……….……….....….…51
4.1.3 Growth and Surface Characterization…………..……....…………......…..52
4.1.4 Polarization Dependent ARPES……………...………....…….………….54
4.1.5 Electronic Structure Characterization of Bulk and Edge....…....…………56
4.1.6 Conclusion………………………………………………...……….....59

4.2 Observation of Topologically Protected States at Crystalline Phase Boundaries in Single-Layer WSe_2
4.2.1 Introduction…………………………………………….…….......….…61
4.2.2 Structural Characterization of Single-layer 1T′–WSe_2………..…..….....61
4.2.3 Electronic Characterization of Single-layer 1T′–WSe_2…...………..........65
4.2.4 Density Functional Theory Calculations and Comparison with the Experiments…….……………………….……..……………...…..69
4.2.5 Conclusion……………………………………………………......……71

4.3 Manipulating Topological Domain Boundaries in the Single-layer Quantum Spin Hall Insulator 1T'–WSe_2
4.3.1 Introduction…………………………………………….…………...…73
4.3.2 STM Manipulation to Create Domain Boundaries in 1T'–WSe_2…......…74
4.3.3 Evidence for Ferroelasticity…………………………………………...75
4.3.4 Electronic Characterization of 120° 1T'/1T' Domain Boundaries...……77
4.3.5 Density Functional Theory Calculations and Comparison with the Experiments……………………………………………………….....80
4.3.6 Theoretical and Experimental Characterization of 60° and 0° 1T'/1T' Domain Boundaries…………………………...……….……….....81
4.3.7 Non-Trivial and Trivial Two-Channel System……………………...…....85
4.3.8 Conclusion……………………………………………………………..86

Bibliography **87**

List of Figures

1.1 Electronic dispersion for graphene nanoribbons
1.2 The different band gaps of Na-AGNRs as a function of width.
1.3 Calculated LSDA band structure of a 12- ZGNRs
1.4 Reaction scheme of N=7 AGNRs.
1.5 Materials of different topologies.
1.6 Edge state of QH and QSH.
1.7 Atomistic structures of monolayer TMDs of the three different phases.
1.8 Structural stability of monolayer 1T'–MX_2
1.9 Different topological domain boundaries.
2.1 Schematic of STM tunnel junction.
2.2 Diagram of basic STM set-up.
2.3 Schematics of evaporators.
2.4 Schematic of leak-valve deposition set-up.
3.1 Bottom-up synthesis of 7–13 GNR heterojunctions.
3.2 STM dI/dV spectroscopy of 7–13 GNR heterojunction electronic structure.
3.3 Comparison of experimental dI/dV maps and theoretical LDOS for a 7–13 GNR heterojunction.
3.4 Theoretical electronic structure of 7–13 GNR heterojunction.
3.5 Height dependence of the electron potential energy.
3.6 Band structure evolution of freestanding boron-doped N = 7 armchair graphene nanoribbons at different dopant densities.
3.7 Calculated wavefunctions of dopant states.
3.8 Molecular precursors used in boron doped study.
3.9 Electronic structure of a dilute boron-doped N = 7 AGNR on Au(111).
3.10 Electronic structure of densely boron-doped N = 7 AGNR on Au(111).
3.11 DFT-LDA calculation of dilute-doped N = 7 GNR on Au(111) substrate.
3.12 DFT-LDA calculation of densely doped N = 7 GNR on Au(111) substrate.
3.13 Wavefunctions of States A and B of the densely-doped GNR.
3.14 Bottom-up synthesis N=13 sulfur-doped AGNR.
3.15 STM dI/dV spectroscopy of S-13-AGNRs.
3.16 Theoretical electronic structure of S-13-AGNRs.
4.1 Topological phase transition in 1T'–WTe_2.
4.2 Characterization of epitaxially grown 1T'–WTe_2 and overall electronic structure from ARPES.
4.3 Polarization dependent ARPES.
4.4 Bandgap opening in monolayer 1T'–WTe_2.
4.5 Tunneling spectroscopy in the bulk and at the edge of 1T'–WTe_2.
4.6 Determining the bulk gap size from STS.
4.7 Continuous edge states on irregularly shaped edges.
4.8 Atomic structure of mixed-phase single-layer WSe_2.
4.9 ARPES characterization of single-layer 1T′–WSe_2.

4.10 STS characterization of single-layer mixed-phase WSe_2.
4.11 Quasiparticle interference patterns in single-layer 1T′–WSe_2.
4.12 Spatial extent of atomically well-ordered 1D interface state in single-layer 1T′–WSe_2.
4.13 WSe_2 1T′–1H interface electronic structure.
4.14 STM tip-induced structural change in monolayer 1T'–WSe_2.
4.15 Reversibility of 1T'/1T' domain formations.
4.16 1T' to 1H phase transition.
4.17 Structural and electronic properties of a 120° 1T'/1T' domain boundary.
4.18 Comparison of electronic properties of 120° 1T'/1T' domain boundary and 1T'/1H boundary coexisting in single-layer WSe_2.
4.19 Band Structure of 1T'/vacuum and 120° 1T'/1T' domain boundaries in single-layer WSe_2.
4.20 Structural and electronic properties of the 60° and 0° domain boundaries.
4.21 Position-dependent STS of 0° 1T'/1T' domain boundary in single layer 1T'–WSe_2.
4.22 Calculated band structures for 60° and 0° 1T'/1T' domain boundaries in single-layer WSe_2.
4.23 Trivial/topological two-channel system.

List of Abbreviations

AGNR	Armchair Graphene Nanoribbons
ARPES	Angle-Resolved Photoemission Spectroscopy
BLG	Bilayer Graphene
BZ	Brillouin Zone
CB	Conduction Band
DB	Domain Boundaries
DFT	Density Functional Theory
dI/dV	Differential Conductance
DOS	Density of States
E-Beam	Electron Beam
EDC	Energy Distribution Curves
FFT	Fourier Transform
FS	Fermi Surface
GNR	Graphene Nanoribbons
h-BN	Boron Nitride
LDA	Local Density Approximation
LDOS	Local Density of States
LSDA	Local Spin Density Approximation
MBE	Molecular Beam Epitaxy
MIGS	Metal-Induced-Gap-States
ML	Monolayer
NEGF	Non-Equilibrium Green's Function Method
PBE	Perdew-Burke-Ernzerhof
PDOS	Partial Density of States
QCM	Quartz Crystal Microbalance
QPI	Quasiparticle Interference
QH	Quantum Hall
QHE	Quantum Hall Effect
QSH	Quantum Spin Hall
QSHI	Quantum Spin Hall Insulator
RHEED	Reflection High-Energy Electron Diffraction
RT	Room Temperature
SOC	Spin-Orbit Coupling
STM	Scanning Tunneling Microscopy or Scanning Tunneling Microscope
STS	Scanning Tunneling Spectroscopy
TB	Tight-Binding
TI	Topological Insulator
TMD	Transition Metal Dichalcogenides
UHV	Ultra-High Vacuum

VB	Valence Band
ZGNR	Zigzag Graphene Nanoribbons
1D	One-Dimensional
2D	Two-Dimensional
3D	Three-Dimensional

Chapter 1. Introduction

1.1 Graphene Nanoribbons

Advances in technology have resulted in a significant decrease in the size of devices, leading to increased demand for techniques to manipulate and fabricate materials in the nanoscale regime. Structural and electronic fine-tuning at the single nm scales however, has proven to be very challenging experimentally. The first challenge is to find a material that hosts useful electronic properties at small scales and the next challenge is to find a technique that can controllably manipulate the structural and electronics properties of such a material. Bottom-up synthesis of graphene nanoribbons (GNRs) is one possible answer to these challenges.

1.1.1 Theory of Graphene Nanoribbons

GNRs are one-dimensional (1D) narrow strips of graphene whose electronic properties strongly depend on their width and edge structures.[1-11] The two highest symmetry edge structures are zigzag and armchair edges. Fig. 1.1a shows a honeycomb lattice having zigzag edges along the x-direction and armchair edges along the y-direction. GNRs with zigzag edges (ZGNRs) are finite in y but extend along the x-direction, while GNRs with armchair edges (AGNRs) are finite in x but extend along the y-direction.

The electronic properties of GNRs can be modeled by the tight-binding (TB) approximation while imposing appropriate boundary conditions. TB predicts that the electronic properties of AGNRs will strongly depend on their widths (they can be metallic or semiconducting),[1-5] while ZGNRs of all widths are metallic with edge states residing on both sides.[1-10] The result of such TB calculations is presented in Figs. 1.1b-c. However, more detailed *ab initio* calculations of GNRs with hydrogen-passivated edges show that both zigzag and armchair edge geometries always possess nonzero, direct bandgaps. The origins of these bandgaps for different edge geometries are different, which will be explained later.

For both first-principles calculations and TB, AGNRs can be classified into three distinct families: $N_a = 3p$, $3p+1$ and $3p+2$, where N_a is the number of dimer lines and p is a positive integer. First-principles calculations using the local density approximation (LDA) and TB calculations agree that for 3p and 3p+1 AGNRs families that the bandgap of each N_a-AGNR is inversely proportional to its width as shown in Fig. 1.2.[12, 13] For the 3p+2 family however, TB calculations predict the AGNRs to be metallic, while DFT predicts they are semiconducting. LDA calculations carried on hydrogen-passivated armchair edges predict a considerable change in the on-site energy and bonding distance of the edge carbon atoms. These edge effects play an important role and open a bandgap in the electronic structure of 3p+2 AGNRs, the origin of their semiconducting behavior. Hence, first-principles calculations predict that AGNRs are always semiconducting with bandgaps originating from quantum confinement and edge reconstruction.

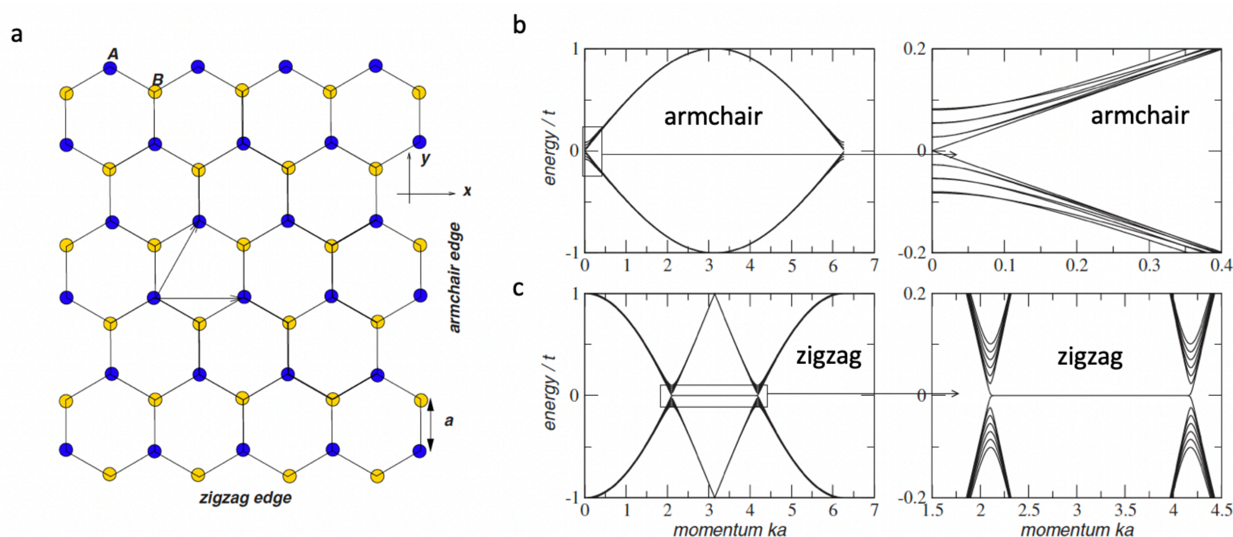

Figure 1.1 | Electronic dispersion for graphene nanoribbons. a, A honeycomb lattice displays both zigzag and armchair edges. b-c, Left: energy spectrum calculated through TB for a nanoribbon with armchair (b) and zigzag (c) edges. The nanoribbon width is N=200. Right: close-up of the low energy states shown on the right. (Figure is reproduced with permission from ref. 12)[12]

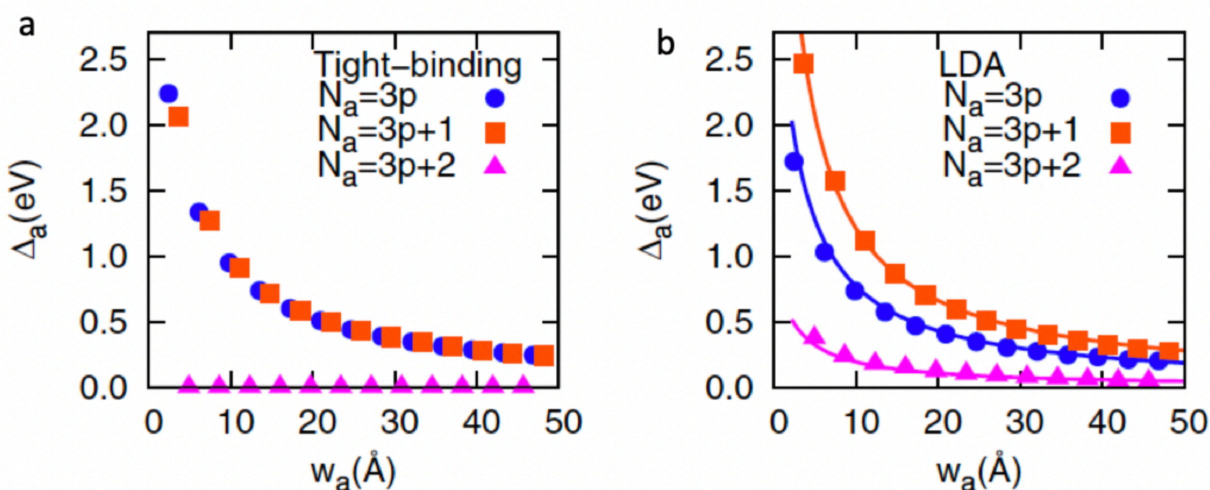

Figure 1.2 | The different band gaps of Na-AGNRs as a function of width. a, TB calculations with t=2.70 eV and b, first-principles calculations. (Figure is reproduced with permission from ref. 13)[13]

First-principles calculations of ZGNRs that include the spin degree of freedom (i.e. the local spin density approximation (LSDA)) predict the opening of a bandgap in their band structure for a different reason (Fig. 1.3).[13, 14] Unlike AGNRs, this bandgap is due to spin-ordered states at the edges that create a staggered sublattice potential.[13-15] Moreover, the two

edges of a ZGNR are predicted to exhibit antiparallel spin orientations resulting in a magnetic insulating ground state.

Additional first-principles calculations performed within the GW approximation predict that the quasiparticle band gaps of both AGNRs and ZGNRs have significant self-energy corrections. These theoretical studies predict that GNRs host a wide range of electronic and magnetic properties (from semiconductors to magnetic edge states) governed by edge geometry and width, making them uniquely desirable for future nanoscale devices.[13-15]

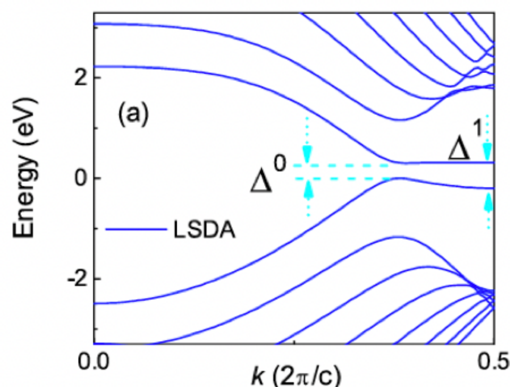

Figure 1.3 | Calculated LSDA band structure of a 12- ZGNRs. The up and down spin states are degenerate for all the bands, and the top of the valence band is set to zero. The symbols Δ_0 and Δ_1 denote the direct band gap and the energy gap at the zone boundary $kd_z = \pi$. (Figure is reproduced with permission from ref. 15).[14, 15]

1.1.2 Bottom-Up Approach

A prerequisite for future GNR applications is the ability to controllably manipulate their electronic properties. Such control requires the development of fabrication tools capable of precisely manipulating their width and edge geometries at the atomic scale, as well as precise integration of dopant atoms into the GNR structure. The bottom-up approach is ideal for achieving such structures since here a molecular precursor is chemically engineered and used as the building block for on-surface synthesis of GNRs. This technique leads to homogeneous GNRs having a specific edge geometry and width. By changing the chemical structure of the building block molecule, GNRs of different edge geometry, width, or even doping can be fabricated. Therefore, the bottom-up approach creates a robust route for controllably fine-tuning the electronic properties of GNRs at the atomic-scale.

The first successful bottom-up GNR synthesis was reported in 2010.[16] Fig 1.4 presents a reaction pathway for molecular precursors to self-assemble into N = 7 AGNRs. Importantly the molecular precursors are designed to be terminated by halogen molecules. When they are deposited onto metallic surfaces, and annealed to elevated temperatures, they undergo a surface-assisted chemical reaction (Ullmann-type coupling) where the halogen atoms unbind and leave the molecular precursors with radicals.[17-20] As the radicals diffuse on the surface, they covalently bind into linear polymer chains. Upon further annealing to higher temperatures, the polymer

chains undergo cyclodehydrogenation to create atomically thin, flat AGNRs.[16] This approach has now then been used for numerous GNRs of different widths, edge geometries, and dopants where each structure hosts very different electronic properties.[11, 21-30] Throughout my time in graduate school, I explored many different GNR structures. This dissertation presents three of these projects in great detail.

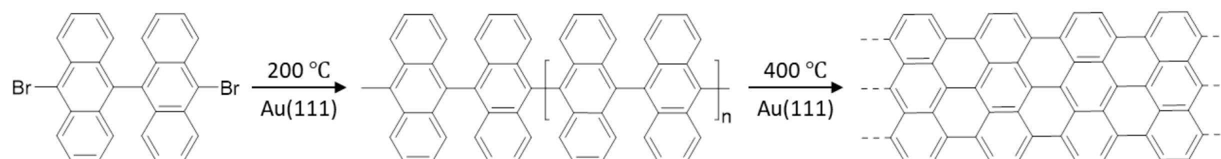

Figure 1.4 | Reaction scheme of N=7 AGNRs. The left molecule is 10,109-dibromo-9,99-bianthryl which is the molecular precursor. After deposition on the Au(111) surface, the sample is annealed to 200 ℃ resulting in the formation of linear polymers through Ullmann-type coupling. A second annealing step at 400 ℃ results in the formation of N = 7 AGNRs.

1.2 Quantum Spin Hall Insulator

1.2.1 Topology

Topology is a classifying tool for materials that has recently attracted a lot of attention. The significance of topology can be seen through a simple example: oranges and bowls belong to one topological class while coffee mugs and doughnut belong to another topological class, since the latter two possess holes. In quantum mechanics, topology is related to change of the Hamiltonian of the systems when subjected to an adiabatic transformation. Two systems (that have gapped band structures), have the same topology if their Hamiltonians can be continuously deformed into one another without closing the energy gap. This gives rise to unique 1D states that can exist at the boundary between two materials of different topologies. Hence, topological give considerable rise to new exotic physical phenomena that were not previously possible.

In general, the different topological classes can be distinguished by a topological invariant, the so-called Chern invariant.[31-33] The Chern invariant can be understood through a Berry phase associated with the Bloch wavefunction, where electronic states are described in terms of their crystal momentum k, in a periodic Brillouin zone. When a quantum state is transported around a closed loop in momentum space, the Bloch wavefunction picks up a well-defined gauge-invariant phase known as Berry phase.[33-37] This phase can be described as the line integral of

$$A_m = i\langle u_m|\nabla_k|u_m\rangle, \tag{1.1}$$

where $|u_m(k)\rangle$ is a Bloch wavefuntion, and A_m is Berry connection. The Berry phase can also be expressed as a surface integral of the Berry curvature

$$F_m = \nabla \times A_m, \tag{1.2}$$

This Berry curvature can be used to define the Chern invariant, where

$$C = \frac{1}{2\pi}\int d^2k\, F_m, \tag{1.3}$$

is the first Chern number and $C \in Z$. It is through this Chern invariant that systems of different topologies can be distinguished.

1.2.2 Topologically Trivial and Non-Trivial

To better understand how these concepts play a role in physical systems, we will consider a few examples. The simplest kind of insulator is a collection of inert atoms where the electrons are tightly bound to each atom. Fig. 1.5b presents the band structure of such a system; due to filling of the atomic energy levels the filled and empty states are separated by an energy gap. We call this a trivial insulator; most of the materials that we are used to and use in our daily lives fall into this same topologically trivial class of materials.

Sometimes a system, such as an integer quantum Hall insulator, can have a different topology than a normal insulator. The integer quantum Hall effect (QHE) can be seen when electrons on a 2D plane are subjected to a perpendicular B-field. The electrons will go through cyclotron motion, where quantum mechanics quantizes their energy levels, creating so-called Landau levels (Fig. 1.5c). The occupied and unoccupied Landau levels are separated by an energy gap described as

$$E_m = \hbar\omega_c\left(m + \frac{1}{2}\right), \quad (1.4)$$

where ω_c is the cyclotron frequency (Fig. 1.5c,d).

Comparing the trivial insulator with the integer quantum Hall insulator, we can see that both systems have energy gaps. However, their electronic properties are still quite different. Unlike a trivial insulator, the quantum Hall (QH) insulator hosts conductive one-directional edge states that carry a quantized edge conductance of

$$\sigma_{xy} = C_n \frac{e^2}{2\pi\hbar} \quad (1.5)$$

The existence of such edge states can be seen even classically where the orbits at the boundary go through a skipping cyclotron motion, causing conduction in a single direction along the one-dimension boundary that is protected from backscattering. (Fig. 1.6a,b).[33, 38-44] Hence, what distinguishes these two systems are their topologies: the collection of inert atoms is a trivial insulator while the QH insulator has a different topology and is a topologically non-trivial material.

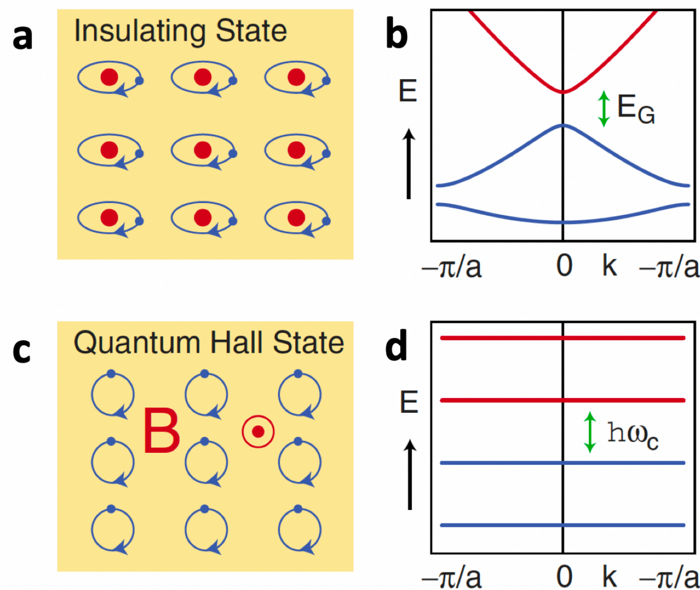

Figure 1.5| Materials of different topologies. a, An atomic insulator. b, A model insulating band structure. c, The cyclotron motion of electrons. d, The Landau levels, which may be viewed as a band structure. (Figure is reproduced with permission from ref. 45)[45]

1.2.3 Quantum Spin Hall Insulator

Haldane proposed a toy model on a spinless graphene lattice where the QHE can occur through a standard Bloch band structure (considering first and second nearest neighbors) with broken time-reversal invariance but no net magnetic flux through the system.[44] This became a building block for the later prediction of 2D quantum spin Hall (QSH) insulators.[46-48] In the simplest case, a QSH insulator can be thought of as two copies of a QH insulator with Hall conductivity for up and down spins propagating in opposite direction (Fig. 1.6c) in the presence of time reversal symmetry. Time-reversal symmetry will still be preserved in a QSH insulator as it flips both the spin and direction of the edge conduction. This quantized spin Hall conductivity propagating at the edges can be defined by $\sigma_{xy}^{s} = \frac{e^2}{2\pi\hbar}$.[46-54]

Moreover, these counter-propagating edge states are robust even at their crossing at $k = 0$ because they are protected by Kramers degeneracy. Hence, in the presence of any non-magnetic disorder, backscattering is forbidden, and edge state transport is ballistic. Hence, a 2D TI, or a QSH insulator, is characterized by an insulating bulk and a conductive helical edge state, in which carriers with different spins counter-propagate to realize a geometry-independent edge conductance $2e^2/h$.[46-54] QSH insulators host a gapped bulk with helical edge states protected from backscattering via time reversal symmetry.

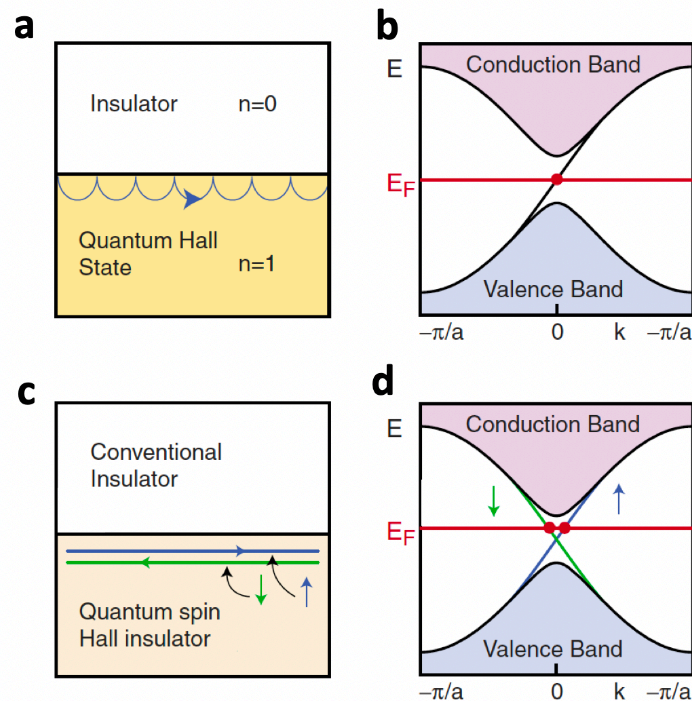

Figure 1.6| Edge state of QH and QSH. a, Skipping cyclotron orbits. b, The electronic structure of a semi-infinite strip described by the Haldane model. A single edge state connects the valence band to the conduction band. c, The interface between a QSH insulator and an ordinary insulator. d, The edge state dispersion in a graphene model where up and down spins propagate in opposite directions. (Figure is reproduced with permission from ref. 45)[45]

Due to these unique characteristics, QSH insulators can pave the way for a new generation of electronic and spintronic devices, enabling new applications. The only scattering channel for such helical edge current is back scattering, which is prohibited by time-reversal symmetry, making QSH insulators a promising material candidate for spintronics and other applications.

1.2.4 QSH, Previous Experimental Realizations

So far only a handful of QSH systems have been fabricated, mostly limited to quantum well structures of three-dimensional (3D) semiconductors such as HgTe/CdTe [55] and InAs/GaSb.[56] Edge conduction consistent with a QSH state has been observed.[55-57] However, the behavior of these systems under a magnetic field, where time-reversal symmetry is broken, cannot be explained within our current understanding of the QSH effect.[58, 59] Also, the small bandgaps exhibited by many candidate systems, as well as their vulnerability to strain, chemical adsorption, and element substitution, make them impractical for advanced spectroscopic studies or applications. As a result, there have been continued efforts to predict and investigate other material systems to further advance the understanding of this novel quantum phenomenon.[60-64] There are many challenges to make a robust 2D material with a QSH state, a platform needed for widespread study and application.

1.2.5 TMDs as a Platform

Monolayer transition metal dichalcogenides (TMDs) are atomically-thin MX_2 materials, where M is a transition-metal atom and X is a chalcogen atom. They come in different structural phases: 1H, 1T, and 1T', as seen in Fig. 1.7. Depending on their atomic compositions and structural phase, their electronic properties can be very diverse, ranging from wide-gap semiconductors to superconductors. Recent theoretical studies have predicted that the 1T' phase of MX_2 TMDs, where M = (W, Mo) and X = (Te, Se, S) should form a new class of QSH insulators with relatively large bandgaps.[65, 66] The 1T' phase of this class of TMDs was predicted to host topologically-protected dissipationless edge states that bridge the energy gap opened by band inversion and strong spin–orbit coupling. Realization of such QSH insulators in 2D TMDs would be a breakthrough as this is a robust family of materials with none of the complications from surface/interface dangling bonds that are seen in 3D semiconductors, enabling a broad range of study and application of QSH physics.

As seen in Fig. 1.8, depending on the material, some phases are more stable than the others. Among them, WTe_2 is the only material for which the 1T' phase is most energetically favored. For the other materials (such as WSe_2), the 1T' phase is a metastable phase that may coexist with the energetically preferred 1H phase, which is a wide-gap semiconductor. Having access to these TMDs of such different electronic properties allows the realization of novel domain boundaries with different topologies as follows: 1) non-trivial domain boundaries between 1T'–vacuum or 1T'–1H phases that host helical edge states, as well as 2) trivial domain boundaries that can exist inside the topologically non-trivial 1T' phase. Figure 1.9 presents a sketch of these possible new topological domain boundaries. This flexibility allows for the creation and manipulation of 1D atomically-precise interfaces that can either carry helical

conductions channels or trivial conduction channels of charge or spin by controlling the topology of the 2D parent material. This behavior paves the way for controllable creation of topological devices where both topologically protected and conventional ballistic charge and spin transport regimes co-exist in a single circuit.[67]

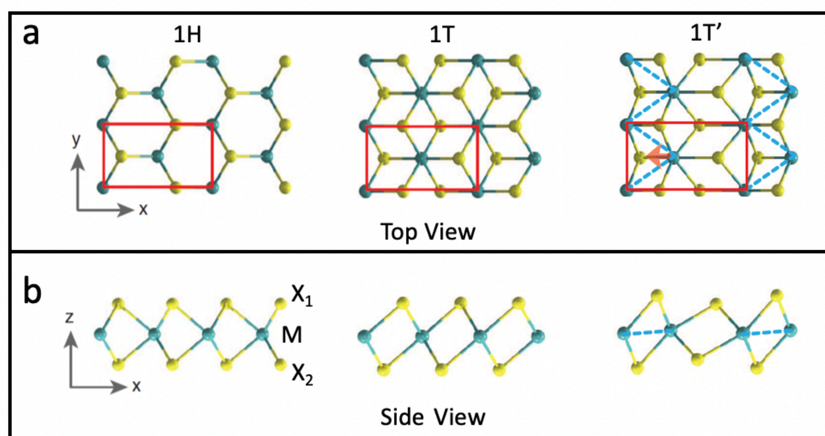

Figure. 1.7| Atomistic structures of monolayer TMDs of the three different phases. a, and b, top and side view of 1H, 1T, and 1T'-MX_2. 1T′ structure is distorted 1T-MX_2, where the M atoms have been moved from their original rhombohedral position to form 1D zigzag chains indicated by the dashed blue line. The unit cell is indicated by red rectangles. (Figure is reproduced with permission from ref. 65)[65]

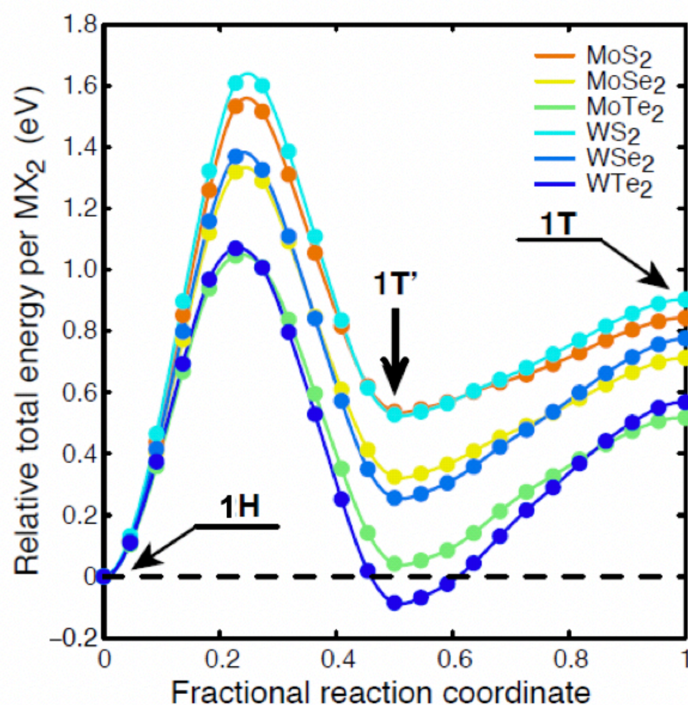

Figure 1.8| Structural stability of monolayer 1T'–MX_2. relative total energy per MX_2 as a function of fractional reaction coordinate.

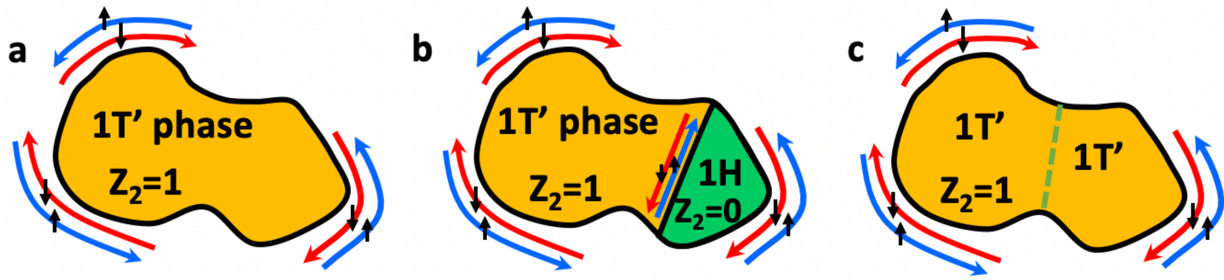

Figure 1.9| Different topological domain boundaries. a, b, non-trivial domain boundaries at 1T'–vacuum and 1T'–1H interfaces. c, Trivial domain boundary between two 1T' phases.

Chapter 2. Scanning Tunneling Microscopy

Scanning tunneling microscopy (STM) is a surface sensitive characterization technique that can measure the tunneling current between a sharp metallic tip and a conducting sample. The tip is brought close to the sample (usually less than 1 nm above the sample) and a voltage difference is applied between the sample and tip. STM measures the quantum tunneling current between the sample and tip, which in turn allows it to measure the local density of states (LDOS) of the sample. Moreover, STM tips have X-Y movement, which enables position dependent. STM is thus capable of probing both the geometric structure and electronic properties of a sample. The first STM was invented in 1980 by Gerd Binnig and Heinrich Rohrer which earned them the physics Nobel Prize in 1986. The basic theory and principles of STM will be discussed in this section. For a more complete discussion please refer to ref.68[68] and Ryan Yamachika's thesis.[69]

2.1 Quantum Tunneling Theory of STM

The wave characteristic of electrons in quantum mechanics allows for tunneling current through a barrier between two systems; this is the essence of STM. The simplest model for describing electron tunneling in STM is through Fermi's golden rule.[68, 70]

$$W_{i\to f} = \frac{2\pi}{\hbar}\left|\langle\psi_f|H'|\psi_i\rangle\right|^2\rho_f(E_i) \qquad (2.1)$$

Here $W_{i\to f}$ is the electron transition rate from state ψ_i to ψ_f and $\rho_f(E_i)$ is the density of the final states.

When a voltage difference is applied between the two tunneling electrodes (here tip and sample), the total electron tunnel rate can be calculated to be a difference of the transition rates from tip to sample and from sample to tip:

$$W = \int (dW_{s\to t} - dW_{t\to s})$$
$$= \frac{2\pi}{\hbar}\int_{-\infty}^{\infty}\sum_{n}^{N(E_t)}\left|\langle\psi_{s,n}|H'|\psi_t\rangle\right|^2\rho_{s,n}(E_t)\rho_t(E_t+e_cV_t)(f(E_t)-f(E_t+e_cV_t))dE_t \qquad (2.2)$$

Here $f(E)$ is the Fermi dirac distribution, and the applied voltage difference forces the Fermi level of the sample and the tip to be shifted by an amount = e_cV_t. Here we are summing over all the possible states on the sample that have energy E_t. The tunneling current is then proportional to the transition rate of the electrons multiplied by the electron charge:

$$I(V) = \frac{2\pi e_c}{\hbar}\int_{-\infty}^{\infty}\sum_{n}^{N(E_t)}\left|\langle\psi_{s,n}|H'|\psi_t\rangle\right|^2\rho_{s,n}(E_t)\rho_t(E_t+e_cV_t)(f(E_t)-f(E_t+e_cV_t))dE_t \tag{2.3}$$

However, there is an oversight in this model since it assumes the initial and final states of the transition to be in the same system. This is not the case for STM, where the tunneling current is measured between two different systems (i.e the tip and the sample).[68, 69] To overcome this, Bardeen proposed a new approach to model a metal-insulator-metal junction and implemented new approximations to extend Fermi's golden rule to tunneling.[68, 71] Bardeen's theory allows for calculation of tunneling current between two metals separated by a thin insulating layer (i.e. vacuum in the case of STM). Here we assume that the eigenstates of the sample and tip are nearly orthogonal to each other, meaning tip and sample wavefunctions have only a slight overlap. This indicates that there exists some probability/time for an electron from tip to hop onto the sample (or vice versa). For simplicity, we can assume that all the electrons are on the tip at the beginning. We have to then solve the Schrödinger equations to follow the evolution of the electrons between tip and sample. To do so we first define a tunneling matrix element M_{t-s}:

$$M_{t-s} = \langle t|H'|s\rangle = \int \psi_t^*(H-H_s)\psi_s d^3r = \frac{\hbar^2}{2m}\int_\sigma(\psi_s\nabla\psi_t^* - \psi_t^*\nabla\psi_s).dS \tag{2.4}$$

Where H is the total hamiltonian and H_s satisfies sample and barrier perturbations. The integration takes place on any surface, σ, separating the tip from the sample. We are in fact using a perturbation to scatter a tip state into the continuum states of the sample at the same energy. Using the tunneling matrix element to solve the time-dependent Schrödinger equation, the probability of tunneling from the *s*-th state of the sample to the *t*-th state of the tip if found to be:

$$p_{t-s}(t) = |c_s(t)|^2 = |M_{t-s}|^2\frac{4sin^2[(E_t-E_s)t/2\hbar]}{(E_t-E_s)^2} \tag{2.5}$$

Now to further simplify the expression (2.5), we sum over all the possible states of the sample with energy E_s. We also assume that the tunneling is elastic (meaning $E_s = E_t$). The expression for total probability of tunneling from tip to sample in a time τ is then:

$$p_{t-s}(\tau) = \frac{2\pi}{\hbar}|M_{t-s}|^2\rho_s(E_s)\tau \tag{2.6}$$

An important consequence of Bardeen's theory is that the tunneling current is dependent on the shape of the tip (Eq. 2.4). This can make a tunneling calculation quite complex, since the structure of the tip is often unknown. Tersoff-Hamann theory overcame this problem by further modifying Bardeen's theory and proposing a new model for the tip to make the calculation independent of the tip shape.[72, 73] The Tersoff-Hamann model of STM emphasizes the properties of the sample surface and allows the tip contribution to be ignored. It assumes the tip wavefunction to be an s-wave (such as $\psi = e^{\kappa|r-r_0|}/4\pi|r-r_0|$), centered around the tip apex nucleus at position $r_0 = (0,0,z_0)$, while the sample surface is at the plane $z = 0$. The time-independent Shrodinger equation near the Fermi level can be written as

$$-\frac{\hbar^2}{2m}\nabla^2\psi(r) = -\Phi\psi(r), \text{ or} \qquad \nabla^2\psi(r) = \kappa^2\psi(r) \qquad (2.7)$$

where $\kappa = \sqrt{\frac{2m\Phi}{\hbar}}$, and Φ is the work function.
By solving the Schrödinger equation above, which satisfies both the sample and tip wavefunction, new solutions for each can be found. These new solutions can be plugged into Eq. 2.4 to modify the tunneling matrix element M_{t-s} to be

$$M_{t-s} = \frac{\hbar^2}{2m}\int_{z=0}(\psi_s\nabla\psi_t^* - \psi_t^*\nabla\psi_s)dS \qquad (2.8)$$

which simplifies to

$$M_{t-s} \propto \psi_s(r_0) \qquad (2.9)$$

Hence, for a spherical s-wave tip, the tunneling matrix element M_{t-s} is proportional to the value of the tunneling wavefunction evaluated at the apex of the tip. This means that a bigger contribution of the tunneling current comes from the surface states that decay further into the vacuum.

In order to apply this knowledge to real-life STM measurements, we have to look at the total tunneling probability of all the states of the tip at a specific energy, ε. (Fig 2.1 presents a schematic STM tunnel junction). This means that we have to multiply Eq. 2.6 with the density of states of the tip, $\rho_t(E_t)$ where $E_s = E_t = \varepsilon$. Hence we can rewrite Eq. 2.6 as

$$p_{t-s}(\tau) = \frac{2\pi}{\hbar}|M_{t-s}|^2\rho_t(\varepsilon)\,\rho_s(\varepsilon)\tau \qquad (2.10)$$

For tunneling to take place a voltage difference should be applied between tip and the sample enabling occupied tip electrons to tunnel into unoccupied sample states. The tunnel current can then be calculated to be

$$I = \frac{4\pi e_c}{\hbar}\int_0^{e_cV_t}|M_{t-s}|^2\rho_t(E_F - e_cV_t + \varepsilon)\,\rho_s(E_F + \varepsilon)d\varepsilon \qquad (2.11)$$

where E_F is the Fermi level and V_t is the applied voltage to the tip. The integral limit is the range of the energies between the Fermi levels of the tip and the sample in the presence of the applied voltage, which is the allowed energy range through which electrons can elastically tunnel from the tip to the sample.

Eq. 2.11 can further be simplified by assuming the tip density of states to be constant in energy, $\rho_t(E_F - e_cV_t + \varepsilon) = \rho_t$, meaning allowing it to be pulled out of the integral. Assuming that the tunneling matrix element is also energy independent at small energy ranges around the Fermi level, it can also be pulled out of the integral. Hence Eq 2.11 can be reduced to

$$I = \frac{4\pi e_c}{\hbar}\rho_t\int_0^{e_cV_t}|M_{t-s}|^2\,\rho_s(E_F + \varepsilon)d\varepsilon \qquad (2.12)$$

The differential conductance (dI/dV) can be calculated by taking derivative of Eq. 2.12:

$$\frac{dI}{dV_t} = \frac{4\pi e_c}{\hbar}|M_{t-s}|^2\rho_t\rho_s(E_F + e_cV_t) \tag{2.13}$$

This is a significant result which tells us that the differential conductance is directly proportional to the local density of states of the sample. [68, 69, 72, 73]

Another interesting case to consider is when the voltage is applied on the sample instead of the tip (the tip and sample voltages are always opposite $V_{sample} = -V_{tip}$. Eq. 2.13 shows that when a negative voltage is applied to the tip (positive sample bias), the STM probes unfilled the density of states of the sample. Figure 2.1 shows the energy alignment of an STM tip junction.[68, 69] When a positive voltage is applied to the tip (negative sample bias) the filled states of the sample are probed.[11, 21-23]

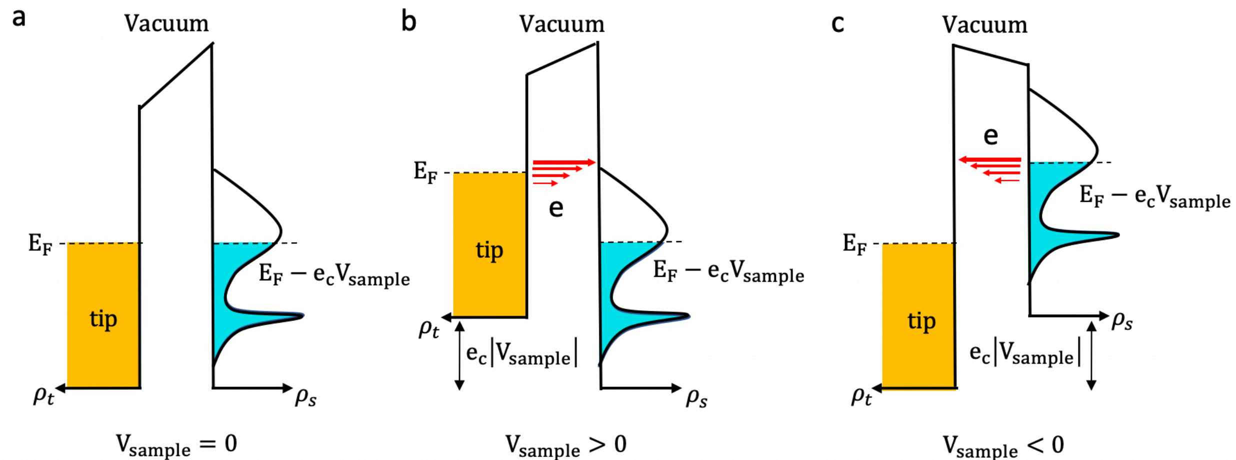

Figure 2.1| Schematic of STM tunnel junction. Tip is modeled by flat featureless density of state (DOS). a, Tip and sample are connected but no sample bias is applied. b, c sketch of the electronic structure for the positive and negative sample biases. Red arrows indicate the direction of the tunneling current.

2.2 Basics Principles of STM

STM is quite versatile, it can operate in air, ultra high vacuum (UHV), water, and other liquids. It can also operate at different temperatures, ranging from a few mK to over 600K. Throughout my PhD, I worked on a room-temperature (RT) STM as well as two LHe temperature (T = 4K) STMs that all operated in UHV.

Figure 2.2, presents a schematic of STM electronics. As explained in 2.1, the applied voltage between the tip and the sample results in a tunneling current. This tunneling current is

then converted to voltage, goes through a feedback loop and is used as the main input to the STM electronics. It is this feedback loop that allows STM to perform the two most common modes of measurement: constant-current mode (where the feedback loop keeps the current constant) and constant-height mode (where the feedback loop is tuned off). The plane of the sample's surface is defined to be the x-y plane and the direction perpendicular to it is the z direction. The STM tip has multiple piezoelectrics controlling its movements, allowing it to move in all 3 directions. The X- and Y-piezos control its movement in the x-y plane and allow for sub Å spatial resolution. The Z piezoelectric controls the tip-sample distance. There are two modes of movement in Z, coarse movement (when high voltage is used to move the tip in larger steps towards or away from the sample) and fine movement where the lower voltages are used to move the tip at smaller intervals, enabling precision needed for reaching tunneling conditions.

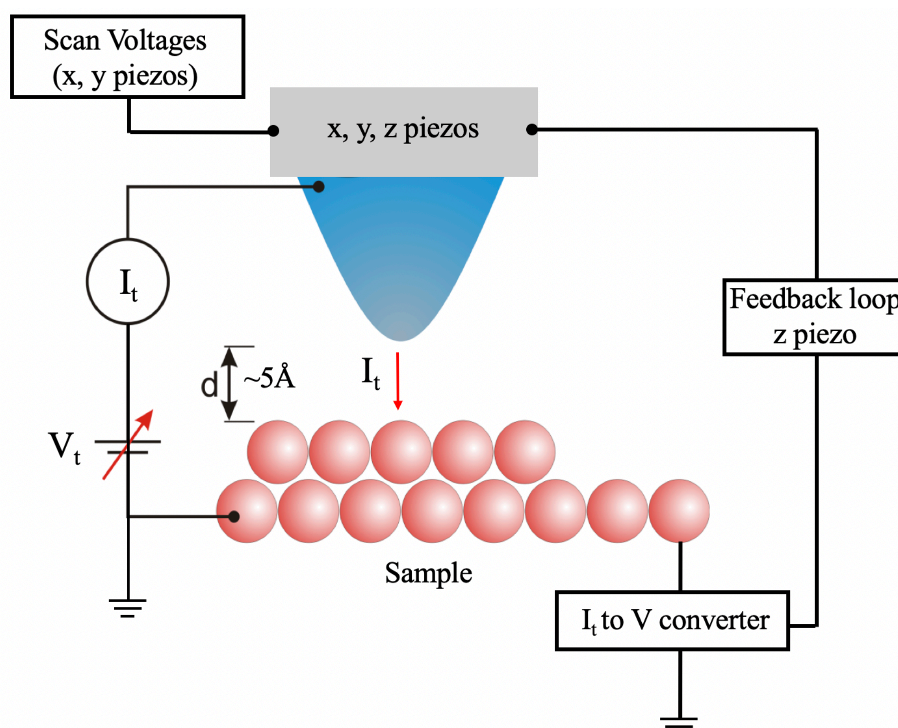

Figure 2.2| Diagram of basic STM set-up.

STM has three main types of measurements; topography, STS point spectroscopy and dI/dV mapping measurements. In the most common topography measurements a constant voltage is applied and the feedback loop is used to keep the tunneling current constant (i.e. constant-current mode). The X-Y piezoelectrics raster scan the sample and measure the sample's wavefunction as a function of position to generate a topographic image of the surface. The topography images plot the sample surface where the integral of the LDOS is constant, and so it is strongly dependent on the value and the sign of the applied voltage, as well as the tip-sample separation. For example, by decreasing the tip-sample separation by 1Å, the tunneling current increases by one decade for a typical metal work function of ~ 5eV. All these features enable STM to achieve stunning topographic images with atomic resolution of the surface.

STM spectroscopy is performed by positioning the tip at a single point, turning the feedback loop off and sweeping the sample bias through an energy window while differential conductance is measured. This is called STS and measures the LDOS of the sample through the energy window of the sample bias. In order to better see this relationship Eq. 2.12 and 2.13 can be further generalized at finite temperature and bias to show

$$I \propto \frac{4\pi e_c}{\hbar}\rho_t \int_0^{e_c V_t} \sum_m \left|\psi_{s,m}(r_0)\right|^2 \delta(E_F + \varepsilon - E_m)\, d\varepsilon \tag{2.14}$$

where the sum is over all the states of energy E_m.

$$\frac{dI}{dV_t} \propto \sum_m \left|\psi_{s,m}(r_0)\right|^2 \delta(E_F + \varepsilon - E_m) = LDOS\,(r_0, E_F + e_c V_t) \tag{2.15}$$

Eq. 2.15 provides a very simple way to interpret STS measurements.[68, 69] It shows that the amplitude of the differential conductance signal at a sample bias V_t is proportional to the sample LDOS at energy $E_F + e_c V_t$ at the tip position r_0. Although it is possible to numerically differentiate the tunneling current $I(V)$, a lock-in amplifier is the preferred method of measuring dI/dV since it gives a much better signal-to-noise ratio. The measured $I(V)$ is an input signal to the lock-in amplifier, a small modulating voltage signal is then added and the resulting modulation current can be read as the output of the lock-in amplifier. In our experiments, we used typical modulation voltages of $1 - 40\text{mV}_{\text{rms}}$ with varying frequencies between 400-700 Hz. The magnitude of the modulation voltages depends on the size of the feature being measured (for features spanning larger voltage range such as large gaps, larger modulation voltages are used).

STM can also measure position dependent STS data, and create a 2D image of the energy-resolved LDOS of the sample as a function of position. This is called dI/dV mapping. These different modes of measurements make STM uniquely capable of measuring precise electronic and structural properties of 1D and 2D systems, as presented in Chapters 3 and 4.[21-23, 74-76]

2.3 Deposition methods

The first half of this dissertation presents results where the samples of interest were fabricated directly on a metallic substrate. In order to successfully achieve these samples, many deposition and growth techniques were designed and calibrated in our STM chambers. This section will briefly go through the steps necessary to accomplish this. More information can also be found in C. Chen, Y.-C. Chen and X. Zhang's theses.[77-79]

The first step before any sample fabrication is to prepare the substrate. Since our STMs operate in UHV, the samples are prepared by stepwise sputtering and annealing processes. Argon sputtering bombards the surface with Ar^+ ions in order to remove impurities on the surface. The

sputtering step is then followed by annealing the substrate to high temperatures in order to desorb impurities and to smooth out the surface. There are two modes of annealing a sample, by either using resistive heating, which can reach lower temperatures (< 400°C), or by using electron-beam (E-beam) heating, where high energy electrons bombard the sample, and thus increase its temperature. E-beam heating is used for reaching higher temperatures (>400°C). These sputtering-annealing steps are repeated many time (3-10 times depending on the cleanliness of the original substrate) to ensure a smooth and defect-free surface, which is very important for deposition and growth of nanostructures on the surface.

The next step is to deposit the desired molecules onto the substrate. Depending on the vapor pressure of the molecules this step can require different deposition techniques. If the molecules are stable under UHV conditions at RT, then Knudsen cell evaporators can be used. Figure 2.3 presents a schematic of such evaporators, where the desired molecules, (a powder in ambient conditions) are placed into the crystal crucible. Once the evaporator is in UHV, current is run through the filament that is wrapped around the crucible (the W heating coil) to heat up and sublimate the molecules. For multiple depositions a dual cell evaporator was designed to enable successful co-deposition of two different molecules onto the surface. Greater detail of the evaporators' designs can be found in refs. 77 and 80.[77, 80] For depositing metals, e-beam evaporators are often be used, since they require higher temperatures than can be achieved by simple resistive heating.

For these evaporation methods, an applied current can control the temperature and hence the deposition rate. However, when using a new molecule with unknown sublimation temperatures, it is important to have a reliable method to find the sublimation temperature as well as the deposition rate. A quartz crystal microbalance (QCM) is a useful tool for such calibrations. It uses a Au electrode as its substrate, and measures the change in the resonant frequency of the quartz crystal resonator as the evaporated molecules are absorbed onto the electrode (the change in frequency is due to the change of the mass that takes place when molecules are absorbed on the surface). In order to calibrate the sublimation temperature and deposition rate of molecules, a QCM would be attached to a linear drive and positioned directly in the line of the molecular flux (to ensure accurate and reliable measurements). After calibration, the QCM can be pulled back and the prepared clean sample can be placed in the direct line of the molecular flux for deposition. Another important quantity to monitor is the temperature of the sample. Having an accurate and reliable temperature reading is especially significant for controllable and reproducible bottom-up fabricated nanostructures. We designed a direct temperature probe on a linear drive which could be placed directly on the sample. This probe was used to monitor the temperature of the sample surface during deposition as well as during the further annealing steps required for bottom-up synthesis. These steps are extremely important for successful and reproducible fabrication of nanostructures on the surface.

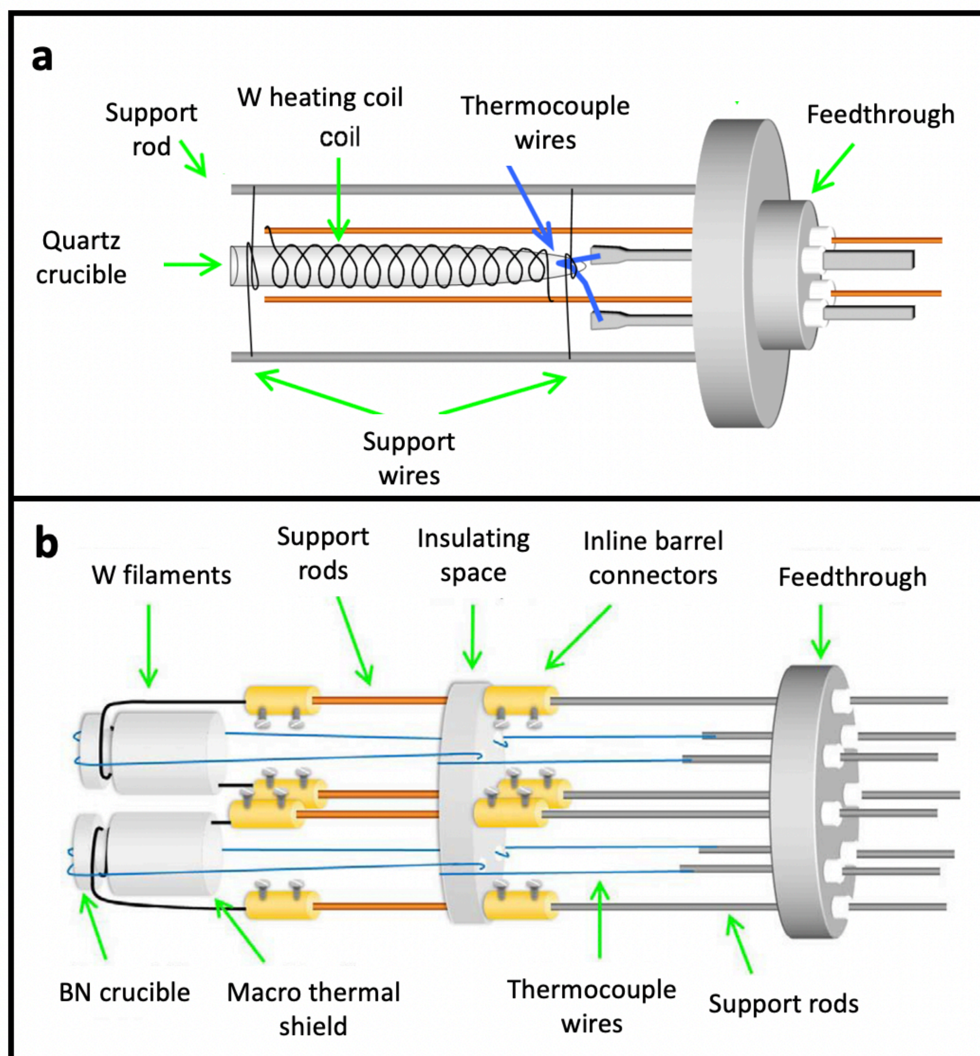

Figure 2.3| Schematics of evaporators a, Knudsen cell and b, dual cell evaporators.

If the vapor pressure of the desired molecule is so high that in ambient conditions it has a liquid or gas form, then a leak-valve deposition technique should be used. Figure 2.4 presents a schematic of such a set up. The source is placed in the belljar that is attached to a UHV leak-valve connected to the a UHV chamber. There is also a Tee fitting that connects the belljar to an external pump. This pump is used to pump down the small volume from ambient pressure to rough vacuum (~10 mTorr). The line is then filled with N_2 or Ar gas and then pumped again. This process is called pump/flush and it has to be repeated at least 5 times to ensure cleanliness of the source for deposition. Finally the pump/flush valve is closed and the system is ready for deposition. The leak-valve is slowly opened introducing the source to the chamber/sample while monitoring the pressure (If the source was in gas form, the belljar is replaced by higher pressure gas).

Leak-valve deposition can be used for both depositing onto RT or high temperature surfaces (such as depositing borazene on Cu surface to form a hexagonal boron-nitride (h-BN) monolayer) as well as cold surface deposition of molecules such as CO directly onto samples held at LHe temperature. Since for these types of deposition the molecules have access to the whole chamber, one must be mindful of deposition pressure so as to prevent contaminating the chamber. One way to decrease the needed deposition pressure is to have a smaller sample to source distance. Hence, for some molecules it is more desirable to perform the experiment in the load lock.

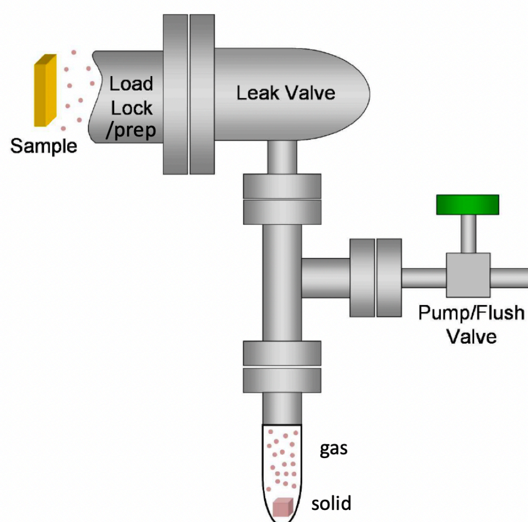

Figure 2.4| Schematic of leak-valve deposition set-up

Chapter 3. Graphene Nanoribbon Projects

GNRs are one-dimensional narrow strips of graphene with electronic properties that strongly depend on their width and edge structure, ranging from semiconducting to magnetic behavior. GNRs provide the opportunity to control their electronic properties through controlling their nano-scale structure. However, the challenge is to experimentally realize these GNRs with complete control over their atomic-scale structure. The bottom-up approach is an ideal route to overcome these challenges. This technique is capable of precisely controlling width and edge geometry of GNRs at the atomic scale as well as precise integration of dopant atoms into the structure of GNRs.

In this section three different projects involving bottom-up fabricated GNRs will be presented. In the first project, GNR heterojunctions of varying widths were realized through the bottom-up approach. Two segments of GNRs with different widths present different bandgap sizes. However, new unexpected states are also sometimes expected at the heterojunction interfaces. The second project involves a detailed study of the concentration dependence of boron-doped N = 7 AGNRs, where the AGNRs are substitutionally doped in their backbone. These boron atoms introduce new dopant states inside the bandgap of the pristine GNR, which are localized on the boron-dopant atoms. As the concentration increases, these dopant states continuously evolve into dopant bands. Surprisingly, the two dopant states have different symmetries, which leads to different hybridization strength with the underlying Au(111) substrate. The third project presents sulfur-doped N = 13 GNRs, where the sulfur atoms substitutionally dope the edges of the GNRs. Rather than significantly affecting the GNR DOS or energy gap, the electronegative S atoms only induce a rigid shift of the energies of both the valence and conduction bands.

3.1 Molecular Bandgap Engineering in 7-13 Armchair GNR Heterojunction

3.1.1 Motivation

Bandgap engineering has been used to create semiconductor heterostructure devices that perform processes such as resonant tunneling[81]and solar energy conversion[82, 83]. However, the performance of such devices degrades as their size is reduced[84, 85]. Graphene-based molecular electronics has emerged as a candidate to enable high performance down to the single-molecule scale[11, 16, 26, 29, 86-89]. Graphene nanoribbons, for example, can have widths of less than 2 nm and bandgaps that are tunable via their width and symmetry[3, 13, 85]. It has been predicted that bandgap engineering within a single graphene nanoribbon may be achieved by varying the width of covalently bonded segments within the nanoribbon[90-92]. Here we demonstrate the bottom-up synthesis of such width-modulated armchair graphene nanoribbon heterostructures, obtained by fusing segments made from two different molecular building blocks. We study these heterojunctions at subnanometre length scales with scanning tunneling microscopy and spectroscopy, and identify their spatially modulated electronic structure, demonstrating molecular-scale bandgap engineering, including type I heterojunction behavior. First-principles

calculations support these findings and provide insight into the microscopic electronic structure of bandgap-engineered graphene nanoribbon heterojunctions.

3.1.2 Bottom-up Synthesis and Local Characterization of Electronic States

GNR heterojunctions were fabricated by combining the molecular building blocks 10,10′-dibromo-9,9′- bianthracene (1) and 2,2′-di((1,1′-biphenyl)-2-yl)-10,10′-dibromo- 9,9′-bianthracene (2). As shown in Fig. 3.1a, molecules 1 and 2 are precursors to N = 7 and N = 13 armchair GNRs, respectively (referred to as 7-AGNRs and 13-AGNRs), where N is the width in number of rows of carbon atoms across the GNR[11, 16]. The building blocks were sublimed onto a Au(111) surface held at room temperature in ultrahigh vacuum (UHV). The surface was then heated to 470 K for 10 min to induce homolytic cleavage[93] of the labile C–Br bonds in building blocks 1 and 2, yielding surface stabilized diradical intermediates. Because 1 and 2 share the same bianthracene backbone, their diradical intermediates are structurally complementary and are able to colligate into linear polymers. On further heating to 670 K for 10 min, a stepwise cyclization/dehydrogenation sequence converted these linear polymers into 7–13 GNR heterojunctions (Fig. 3.1)[11, 89]. The samples were then cooled to 7 K for STM and STS measurements. Figure 1b presents an STM topographic image of a representative sample, showing 7–13 GNR heterojunctions with shapes resembling the sketch in Fig. 3.1a. The narrower segments in these heterojunctions are 1.3 ± 0.1 nm in width in the STM image and are composed of covalently bonded monomers of 1 (N = 7). The wider segments measure 1.9 ± 0.2 nm in apparent width and consist of bonded monomers of 2 (N = 13). As the building blocks mixed and fused in a random sequence during the initial step-growth polymerization, various N = 7 and N = 13 segment lengths were observed (Fig. 3.1b, inset).

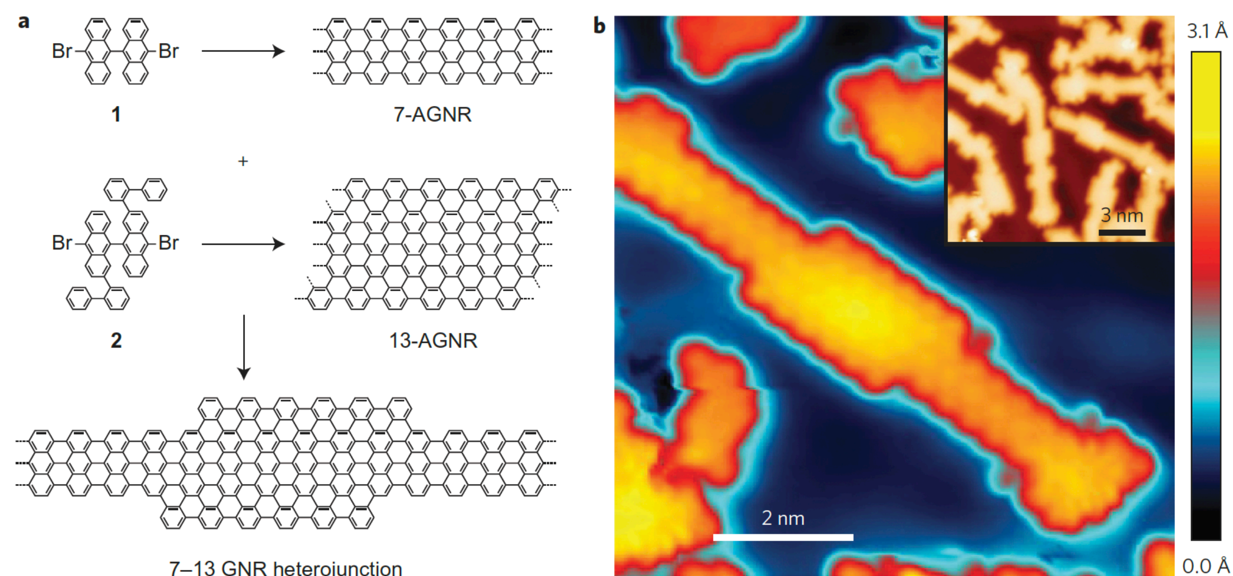

Figure 3.1 | Bottom-up synthesis of 7–13 GNR heterojunctions. a, Synthesis of 7–13 GNR heterojunctions from molecular building blocks 1 and 2. Building blocks 1 and 2 are co-deposited onto a pristine Au(111) surface held at room temperature. Stepwise heating induces cleavage of the labile C–Br bonds, colligation (at 470 K) and then cyclization/dehydrogenation

(at 670 K), resulting in 7–13 GNR heterojunctions. b, High-resolution STM topograph of a 7–13 GNR heterojunction (sample voltage V_s = 60 mV, tunneling current I_t = 200 pA). Inset: Larger-scale STM image of multiple GNR heterojunctions, showing a variety of segment lengths (V_s = 0.50 V, I_t = 2 pA).

To investigate the local electronic structure of these 7–13 GNR heterojunctions, tunneling conductance dI/dV spectra were recorded while placing the STM tip at different positions above the heterojunctions (the magnitude of dI/dV reflects the energy dependent LDOS at the STM tip position). As a background reference, a dI/dV spectrum taken on bare Au(111) is shown in green in Fig. 3.2. A characteristic spectrum (blue curve, Fig. 2) recorded at a specified position on an N = 7 segment of a single heterojunction (see image in Fig. 3.2 inset) exhibits a pronounced shoulder at V_s = 1.86 ± 0.02V (labelled state 1) and a peak at V_s = −0.90 ± 0.02 V (where V_s is the sample voltage). In contrast, the marked N = 13 segment (red curve) shows prominent peaks at V_s = 1.45 ± 0.02 V (labelled state 2) and Vs = −0.12 ± 0.02 V. The energy locations of these states are similar to the valence and conduction band-edges reported previously for isolated 7-AGNRs and 13-AGNRs on Au(111)[11, 26]. Additional states are observed in dI/dV spectra measured at positions near the interface between the N = 7 and N = 13 segments of a heterojunction. The black curve in Fig. 3.2, obtained at the interface position marked by the black cross in the inset to Fig. 3.2, exhibits two additional overlapping peaks labelled as states 3 and 4. Lorentzian peak-fitting yields peak positions for states 3 and 4 of V_s = 1.25 ± 0.02 V and V_s = 1.13 ± 0.02 V, respectively. All of these spectroscopic features were consistently observed on all ten GNR heterojunctions whose nanoribbon segments and interfaces were inspected via dI/dV tunneling spectroscopy using different STM tips (all heterojunctions inspected via dI/dV had both N = 7 and N = 13 segments composed of at least two monomer units each; that is, segment lengths ≥1.6 nm).

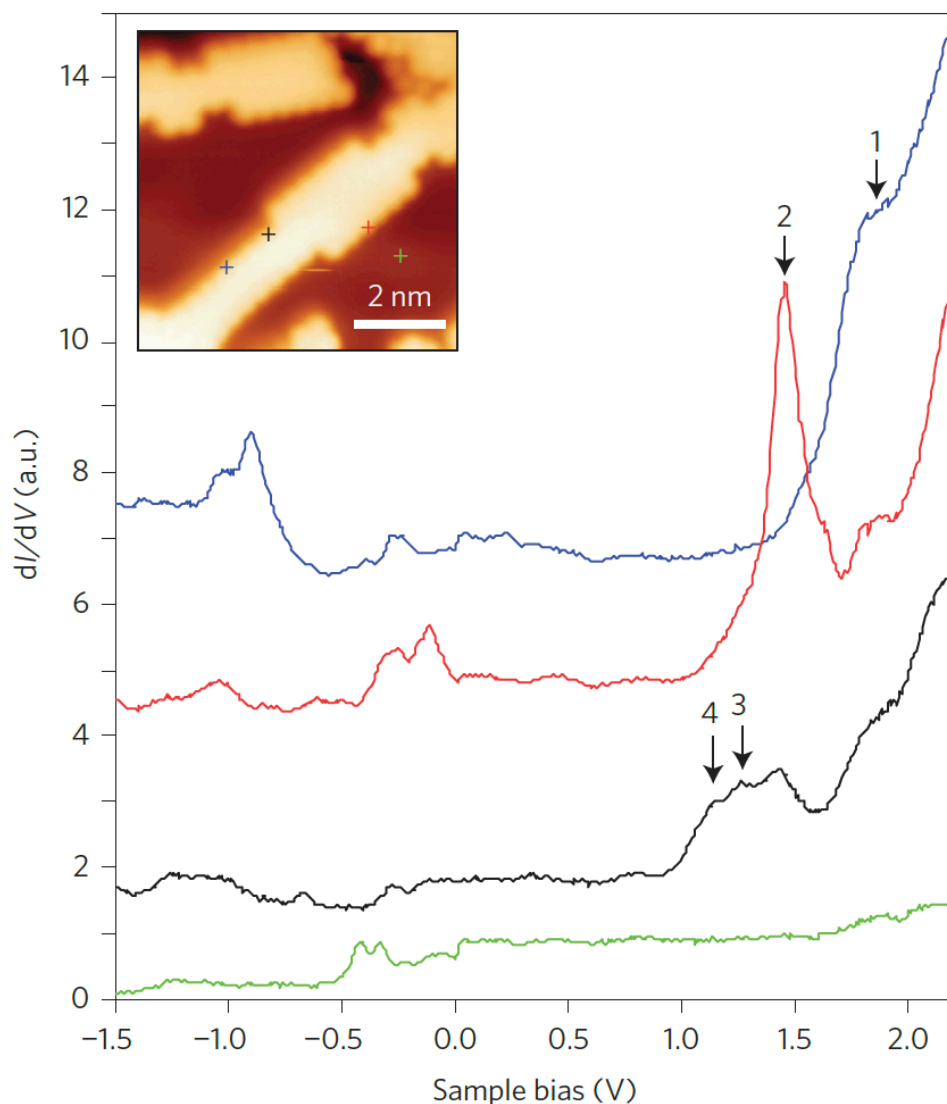

Figure 3.2 | STM dI/dV spectroscopy of 7–13 GNR heterojunction electronic structure. Blue curve: dI/dV spectrum acquired on the narrow N=7 segment of a 7–13 GNR heterojunction (location marked by blue cross in inset). Red curve: Spectrum acquired on the wider N = 13 segment (location marked by red cross in inset). Black curve: Spectrum acquired at the interface region between N=7 and N = 13 segments (location marked by black cross in inset). Green curve: Calibration spectrum acquired with tip held over bare Au(111). All spectra were acquired with the same STM tip. The black, red and blue curves are vertically offset by 1, 4 and 6 arbitrary units, respectively, for clarity (open-feedback parameters: $V_s = 1.00$ V, $I_t = 35$ pA, modulation voltage $V_{rms} = 10$ mV). Resonant peaks showing the locations of four GNR heterojunction states in the unoccupied region are labelled 1–4. Inset: STM topograph of the 7–13 GNR heterojunction measured to obtain this series of dI/dV spectra ($V_s = 0.10$ V, $I_t = 95$ pA).

The spatial distributions of GNR heterojunction states 1–4 were explored experimentally using dI/dV mapping (Fig. 3.3a–d). Figure 3a shows the dI/dV map obtained for the highest-energy state (state 1) at V_s = 1.86 V for the same heterojunction as shown in the inset to Fig. 3.2. The dI/dV map of state 1 exhibits significant LDOS at the edges of the narrower N = 7 segment and some LDOS at the edges of the wider N = 13 segment. Figure 3b shows the dI/dV map obtained at the energy of state 2 (V_s = 1.45 V). This lower-energy state shows significant LDOS near the edges of the wider N = 13 heterojunction segment, but no LDOS in the narrower N = 7 segment. Figure 3c shows the dI/dV map of state 3 at V_s = 1.25 V. This even lower-energy state exhibits significant LDOS at the corners of the interface between the N = 7 and N = 13 segments, as well as some LDOS at the outer edges of the wider N = 13 segment. Figure 3d shows the dI/dV map of state 4, the lowest energy peak for the unoccupied states, at V_s = 1.15 V. This state exhibits LDOS localized to the corners of the interface between the N = 7 and N = 13 regions, but very little LDOS anywhere else. The overall electronic structure of 7–13 GNR heterojunctions shows some features that can be intuitively understood. For example, the fact that the highest-energy unoccupied state (state 1) shows LDOS in both the narrower and wider segments while the adjacent, lower-energy state (state 2) shows significant LDOS only in the wider segment is consistent with a simple quantum well picture. Other features, however, are harder to understand. The origins of interface states 3 and 4, for example, are not intuitive within the quantum well picture. Moreover, the fact that GNR heterojunctions exhibit high LDOS intensity at their edges but not in their interiors (similar to previously reported pristine 7- and 13-AGNRs[11, 26, 29, 94]) conflicts with previous theoretical predictions that there are no localized edge-states in AGNRs near the band-edges[3].

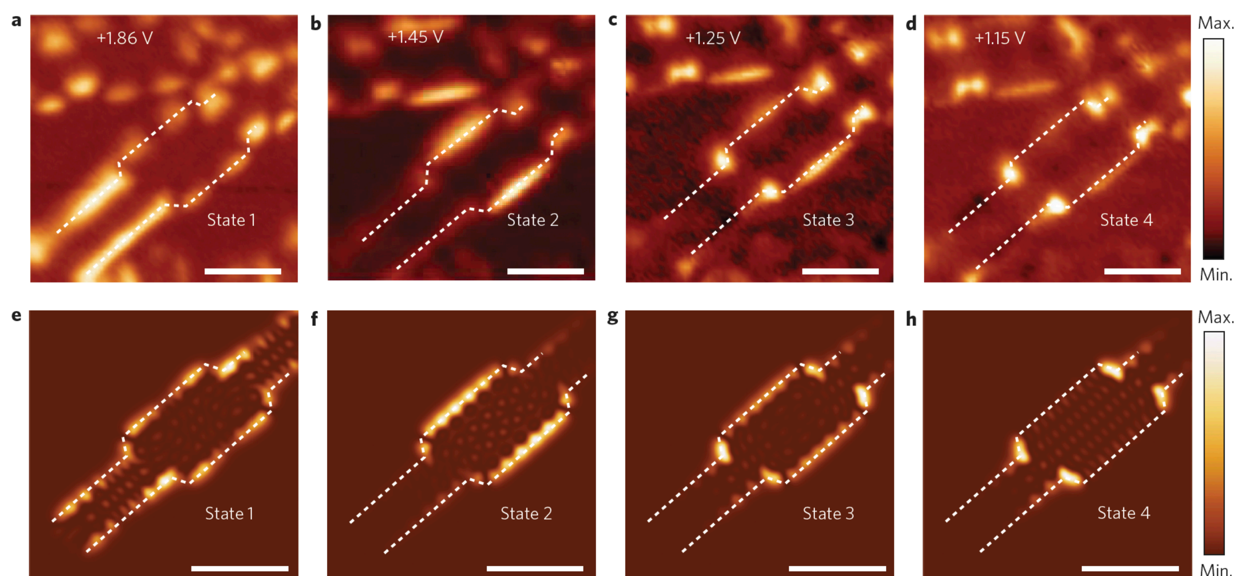

Figure 3.3 | Comparison of experimental dI/dV maps and theoretical LDOS for a 7–13 GNR heterojunction. a–d, Experimental dI/dV spatial maps recorded at the energies of spectroscopic peaks 1–4 for the 7–13 GNR heterojunction shown in the inset to Fig. 3.2 (I_t = 35 pA; modulation voltage V_{rms} = 10mV). Dashed lines are drawn at the mid-height topographic position of the edges of the 7–13 GNR heterojunction. e–h, DFT-calculated LDOS maps of states 1–4 calculated at a height of 4 Å above a 7–13 GNR heterojunction. Dashed lines are drawn at a

distance equal to one carbon dimer–dimer spacing (1.2 Å) outside the 7–13 GNR heterojunction carbon atom border. All scale bars, 2 nm.

3.1.3 Theoretical Calculations and Comparison to Experimental Results

To answer these questions and to better understand the properties of 7–13 GNR heterojunctions, we used first-principles density functional theory (DFT) using LDA to calculate their electronic structure (all calculations were carried out by T. Cao and S. G. Louie). We note that LDA tends to underestimate energy gaps, but here this is offset by the strong metallic screening of the substrate (see section 3.1.4 for further discussion). The simulation was based on the isolated 7–13 junction structure shown in the inset to Fig. 3.4a (all edges were terminated by hydrogen atoms, consistent with the experiment). The resulting DOS is plotted in Fig. 3.4a, with a Gaussian broadening of 0.06 eV (states localized at the two ends of the structure[3, 95] were removed from the plot because we probed regions far from the ends of the GNR heterostructures; see Methods). The four lowest unoccupied states are numbered 1 to 4 in descending order of energy, analogous to the labelling of the resonant states observed experimentally (Fig. 3.2). Out-of-plane height-integrated (h-integrated) LDOS plots (Fig. 3.4b–e) provide detailed information regarding the averaged planar (x–y) spatial distribution of these four calculated states. The lower-energy states 2, 3 and 4 are localized mainly on the wider N = 13 segment and can be understood as confined states in a potential well, with the adjacent and narrower N = 7 segments acting as energy barriers. The highest-energy state 1 extends over the entire heterojunction, including both the wide N = 13 and narrow N = 7 segments. All four states show significant intensity in the interior of the heterojunction and there are no localized edge states (as expected for armchair-edged GNR structures[3, 13]). This appears to be in contradiction with the experimental dI/dV maps depicted in Fig. 3.3a–d, where only the edges exhibit LDOS noticeably higher than the background.

We are able to resolve this apparent contradiction by examining the height dependence of the calculated 7–13 GNR heterojunction LDOS as opposed to the height-integrated quantities. This is shown by the simulated dI/dV maps in Fig. 3.4g–i, which illustrate the height dependence of the LDOS for one particular state (state 2) at different distances h above the GNR heterojunction. At a height of h = 2 Å above the carbon plane (Fig. 3.4g), the LDOS appears rather uniformly distributed across the N = 13 segment, resembling the height-integrated LDOS shown in Fig. 3.4c. However, as one moves higher above the carbon plane, the heterojunction edges begin to exhibit more intense LDOS than the interior (Fig. 3.4h,i), to the point where the edges completely dominate the LDOS at a height of h = 4 Å above the carbon plane (Fig. 3.4i). Simulated dI/dV maps at even greater distances appear similar to Fig. 3.4i. This type of behaviour was observed for all four of the calculated quantum well states of the heterojunction. As our STM tip is located ~5 Å above the carbon plane of the GNR heterojunctions during dI/dV mapping (estimated via the tunnel junction resistance at the open-feedback set points), the experimental dI/dV maps should be directly compared with the theoretical LDOS calculated in a plane above the heterojunction. Indeed, the calculated LDOS of heterojunction states 1–4 at a height of 4 Å above the carbon plane (Fig. 3.3e–h) match the corresponding experimental dI/dV maps very well (Fig. 3.3a–d).

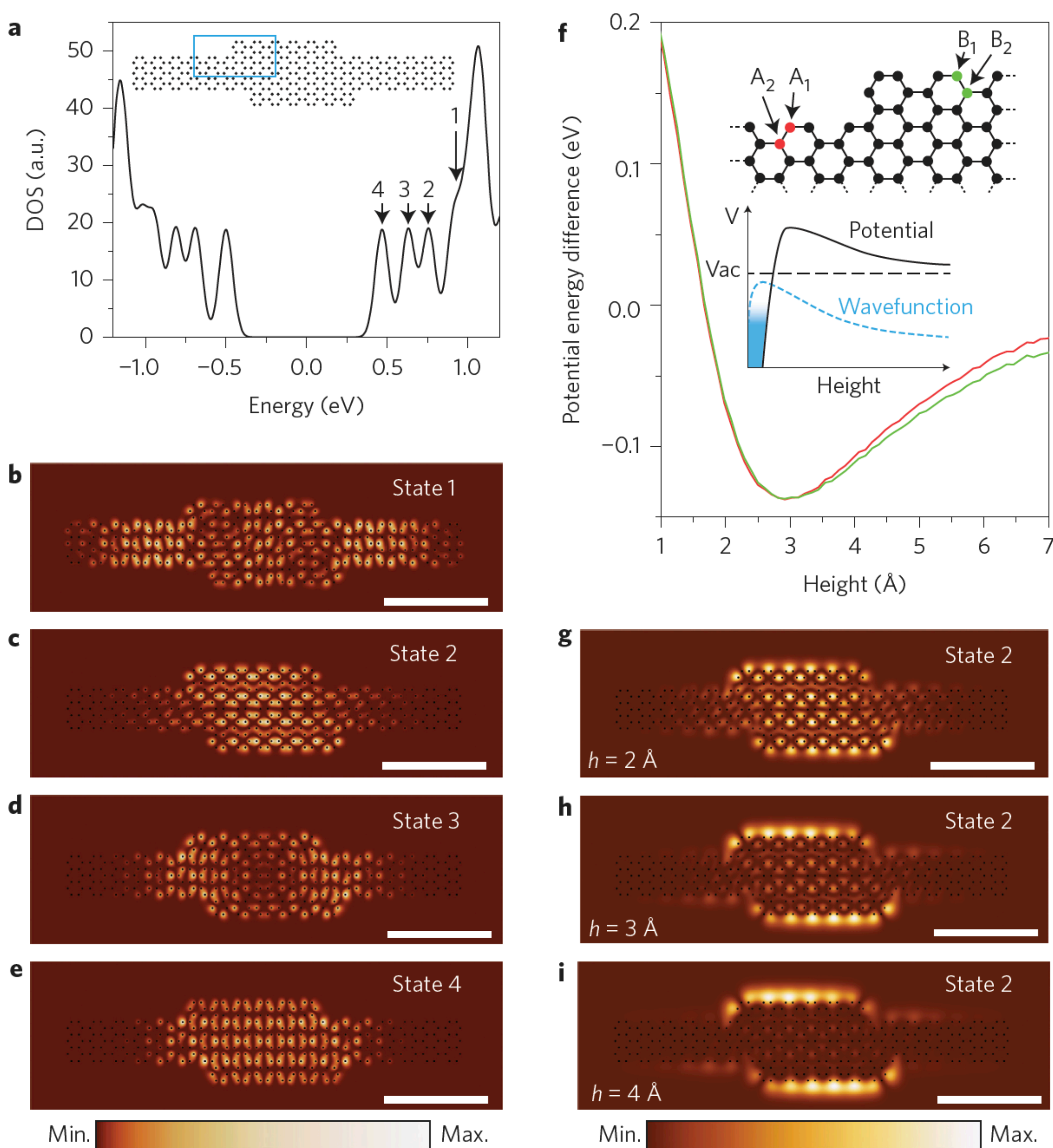

Figure 3.4 | Theoretical electronic structure of 7–13 GNR heterojunction. a, Calculated DOS of the isolated 7–13 GNR heterojunction structure shown in the inset, with a Gaussian broadening of 0.06 eV. Four unoccupied states are labelled 1–4 in the figure (states here are labelled analogous to the peaks observed experimentally; Fig. 3.2). b–e, Height-integrated LDOS maps of theoretical states 1–4 for the 7–13 GNR heterojunction. The plots are normalized with respect to their maximum intensities (270, 348, 500 and 416 arbitrary units in b–e, respectively). f, Calculated electron potential energy difference between edge and inner atoms as a function of

height h above the carbon plane of the 7–13 GNR heterojunction. The red curve shows the potential energy difference between atomic positions A_1 and A_2 (see upper inset). The green curve shows the potential energy difference between atomic positions B_1 and B_2 (see upper inset). The inset structural drawing depicts the boxed region in the inset to a. Lower inset: Height dependence of the potential at one atomic location and the resulting decay of the wavefunction along the surface normal into the vacuum. The horizontal black dashed line indicates the vacuum energy level. Blue shading represents electron filling relative to the vacuum energy level. g–i, Calculated LDOS of 7–13 GNR heterojunction state 2 at heights of 2 Å (g), 3 Å (h) and 4 Å (i) above the plane of the GNR heterojunction. The LDOS plots are normalized with respect to their maximum intensities (180, 9.05 and 0.84 arbitrary units in g–i, respectively). All scale bars, 2 nm.

The strong dependence of the LDOS distribution with height h can be explained by the difference in potential energy felt by electrons at different (x, y) positions above a GNR heterojunction, as shown in Fig. 4f. The red curve in Fig. 4f shows the calculated potential energy difference (within LDA) between positions A_1 and A_2 in the N = 7 segment (marked in the inset structural drawing) as a function of height. A_1 marks a carbon atom at the very edge of the segment and A_2 marks an adjacent carbon atom just one dimer row into the interior. The potential energy at the edge is lower than the potential energy in the interior for heights greater than 1.6 Å above the GNR heterojunction. This implies a smaller out-of-plane (h direction) potential barrier in the vacuum for electrons closer to the edge. The wavefunction at the edge therefore decays more slowly along the h direction into the vacuum than the wavefunction in the interior, resulting in higher LDOS contrast between the edges and the interior, as shown in Fig. 4i (see Fig. 4f inset). The same argument also applies to the N = 13 segment (green curve in Fig. 4f). The stronger spectroscopic dI/dV signal observed near the edges of armchair GNRs is thus attributed to spatial variation in the electronic potential, even though the states themselves are not localized to the edges. Additional discussion in presented in the next section.

3.1.4 Discussion of the Height Dependence of the Electron Potential Energy

The strong dependence of the LDOS distribution with height h can be explained by the difference in potential energy felt by electrons at different (x, y) positions above a GNR heterojunction, as shown in Fig. 3.4f. The red curve in Fig. 3.4f shows the calculated potential energy difference (within LDA) between positions A_1 and A_2 in the N = 7 segment (marked in the inset structural drawing) as a function of height. A_1 marks a carbon atom at the very edge of the segment and A_2 marks an adjacent carbon atom just one dimer row into the interior. The potential energy at the edge is lower than the potential energy in the interior for heights greater than 1.6 Å above the GNR heterojunction. This implies a smaller out-of-plane (h direction) potential barrier in the vacuum for electrons closer to the edge. The wavefunction at the edge therefore decays more slowly along the h direction into the vacuum than the wavefunction in the interior, resulting in higher LDOS contrast between the edges and the interior, as shown in Fig. 4i (see Fig. 3.4f inset). The same argument also applies to the N = 13 segment (green curve in Fig. 3.4f). The stronger spectroscopic dI/dV signal observed near the edges of armchair GNRs is thus attributed to spatial variation in the electronic potential, even though the states themselves are not localized to the edges.

We are able to understand the difference in the height-dependent (along the direction normal to the plane) electron potential energies above atomic positions in the interior compared to those above atomic positions at the edges of the GNRs by considering the charge distribution of the nanoribbon. The carbon nuclei, having positive charge, are point-like and fixed in the graphene plane while the valence electrons are delocalized and exhibit a density distribution that extends into the out-of-plane (i.e., the planar normal) direction. This density distribution for the finite-width ribbon leads to a height-dependent electron potential energy profile which holds true for atomic positions both in the interior and at the edges: the potential energies are negative (i.e., attractive) very close to the graphene sheet, and become positive (i.e., repulsive) at some distance further away from the graphene sheet. However, the electrostatic interaction felt by an electron above an edge atomic position is attributed more to the charges in the interior of the nanoribbon than to the small amount of electron charge that is spilled into the vacuum near the edge. Therefore, compared with the electrostatic potential energy profile above the interior atomic positions, the potential energies above the edge atomic positions are smaller in absolute value at all heights, except near a small transition region where the potential goes from negative (near plane) to positive (far from plane) value. As a result, the electrostatic potential difference between the edge and the interior ($V_{edge} - V_{interior}$) is positive at a small height above the graphene plane and turns negative above certain critical height (which may be system dependent). We expect the above analysis to be true for any atomically thin quasi-2D system.

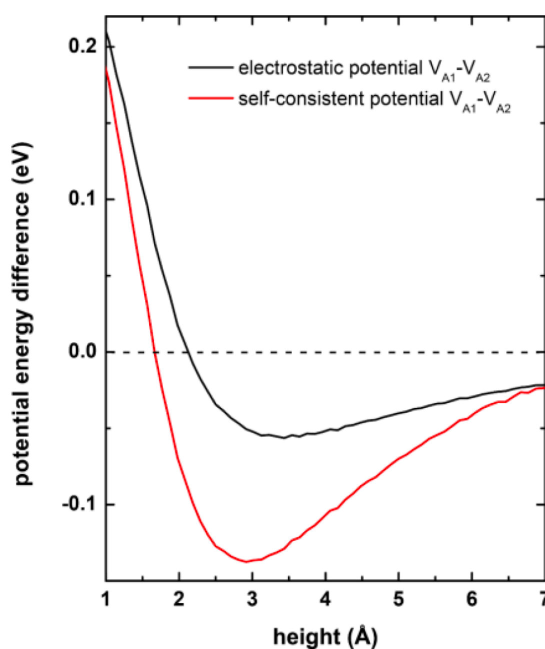

Figure 3.5| Height dependence of the electron potential energy. Comparison of DFT-calculated electrostatic and self-consistent potential energy difference as a function of height along the planar normal direction above an atomic position at the GNR edge (A_1) compared to that above an atomic position in the interior (A_2). The black curve shows the electrostatic potential energy difference between positions A_1 and A_2 as indicated in the sketch in Fig. 3.4f of the main text, while the red curve depicts the self-consistent potential energy difference for these same two positions.

In Fig. 3.5, we show the height-dependent electrostatic potential energy difference as well as the self-consistent potential energy (electrostatic plus exchange-correlation) difference between the edge atomic position A_1 and the interior atomic position A_2 obtained using density functional theory for the 7-13 GNR heterojunction (Fig. 3.4f). The electrostatic potential energy difference is positive at small height and turns negative at ~2.1 Å above the ribbon, consistent with our qualitative analysis above. The self-consistent potential energy is different from the electrostatic potential energy because it takes into account the exchange-correlation effects at the LDA level. These additional effects lower the potential seen by the electron above the edge atom even further when compared to the interior atomic position. The overall effect is that for a given electronic state, the wavefunction is expanded in the normal direction on the edge atom when compared to the extension above the atoms in the interior of the ribbon.

3.1.5 Conclusion

These results imply that the band alignment in 7–13 GNR heterojunctions is very similar to type I semiconductor junctions, because the lowest unoccupied (highest occupied) state in the N = 13 segment is lower (higher) than that in the N = 7 segment. (Such spatially varying energy gap size is a hallmark of bandgap engineering and is different, for example, from the band offsetting that leads to p–n-type junctions.[30]) The N = 7 segment might therefore serve as an energy barrier for charge carriers trapped in the N = 13 segment (our spectroscopic data suggest that the energy required to excite an electron from state 4, which is localized in the N = 13 segment, to state 1 and thus into the N = 7 segment, is ~0.7 eV). This provides a possible means for constructing graphene quantum-dot-based systems with sub-nanometre feature sizes and single-atom thickness. A potential benefit of this heterojunction architecture is that electrical contacts to the quantum dots are readily available via the outer GNR segments. Bottom-up GNR-based synthesis methods thus have potential for creating functional gap modulated semiconductor junctions with atomically controlled features that are smaller than possible through conventional top-down lithography.

3.2 Concentration Dependence of Dopant Electronic Structure in Bottom-up Graphene Nanoribbons

3.2.1 Abstract

The previous section presented successful synthesis and characterization of width modulated AGNR heterojuntions from molecular precursors. This was a significant development in the field of bottom-up GNRs since it provided experimental evidence that the electronic properties of the GNR can be controlled via their width. Analogous to traditional semiconductors, GNR electronic structure can also be tailored by the introduction of heteroatom impurities.[96-98] The effect of impurity doping on GNRs, however, is not easily understood using the common framework of traditional semiconductor materials.[99, 100] GNRs, for example, are intrinsically in the regime of strong quantum confinement and exhibit trigonal planar symmetry rather than the more common tetrahedral symmetry, leading to conduction through extended π-networks unlike conventional semiconducting systems.

Bottom-up synthesis provides an effective method to explore heteroatom doping in GNRs since it enables site-specific incorporation of heteroatom dopants through designed precursor molecules that can be assembled into atomically-precise doped GNRs.[11, 16, 24, 25, 101, 102] The introduction of nitrogen atoms into GNR edges, for example, has been shown to shift the energy-level alignment of GNR band structure,[30, 96]while the incorporation of boron atoms into the GNR backbone has been shown to introduce new in-gap states.[27, 28, 103] The electronic structure of boron-induced dopant states, however, including the effects of substrate hybridization, remains poorly understood.[25, 27, 28, 101-103]

In this section, we report the bottom-up synthesis and characterization of boron-doped N = 7 AGNRs at two antipodal doping regimes: the dilute and highly dense limits. STS measurements and DFT calculations were performed to study the local electronic properties of boron-doped GNRs in both concentration regimes. Our calculations show that there exist two boron-induced dopant states in the gap, one with s-like (even parity) and the other with p-like (odd parity) orbital character that persist in both concentration limits. In the dilute limit our freestanding calculations (i.e., no substrate coupling) show that the boron-induced dopant states are nearly degenerate. As the density of dopant atoms increases in the freestanding regime, the energy separation between the boron induced states increases, and the dopant states form impurity bands since the dopants are arranged periodically. Our experiments, however, are not consistent with the freestanding GNR predictions. In the dilute limit, we experimentally observe two dopant states with different symmetries that are strongly split in energy and broadened into asymmetric peaks (i.e., one is broader than the other). In the dense limit, the experimental upper dopant energy band is shifted in energy with respect to the freestanding theoretical prediction and is significantly broader than expected. This anomalous behavior is explained by hybridization between the boron-induced dopant states and the surface states of the gold substrate. First-principles calculations taking substrate coupling into account confirm that there is a strong and symmetry-dependent hybridization between GNR dopant states and Au(111). Consequently, as seen experimentally, this induces strong energy splitting and asymmetrical broadening whose magnitude depends on the dopant state symmetry.

3.2.2 Freestanding Calculation

Fig. 3.6 shows a DFT calculation (using LDA) of the electronic structure of a freestanding N = 7 AGNR (i.e., no substrate included in the calculation) for three boron dopant concentrations: (i) the undoped case (Fig. 3.6d), (ii) the dilute doping limit (Fig. 3.6e), and (iii) the dense doping limit (Fig. 3.6f) (Fig. 3.6a−c show the unit cells used for the three calculations). GW[21, 104, 105] calculations were seen to give similar results but with larger bandgap values due to self-energy effects. We focus here on the DFT results since substrate screening typically reduces the GW bandgaps to values close to the DFT level when the system is put on a metallic surface (as done in our experiments). The undoped GNR band structure shows the familiar conduction (CB) and valence (VB) bands that have been calculated within DFT before,[26] while the dilute-doped GNR exhibits band edges at similar energies. The most significant difference between the undoped and dilute-doped band structure is the presence of two new defect levels at ~0.5 eV above the VB edge for the dilute-doped case (the appearance of multiple bands above (below) the conduction (valence) band edge for the dilute doped limit is due to band-folding from the supercell geometry used in the calculation). The new impurity states are nearly degenerate ($\Delta E < 20$ meV) and exhibit a large contribution from the π-orbitals of the boron dopant atoms. Analysis of the wave function for the lower defect state shows that it has p-like symmetry (odd parity) along the GNR axial direction (Fig. 3.7b), while the upper defect state has s-like symmetry (even parity) along the longitudinal axis (Fig. 3.7c) (a similar theoretical result for the dilute, freestanding limit was reported in ref 103).[103]

As the dopant concentration increases, the energy splitting between the two impurity states correspondingly increases, and the defect states evolve into impurity bands with an energy gap of 0.5 eV, as shown in the band structure for the densely doped GNR in Fig. 3.6f (the band labeling convention used here is different compared to a previous publication[21] in order to make the role of the dopants more clear).

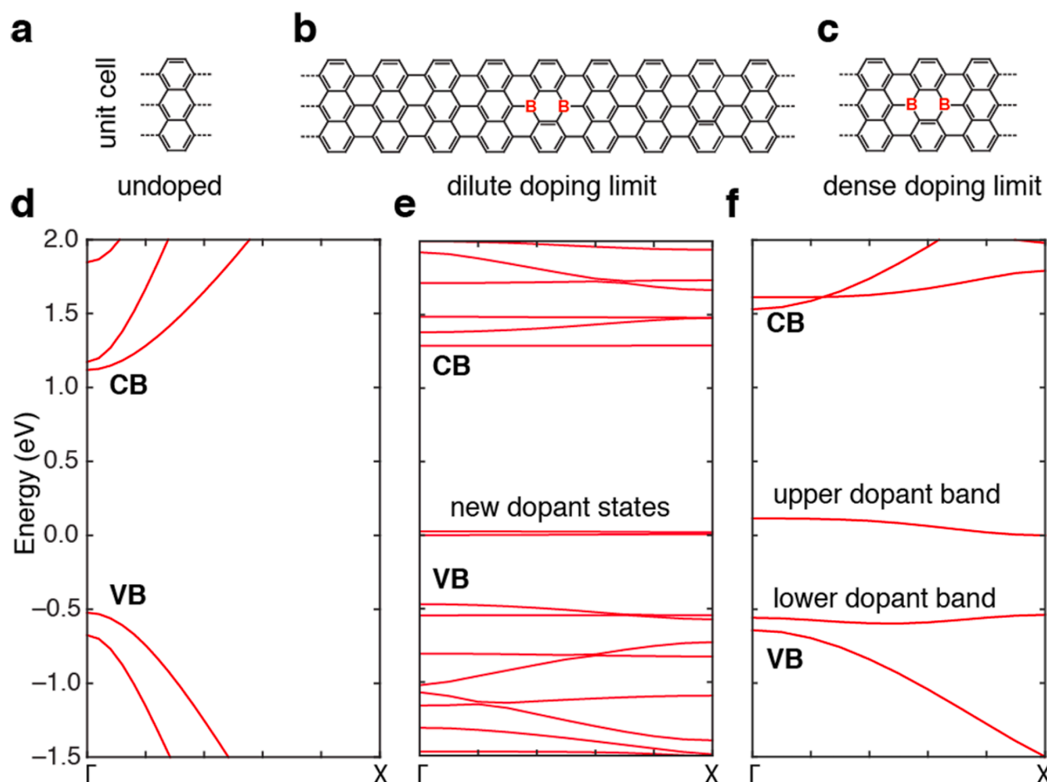

Figure 3.6| Band structure evolution of freestanding boron-doped N = 7 armchair graphene nanoribbons at different dopant densities. Unit cells of a, undoped, b, dilute-doped, and c, densely doped N = 7 GNRs. d−f, Corresponding band structures calculated by DFT within LDA. The relative Brillouin zone sizes in panels d, e, f are 9:1:3, and when this is taken into account, the dispersion of the VB top and CB bottom does not change significantly after doping.

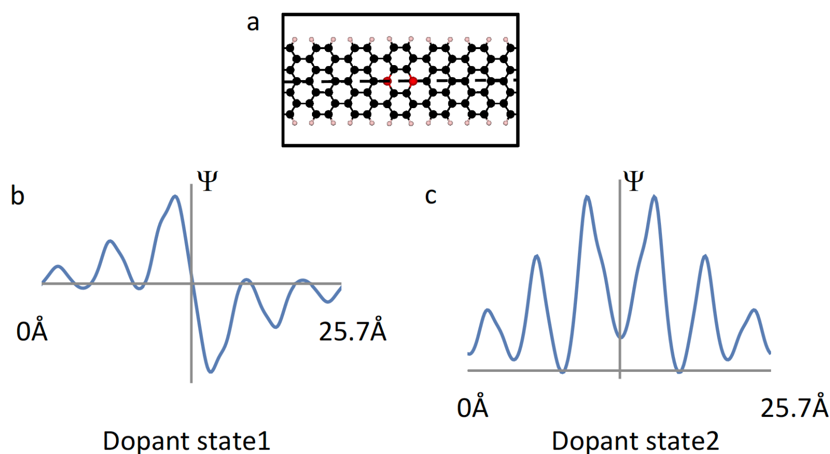

Figure 3.7| Calculated wavefunctions of dopant states. a, The unit cell for a freestanding dilute boron-doped 7AGNR. Red, black, and purple spheres represent boron, carbon, and

hydrogen atoms, respectively. b, c, Calculated wavefunctions of the two dopant states at the Γ point for a freestanding GNR. The wavefunctions are plotted along the axial line of the unit cell in a, (black dashed line) 1Å above the GNR.

3.2.3 Synthesis and Characterization of B-doped AGNRs with Different Dopant Concentrations

In order to experimentally test these theoretical predictions, GNRs were fabricated in both the dilute and dense regimes. The dilute-doped regime was accessed by combining molecular precursors for undoped N = 7 GNR (10,10′-dibromo-9,9′- bianthryl, DBBA) with precursors for boron-doped N = 7 AGNR) in a 10:1 ratio using standard GNR growth conditions[11, 16, 86] (polymerization of the precursors occurs at ~180 °C, while cyclodehydrogenation occurs at ~360 °C (as presented in Fig. 3.8).

Figure 3.9 shows an STM topographic image of a resulting dilute-doped N = 7 GNR on Au(111) with vertical dashed lines indicating the location of a boron defect (a sketch of the wireframe structure is shown in Fig. 3.9a). The region surrounding the dopant atoms has a reduced apparent height in the STM image, suggesting that the boron atoms sit closer to the Au(111) surface than the GNR carbon atoms.

The experimental electronic structure of dilute-doped GNRs was investigated by measuring STM differential conductance (dI/dV) spectra at the position of boron dopants and then comparing that to spectra acquired on undoped GNR segments at the positions marked in Fig. 3.9b (the respective positions are color-coded with the dI/dV curves). Fig. 3.9c shows a characteristic dI/dV point spectrum (green curve) recorded at the edge of an undoped segment of the GNR. This spectrum exhibits a peak at $V_s = 1.68 \pm 0.02$ V, which we identify as the CB edge, as well as a peak at $V_s = -0.80 \pm 0.02$ V, which is identified as the VB edge (Vs is sample voltage). This leads to an overall GNR bandgap of 2.48 ± 0.02 eV, similar to bandgap measurements on undoped N = 7 AGNRs performed previously.[21, 26, 29] The identity of these familiar spectroscopic peaks was confirmed via energy-resolved dI/dV mapping, which allows visualization of the surface LDOS as depicted in Fig. 3.9d−g. Two new states attributed to the dopant atoms are observed in the STM spectroscopy measured at the center (top inset of Fig. 3.9c, blue curve) and edge (bottom inset of Fig. 3.9c, red curve) of the boron defect shown in Fig. 3.9b. The dI/dV spectrum measured at the impurity edge (red curve) shows the presence of a new peak (labeled State 1) that is centered at $V_s = -0.52 \pm 0.02$ V and that has a full width at half-maximum (fwhm) of 0.23 V. The dI/dV spectrum measured at the center of the dopant site (blue curve) exhibits a pronounced upward slope starting at $V_s \approx 0.3$ V and extending to $V_s \approx 1.2$ V that is not observed in the reference spectrum taken at the center of the undoped segment with the same tip (black curve). This second dopant-induced feature is labeled as State 2. We note that these spectroscopic features (States 1 and 2) persist even as adjacent dopants in the dilute regime have inter-impurity distances as small as 2.5 nm center-to-center (see Figure S3 in supplemental information of ref.[22]).

The spatial distributions of dopant-induced States 1 and 2 were determined using dI/dV mapping. Fig. 3.9f shows a dI/ dV map measured at the energy of State 1 that exhibits bright

lines along the edges of the dopant segment as well as two small high intensity spots near the boron atoms (the two central bright spots are located at the sites of the two horizontal boron−carbon bonds, see Figure S8 in supplemental information of ref. [22]). Fig. 3.9e shows a representative dI/dV map of State 2 recorded at 0.8 V that exhibits bright, diffuse LDOS that is elliptically symmetric and centered at the position of the dopant (dI/dV maps recorded for State 2 at different energies in the range 0.3 V < V_s < 1.35 V show similar LDOS patterns, see Figure S8 in supplemental information of ref[22]).

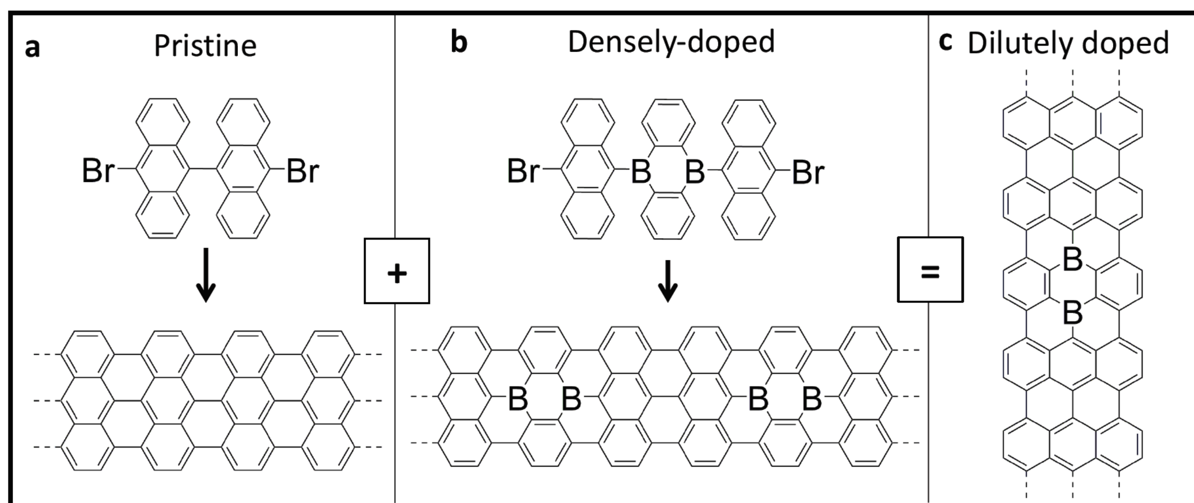

Figure 3.8| Molecular precursors used in boron doped study. a, Pristine precursor 10,10'-dibromo-9,9'-bianthryl, DBBA, leads to pristine N=7 AGNRs. b, Boron-doped precursor molecule with two boron atoms leads to densely doped N=7 AGNR. c, Combining these two precursors in an appropriate ratio (10:1 (pristine: doped) is typical) leads to dilute-doped N=7 AGNRs.

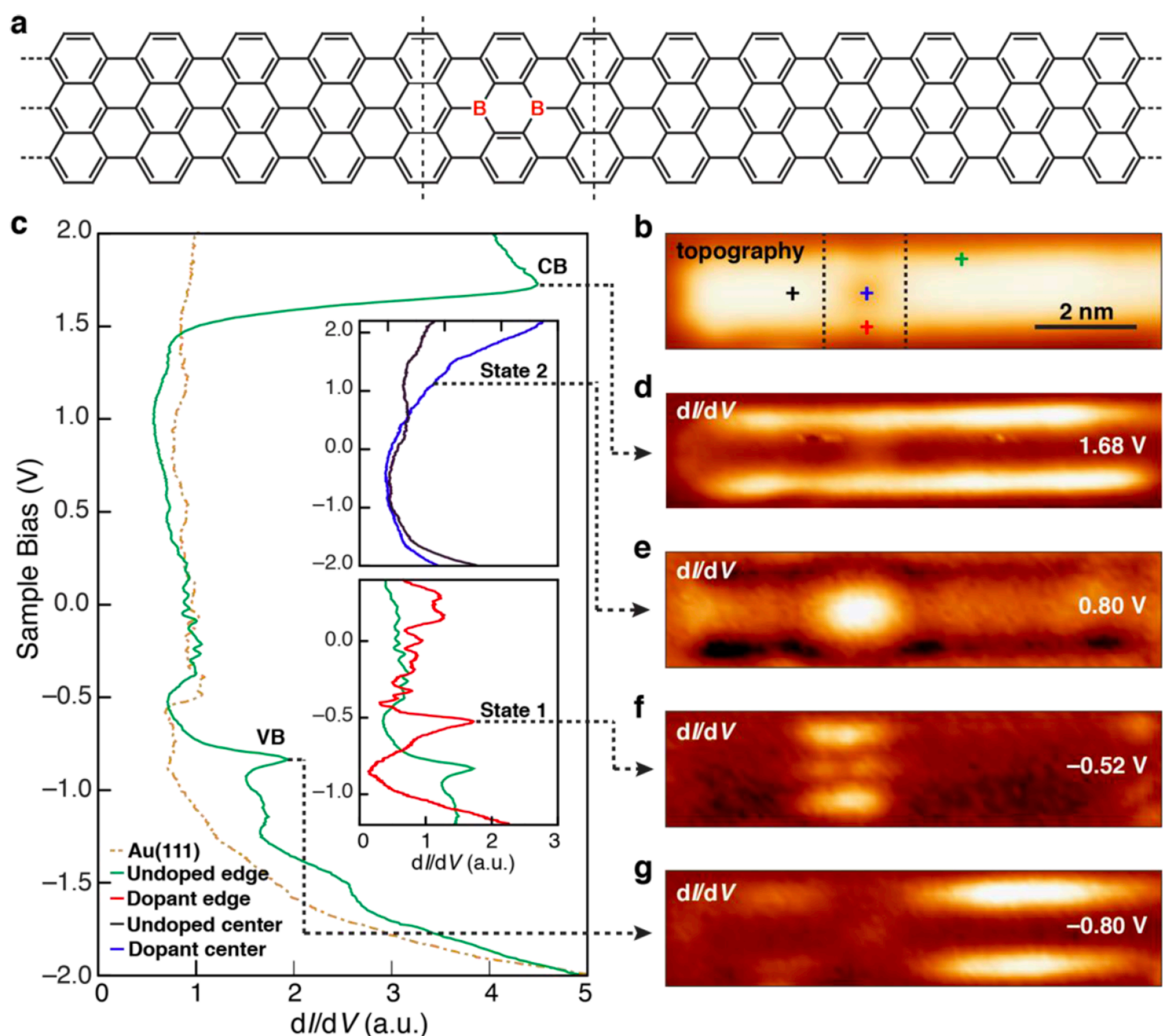

Figure 3.9| Electronic structure of a dilute boron-doped N = 7 AGNR on Au(111). a, Wireframe sketch of a dilute-doped GNR. b, STM topographic image of dilute-doped GNR (V_s = −0.4 V, I_t = 60 pA). c, STM dI/dV spectroscopy measurement taken at the edge of an undoped segment of the GNR (green). Top inset shows dI/dV spectroscopy taken at the center of a boron dimer segment (blue) compared to the center of an undoped GNR segment (black). Bottom inset shows dI/dV spectroscopy taken at the edge of a boron-doped segment (red) compared to the edge of an undoped GNR segment (green). Two new states, dopant States 1 and 2, are observed at −0.52 and 0.8 eV, respectively. dI/dV maps of the GNR are shown at energies corresponding to d, the CB edge (V_s = 1.68 V), e, State 2 (V_s = 0.8 V), (f) State 1 (V_s = −0.52 V), and g, the VB edge (the fact that the VB feature on the left side is darker is due to the asymmetrical defect placement, which likely increases quantum confinement effects on the left side) (V_s = −0.8 V). T = 7 K for all measurements. Panels d−g have the same scale as panel b.

We next explored GNRs doped with boron atoms in the dense limit. These GNRs were grown using only the boron doped precursor (Figure 3.8b). A wireframe sketch of the resulting boron-doped GNR structure is depicted in Fig. 3.10a, and an STM topograph is shown in Fig. 3.10b. As seen previously[27, 28] the boron-doped segments of this GNR sit slightly closer to the substrate than the unsubstituted regions and lead to a 1.30 ± 0.05 Å amplitude periodic height modulation along the GNR long axis in topography. We first characterized the electronic structure of densely doped GNRs via dI/dV point spectroscopy. Fig. 3.10c shows typical dI/dV spectra measured at a position along the backbone (blue curve) and at the edge (red curve) of a densely doped GNR with the same tip (spectroscopy positions are marked in Fig. 3.10b; the spectroscopic features had no significant dependence on how the tip was axially aligned with respect to dopants (see Figure S11 in supplemental information of ref[22])). The dI/dV spectrum recorded at the GNR edge shows a well-defined peak at 1.63 ± 0.04 eV above the Fermi level, EF.[28] The spectrum recorded along the densely doped GNR backbone is quite different and reveals a new, broad spectroscopic feature at 1.0 ± 0.2 eV above E_F (this peak is absent in STS of undoped GNRs[26, 29, 94]). We did not observe any reproducible spectroscopic features below E_F in our dI/dV point spectra for densely doped GNRs on Au(111). We used dI/dV mapping to visualize the electronic structure of densely doped GNRs at different energies. Fig. 3.10d shows a dI/dV map recorded at 1.60 eV, the energy of the upper spectroscopic peak. Here, the intensity of the LDOS is highest along the GNR edges, similar to what has previously been observed for energies near the CB edge in undoped N = 7 AGNRs.[21, 26, 28, 29] The dI/dV map obtained at an energy near the broad spectroscopic peak at 1.0 eV shows a pronounced shift in LDOS away from the GNR edges to the GNR backbone (Fig.10 3e). Fig. 3f shows a dI/dV map obtained in the filled states at a voltage of $V_s = -0.23$ V. Although we observe no peak at this energy in the dI/dV point spectroscopy, a clear transition is observed in the spatial LDOS distribution compared to dI/dV maps obtained at higher voltages (see Figure S10 in supplemental information of ref [22]). At this filled state energy, the LDOS is pushed outward toward the GNR edges, and a longitudinal nodal structure is seen that does not appear in the map at $V_s = 1.0$ V. The new densely doped spectroscopic features observed at $V_s = -0.23$ and 1.0 V do not occur for undoped N = 7 GNRs and so must arise from the influence of boron dopants. We label them here as State A ($V_s = -0.23$ V) and State B ($V_s = 1.0$ V).

Our experimental results for dilute and densely doped GNRs exhibit some qualitative agreement with our theoretical calculations for freestanding boron-doped GNRs, but there are significant discrepancies. For example, in the dilute-doping limit, our experiments faithfully reproduce the two expected defect states in the gap with one exhibiting s-like symmetry (State 2, which has no node) and the other exhibiting p-like symmetry (State 1, which has a node). However, our experimental measurements show a significant splitting between the two states (~1 eV), whereas the theoretical defect states are essentially degenerate. Furthermore, it is not clear why the experimental peak seen for State 1 is so much narrower than the broad, sloping spectroscopic feature that defines State 2.

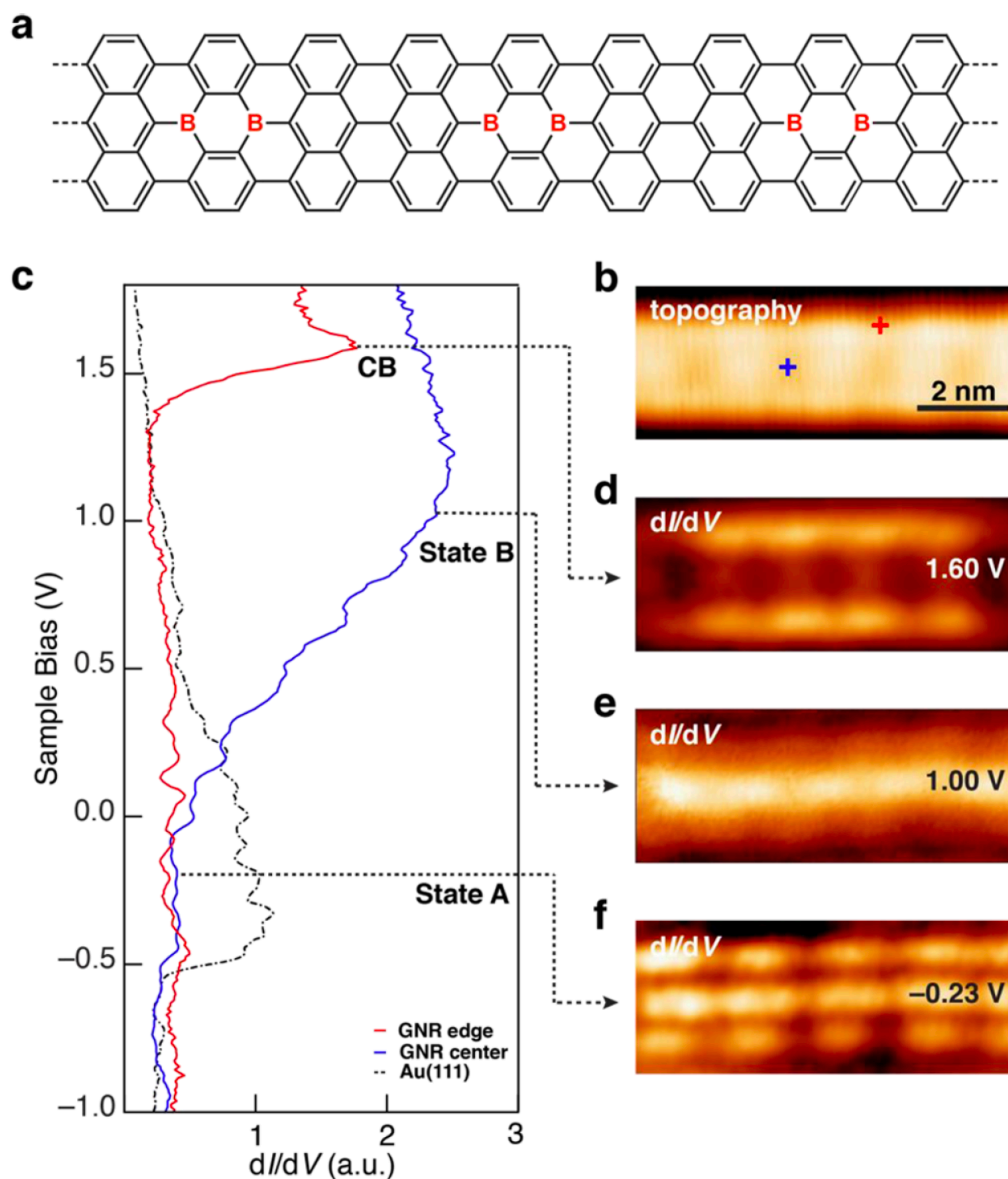

Figure 3.10| Electronic structure of densely boron-doped N = 7 AGNR on Au(111). a, Wireframe sketch of a densely doped GNR. b, STM topograph parameters: $V_s = 1.60$ V, $I_t = 20$ pA. c, STM dI/dV spectroscopy measured at the edge and center of a densely doped GNR as shown in panel b. d, dI/dV map taken at $V_s = 1.60$ V visualizes state at the CB edge. e, dI/dV map taken at $V_s = 1.0$ V visualizes unoccupied dopant-induced state (State B). f, dI/dV map taken at $V_s = -0.23$ V visualizes occupied dopant-induced state (State A). T = 4.5 K for all measurements. Panels d−f have the same scale as panel b.

In the densely doped regime, the experimental peak observed at V_s = 1.6 eV (Fig. 3.10c, red curve) is consistent with the theoretically predicted CB (Fig. 3.6f). The new spectroscopic peak at $V_s \approx 1.0$ V (Fig. 3.10c, blue curve) also roughly corresponds to spectroscopic features expected to arise from a new dopant-induced band[103] (e.g., the upper dopant band in Fig. 3.6f). However, there are major discrepancies between experiment and theory here as well. Most significant is the energy alignment of the observed spectroscopic features. The energy difference between the two experimental spectroscopic peaks shown in Fig. 3.10c is only ~0.5 eV, whereas the theoretically predicted energy difference between the CB and the upper dopant band in Fig. 3.6f is ~1.5 eV. Also, if the state imaged at V = −0.23 eV (Fig. 3.10f) is assigned to the lower dopant band, then the energy difference between the two dopant-induced bands in the experiment (~1.2 eV) is significantly larger than the calculated energy difference (0.5 eV). Moreover, the anomalously broad spectroscopic peak at V_s = 1.0 V is inconsistent with the simulation since the upper dopant bandwidth is predicted to be quite narrow (Fig. 3.6f). The spectroscopic features reported here (including dI/dV maps) were consistently observed on 13 different dilute-doped GNRs and 11 different densely doped GNRs whose electronic properties were inspected using a variety of different STM tips. All STM topographic images were processed using WSxM.[106]

We conclude that the freestanding GNR model used in the calculations is insufficient to describe our experimental data, most likely because it neglects the substrate. Therefore, in order to better understand our experimental results, we performed additional calculations that fully take into account coupling from the underlying Au(111) substrate upon which the boron doped GNRs rest. The electronic structures of both dilute doped and densely doped GNRs on Au(111) were calculated via DFT using the supercells shown in Fig. 3.11d and 3.12d, respectively. Similar to our experimental data, the boron atoms in a fully relaxed simulated GNR sit closer to the Au(111) surface than the carbon atoms in undoped segments of the ribbon. This reduction of the boron−gold distance indicates significant interaction between the boron dopants and the gold substrate atoms.

3.2.4 Symmetry-Dependent Hybridization between the Dopant States and Au(111) Substrate

In order to simulate the dilute-doped dI/dV spectroscopy of Fig. 3.9c, we calculated the energy-resolved LDOS (including gold substrate effects) averaged over a 7.5 Å × 7.5 Å area 4 Å above the boron-doped segment following the topography of the GNR (all calculations were performed by T. Cao, F. Zhao and S. G. Louie). The results are plotted in Fig. 3.11a. Substantial features are seen to appear in previously gapped regions due to hybridization between the GNR and the underlying Au(111) substrate (the CB (1.6 eV) and VB (−0.9 eV) edges are obtained from the undoped segment as explained in the supplemental information of ref[22]). In particular, two features are observed that arise from the boron defect: a broad resonance in the unoccupied states and a narrower resonance in the occupied states. The occupied resonance appears in the range −0.4 eV < E < −0.1 eV and exhibits the LDOS pattern shown in Fig. 3.11c (obtained at E = −0.21 eV). This LDOS map has bright features at the outer edges and two interior peaks of high

intensity located on the C−B bonds that lie along the GNR axis. As seen in Fig. 3.11f, the wave function at this energy has odd parity (p-like) under mirror symmetry.

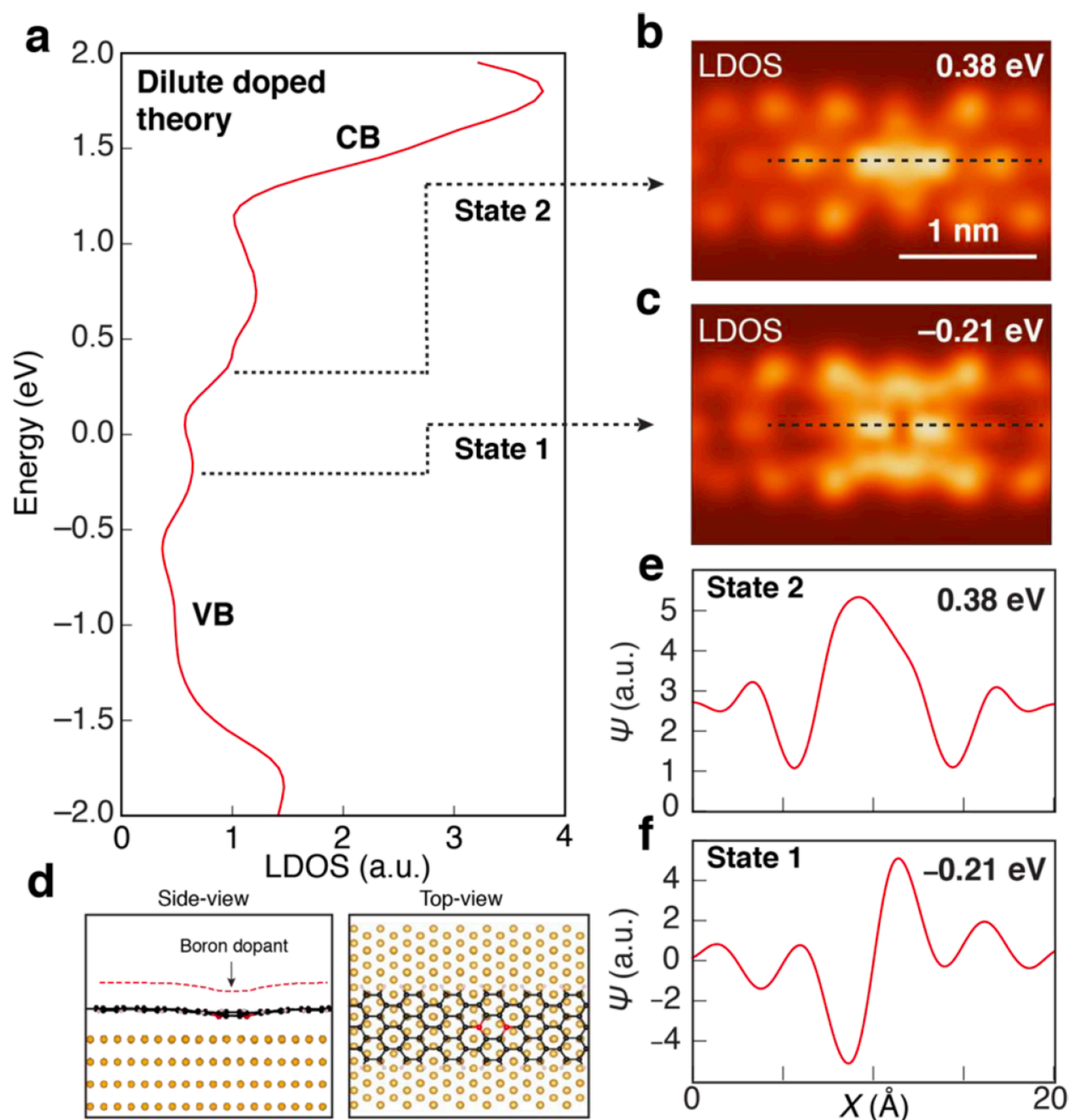

Fig. 3.11| DFT-LDA calculation of dilute-doped N = 7 GNR on Au(111) substrate. a, Calculated LDOS 4 Å above the boron-doped segment shows dopant States 1 and 2 (theoretical LDOS is broadened by a Gaussian function with standard deviation σ = 125 meV). Calculated LDOS map is shown for b, E = 0.38 eV (integrated over a 0.05 eV energy window) and c, E = −0.21 eV (integrated over a 0.05 eV energy window). d, Side-view and top-view of the supercell and the relaxed structure used to calculate the dilute-doped GNR. The supercell includes four layers of Au atoms. Red dashed line shows the surface upon which the LDOS maps are calculated. e, Calculated wave function along the dashed line in panel b for E = 0.38 eV. f, Calculated wave function along the dashed line in panel c for E = −0.21 eV. Panels b and c have the same scale.

The unoccupied LDOS is quite different from what is seen in the occupied states. Here a much broader feature arises over the range 0.3 eV < E < 0.9 eV (a slight dip can be seen at E ≈ 0.5 eV). Fig. 3.11b shows a representative LDOS map of this defect state (obtained at E = 0.38 eV). As seen in Fig. 3.11e, this dopant state has a more delocalized wave function than the occupied state feature and exhibits approximate even parity (s-like).

The simulated behavior of the dilute-doped GNR on Au(111) supports our hypothesis that differences observed between the experiment and the "freestanding" theory arise from the interaction between boron-doped GNRs and the gold substrate. The reasonably good agreement between theory and experiment for the defect state energies and broadening allows us to identify the occupied and unoccupied features in the theoretical LDOS of Fig. 3.11a with experimentally observed State 1 and State 2 of Fig. 3.9c. Further evidence for this assignment is found in the striking resemblance of the theoretical occupied state LDOS pattern (Fig. 3.11c) to State 1 (Fig. 3.9f), as well as the resemblance of the theoretical unoccupied LDOS pattern (Fig. 3.1b) to State 2 (Fig. 3.9e). The energy splitting between the central energy of the two simulated defect state peaks (~1 V) is also similar to what is observed experimentally, indicating that the boron-induced defect states (which are nearly degenerate for a freestanding GNR) are strongly split by interaction with the Au(111) substrate. This interaction also explains the different broadening of the two defect states, which is faithfully reproduced by the calculation and which arises due to the different symmetries of the dopant states. Because State 1 has p-like character, it hybridizes more weakly with the s-like surface states of gold (leading to a narrower peak), whereas State 2 has s-like character and so hybridizes more strongly with gold (leading to a broader peak). The s- and p-like symmetries of the boron defect states are thus primary factors in determining the dopant electronic structure for the strongly hybridized boron-doped GNR/Au(111) complex. First-principles calculations were performed using DFT in the local density approximation, implemented in the Quantum Espresso[107] package. GW calculations were performed using the BerkeleyGW package.[108]

Motivated by the agreement between experiment and theory for the dilute-doped GNRs in the presence of Au(111), we examined the electronic structure of densely doped GNRs supported by Au(111). The energy-resolved LDOS 4 Å above the boron-doped segment was calculated using the same method as in the dilute case and is shown in Fig. 3.12a. The energy-dependent LDOS of Fig. 5a is very similar to what is seen in the dilute-doped case (Fig. 3.11a). For example, a broad unoccupied resonance and a narrower occupied resonance arise due to substrate interactions, and the resonances have almost identical energy and width as the State 1 and 2 features of the dilute regime. A representative LDOS map of the theoretical unoccupied states obtained at E = 0.35 eV (Fig. 3.12c) is dominated by nearly uniform bright intensity along the longitudinal axis of the densely doped GNR (i.e., bright intensity occurs at the boron dimer sites as well as at the carbon dimer sites between them). This theoretical LDOS map is qualitatively very similar to the experimental unoccupied state dI/dV map of Fig. 3.10e, and so we identify the broad, unoccupied state feature of Fig. 3.12a as State B. A representative map of the theoretical occupied states obtained at E = −0.22 eV (Fig. 3.12d) shows a shifting of LDOS intensity to the GNR edges and a new lateral periodicity whose wavelength matches the distance between boron dimers (due to reduction in LDOS at the carbon dimer sites between boron dimers). This theoretical LDOS map is qualitatively similar to the experimental occupied state dI/dV map of Fig. 3.10f, and so we identify the narrow, occupied state feature of Fig. 3.12a as

State A. The lack of a clear peak due to State A in the experimental dI/dV point spectroscopy (Fig. 3.10c) is likely due to increased hybridization between densely doped lower dopant band states and the Au(111) surface compared to dopant states in the dilute-doped regime.

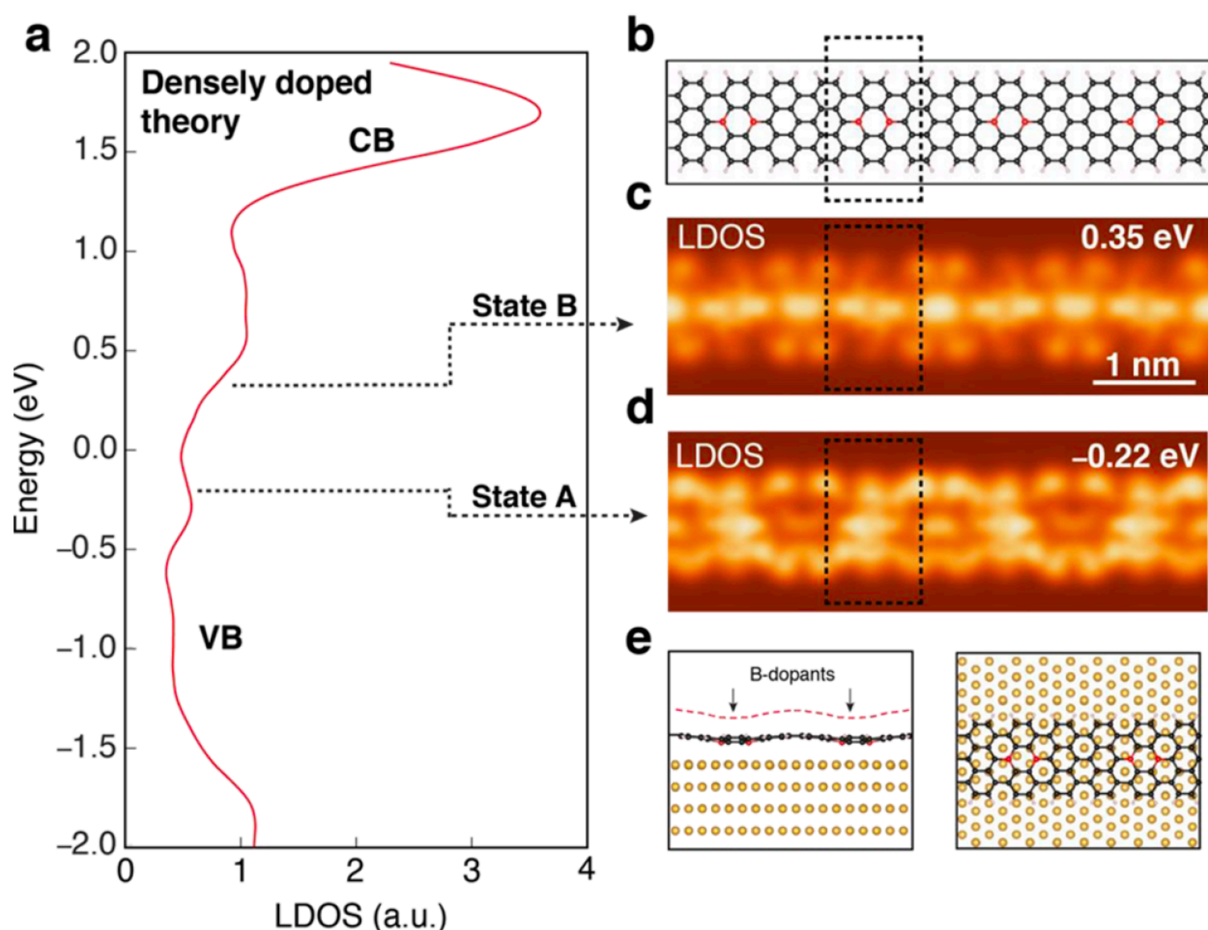

Figure 3.12| DFT-LDA calculation of densely doped N = 7 GNR on Au(111) substrate. a, Calculated LDOS 4 Å above boron-doped segment shows dopant States A and B (theoretical LDOS is broadened by a Gaussian function with standard deviation σ = 125 meV). b, Wireframe sketch shows location of boron atoms. Calculated LDOS maps (each including four boron dimers) are shown for c, E = 0.35 eV (integrated over a 0.05 eV energy window) and d, E = −0.22 eV (integrated over a 0.05 eV energy window). e, Side view and top view of the supercell and the relaxed structure (includes four layers of Au atoms) used to calculate the relaxed densely doped GNR. The red dashed line shows the surface upon which the LDOS maps are calculated. Panels c and d have the same scale.

Our simulations allow us to confirm that the underlying physics determining the behavior of densely doped GNRs is similar to the symmetry-dependent mechanism at work in the dilute-doped regime, despite the significant difference in dopant concentrations. This can be seen by examining the wave functions of occupied and empty states for densely doped GNRs (Fig. 3.13). The wave function for State B is seen to be symmetric around a line bisecting a boron dimer and thus exhibits s-like symmetry similar to State 2 of the dilute regime (Fig. 3.11e). This explains why the densely doped GNR couples so strongly to the s-like conduction band of Au(111) at this

energy, thus leading to the broad, unoccupied resonance observed both theoretically (Fig. 3.12a) and experimentally (Fig. 3.10c), which looks so similar to State 2 of the dilute regime. The wave function for State A, however, has p-like symmetry around the boron dimer (Fig. 3.13b) which explains why it couples less strongly to the gold conduction band and exhibits a narrower resonance, similar to State 1 of the dilute regime. Due to the dominant effects of substrate hybridization, States A and B of the dense regime can be heuristically thought of as simple 1D arrays of States 1 and 2 of the dilute regime, respectively. Despite this strong substrate interaction, however, states A and B can still be associated with the lower and upper dopant bands of the freestanding GNR shown in Fig. 3.6f. The experimental energies of these states can thus be used to extract an apparent bandgap of $E_g \approx 1.2$ eV for densely doped GNRs on Au(111).

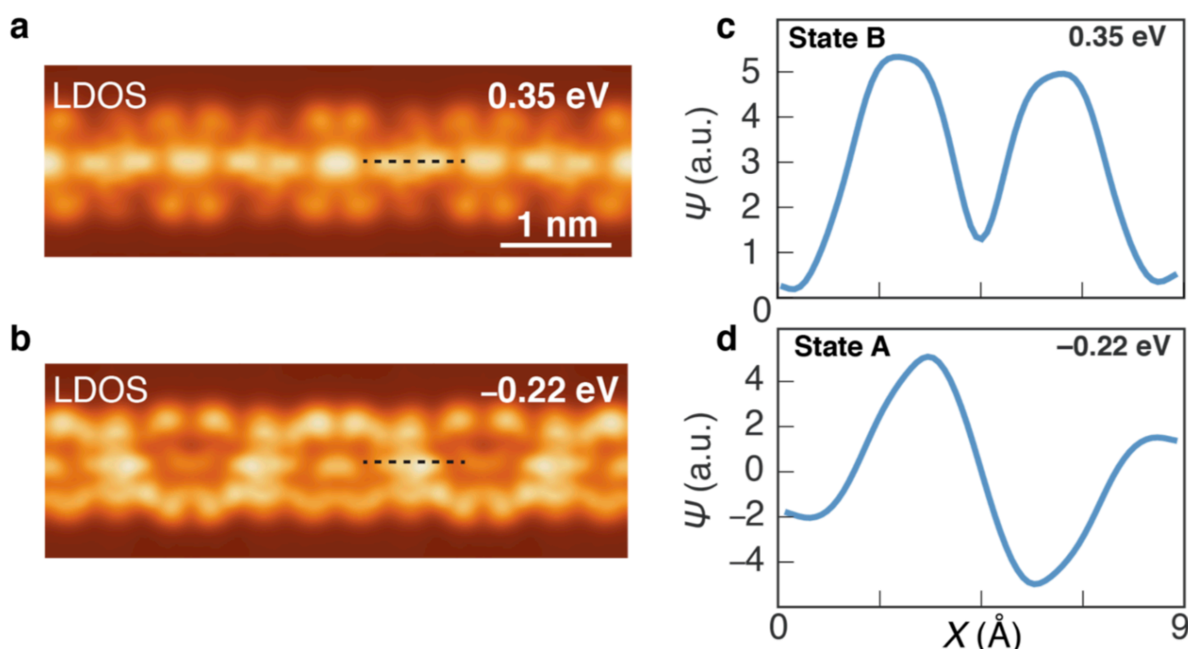

Figure 3.13| Wavefunctions of States A and B of the densely-doped GNR. a, b, Calculated LDOS maps of States A and B for the densely-doped AGNR. c, Calculated wavefunction along the dashed line in a, at E = 0.35eV shows the *s*-like symmetry nature of State B. d, Calculated wavefunction along the dashed line in b, at E = – 0.22eV exhibits a node (i.e., the wavefunction crosses the x-axis) which indicates the *p*- like symmetry of State A. a, and b, have the same scale.

Note that for calculations that included a gold substrate, the GNR was positioned on top of a Au(111) surface that included 288 gold atoms in four layers within the supercell. The GNR was placed perpendicular to the Au(110) crystallographic direction to ensure commensuration between the unit cell of gold and the GNR to within less than 1% lattice mismatch. The GNR was slightly strained initially to fit the lattice constant of gold but was then fully relaxed until the forces on every atom were less than 0.02 eV Å−1.

3.2.5 Conclusion

Our experimental and theoretical studies show that introduction of boron dopants into AGNRs induces the formation of two new in-gap dopant states that have different symmetries.

These dopant-induced states continuously evolve as the boron dopant concentration increases. Moreover, we see that hybridization between dopant atoms and the underlying Au(111) substrate has an unusually strong impact on the electronic structure of boron-doped GNRs, much greater than for other doped GNR systems studied to date.[24, 30, 96] Both the dilute and densely doped electronic behavior depends strongly on the impurity state symmetry, with s-like (p-like) states hybridizing more strongly (weakly) with the gold substrate, thus leading to strong, symmetry-dependent energy splitting. This strong substrate coupling masks the effects of impurity−impurity interactions that are predicted for freestanding boron doped GNRs. We thus expect very different electronic behavior (including a clearer, more well-defined bandgap) for boron doped GNRs placed on substrates that interact less strongly with boron impurity atoms than gold.

Bottom-Up Synthesis of N = 13 Sulfur-Doped Graphene Nanoribbons

3.3.1 Abstract

As explained in sections 3.1 and 3.2, recent advances in bottom-up GNR synthesis have yielded new techniques for modulating GNR width[11, 30, 102] and for introducing dopant heteroatoms[23, 30, 96, 109] with atomic precision both along the GNR edge and, more recently, along the backbone.[22, 27, 28] Edge-doping in bottom-up fabricated GNRs however, has relied mainly on the introduction of nitrogen heteroatoms in the form of pyridine and pyrimidine rings along the edges of chevron GNRs.[30, 96, 110] In this position the electron lone pair on the trigonal planar nitrogen atoms is not in conjugation with the GNR aromatic π- system. Rather than significantly affecting the GNR DOS or energy gap, the electronegative N atoms only induce a rigid shift of the energies of both the valence and conduction bands.[30]

Here we report the fabrication and nanoscale characterization of atomically precise N = 13 armchair graphene nanoribbons (S-13-AGNRs) where alternating $(CH)_2$ groups lining the edges of the GNRs have been replaced by sulfur atoms. This alternative edge-doping pattern places one of the lone pairs (having p-character) on trigonal planar S atoms in full conjugation with the extended π-system of the 13-AGNR. Molecular precursors for S-13-AGNRs (1 in Fig. 3.14a) are derived from 10,10′-dibromo-9,9′-bisanthracene and feature (2- phenyl)thiophene substituents. A submonolayer of 1 was deposited onto a Au(111) surface under ultrahigh vacuum (UHV). Subsequent heating of the decorated Au(111) surface to 200 °C induces a radical step growth polymerization to give poly-1. A second annealing step (400 °C) induces a thermal cyclodehydrogenation to yield fully conjugated S-13-AGNRs. Both STM and STS were used to investigate the structure and to probe the electronic states of the resulting S- 13-AGNRs. STS measurements reveal a LUMO state (lowest unoccupied molecular orbital) for S-13-AGNRs at approximately the same energy as that previously recorded for undoped 13-AGNRs. When compared to undoped 13-AGNRs, the DOS associated with the LUMO in S-13- AGNR spans a significantly broader energy range. These results are consistent with ab initio simulations of S-13-AGNRs that indicate a sulfur-induced increase in the energy separation between CB and CB+1 as well as between the VB and VB−1 13-AGNR band edges (here, CB refers to the conduction band, and VB refers to the valence band).

3.3.2 Bottom-up Synthesis and STM Characterization of Electronic States

The molecular precursor for S-13-AGNRs 1 (Figure 3.141a) was synthesized through a Suzuki cross-coupling of 2,2′,10,10′-tetrabromo-9,9′-bianthracene (2) with 2 equiv of (2-(thiophen-2-yl)phenyl)boronic acid (3) (see the Supporting Information of ref[23]). Oxidative addition favors the sterically less hindered 2,2′-position in the bisanthracene backbone and yields the desired regioisomer 1 as the major product in 44% yield.

A polished Au(111) single crystal was used as the substrate for the STM measurements. Standard Ar^+ sputtering/annealing cycles were applied to prepare an atomically clean Au(111) surface. The molecular building block 1 was evaporated from a home-built Knudsen cell evaporator, and the deposition rate was calibrated in a test chamber using a quartz crystal

microbalance. Compound 1 was sublimed at 478 K onto a 298 K Au(111) substrate under UHV for about 2 min to obtain 30−90% coverage. STM measurements were performed on two home-built low- temperature STMs operating at 13 and 7 K. Both tungsten and PtIr tips were used for STM topographic measurements in constant current mode. The dI/dV spectra were recorded using a tungsten tip and measured with a lock-in amplifier under open-feedback conditions. WSxM was used to process all STM images.

Fig. 3.14b shows a STM image of 1 on Au(111) as deposited. The molecules tend to aggregate into irregular islands along the Au(111) herringbone reconstruction with an average height of 0.5 nm. Annealing the molecule-decorated sample at 200 °C for 20 min induces homolytic cleavage of the labile C−Br bonds in 1 followed by radical step growth polymerization of the intermediate diradical to give poly-1 (Fig.3.14a). A representative STM image of a linear chain of poly-1 on Au(111) is depicted in Fig. 3.14c. Analogous to the polymer precursor for undoped 13-AGNRs, poly-1 exhibits a pattern of alternating protrusions associated with the preferred con- formation of the (2-phenyl)thiophene substituents on the Au(111) surface (the periodicity of the protrusions is 0.83 ± 0.02 nm with an apparent height of 0.43 ± 0.02 nm).[11, 16, 27]Further annealing of Au(111) samples at 400 °C for 20 min induces a thermal cyclodehydrogenation that converts poly-1 into fully cyclized S-13-AGNRs (Fig. 3.14d). The average height and width of the resulting S-13-AGNRs are 0.23 ± 0.01 and 1.9 ± 0.2 nm, respectively, and are comparable with the dimensions previously reported for undoped 13-AGNRs (0.21 ± 0.01 and 1.9 ± 0.2 nm).[11, 21]

Statistical analysis of STM images shows that the average length of S-13-AGNRs obtained by this growth procedure is 5 nm (Supporting Information of ref [23]). We observe some irregular edge structure in our samples following the final cyclodehydrogenation step (see Fig. S8 in Supporting Information of ref [23]). These defects might arise from the additional strain induced along the edges of GNRs by the introduction of five-membered thiophene rings or by deletion of the thiophene ring through fragmentation of the (2- phenyl)thiophene C−C bond during the thermal annealing at 400 °C.

The local electronic structure of S-13-AGNRs was characterized by recording dI/dV spectra at various positions above the S-13-AGNR decorated surface. Fig. 3.15 shows typical dI/dV spectra measured at the center and edges of a S- 13-AGNR compared to a reference spectrum measured with the STM tip placed above the bare Au(111) substrate. The Au(111) reference spectrum is dominated by a peak centered at a sample bias of $V = -0.3$ V that drops steeply for $V \leq -0.5$ V. This feature is known to originate from the Au(111) surface state,[111] which has a band edge at 0.5 eV below the Fermi energy E_F (E_F corresponds to $V = 0$). All spectra recorded with the STM tip positioned above S-13-AGNRs show a peak for $V < 0$ that is similar to the peak observed when the tip is held above bare Au(111). This makes it difficult to discern whether this feature (when seen at locations above a S-13-AGNR) is due to the intrinsic S-13-AGNR electronic structure (such as the VB edge) or is due to the underlying Au(111) surface state. A more unambiguous S-13-AGNR spectral feature is observed at $V = 1.22 \pm 0.23$ V. Here, a peak can be seen in the dI/dV spectra at the S-13-AGNR edges that is not observed at either the S-13-AGNR center or in the Au(111) reference spectrum. This behavior is consistent with the spectral signature of GNR band edge states observed previously for N = 5, 7, and 13 AGNRs[11, 21, 26, 102] and is assigned to the S-13-AGNR conduction band edge. This band edge feature lies at almost the same energy as the undoped 13-AGNR conduction band edge (V = 1.21

± 0.06 V)[11] but is significantly broadened with a full width at half-maximum (fwhm) of ΔE = 0.37 ± 0.2 eV compared to ΔE = 0.19 ± 0.07 eV for the undoped 13-AGNR.

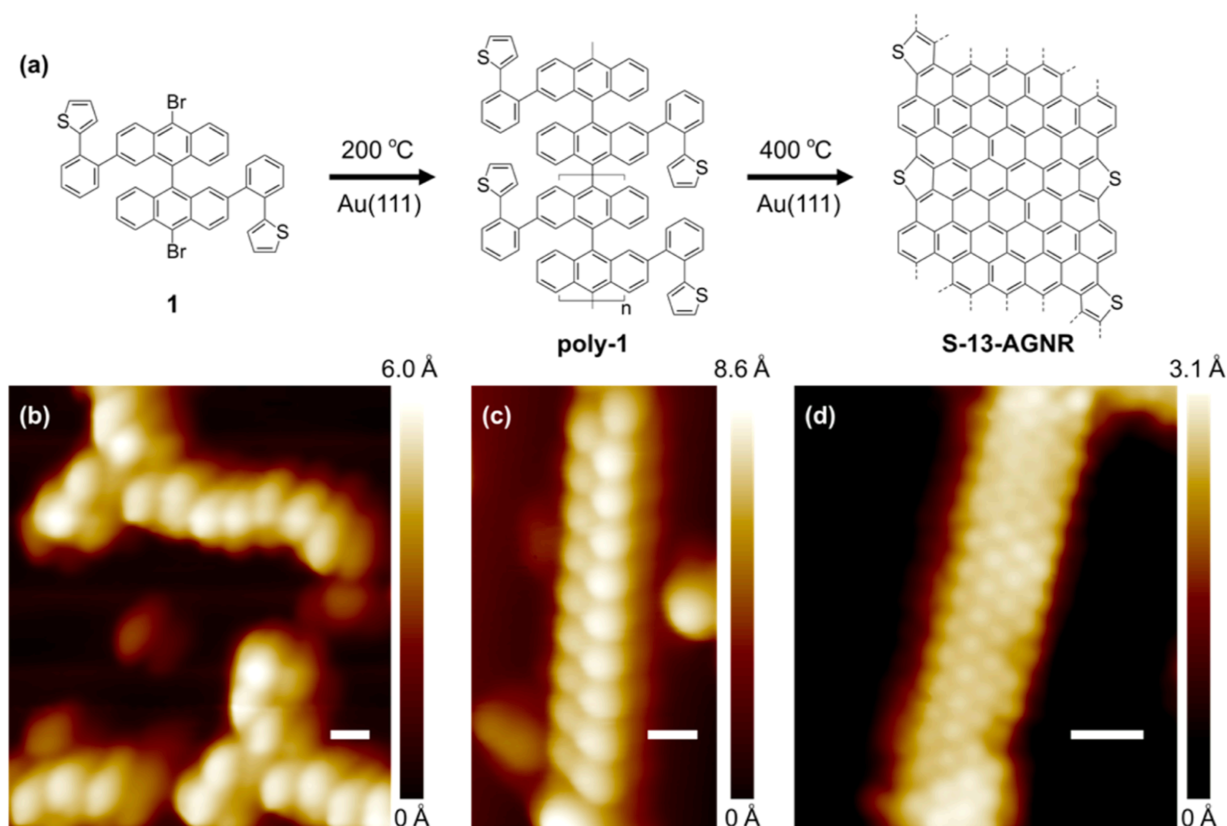

Figure 3.14| Bottom-up synthesis S-13-AGNRs. (a) Reaction scheme for bottom-up synthesis of S-13-AGNRs. Annealing at 200 °C induces radical step growth polymerization. Annealing at 400 °C induces cyclodehydrogenation to yield S-13-AGNRs. (b) STM image of precursor 1 as deposited onto a Au(111) surface (V_s = 2.0 V, I_t = 20 pA, T = 13 K). (c) STM image of poly-1 (after the first annealing step) shows the characteristic pattern of alternating protrusions (V_s = 2.0 V, I_t = 20 pA, T = 13 K). (d) STM image of a fully cyclized S-13-AGNR (V_s = 0.1V, I_t = 15 pA, T = 7 K). Scale bars are 1nm.

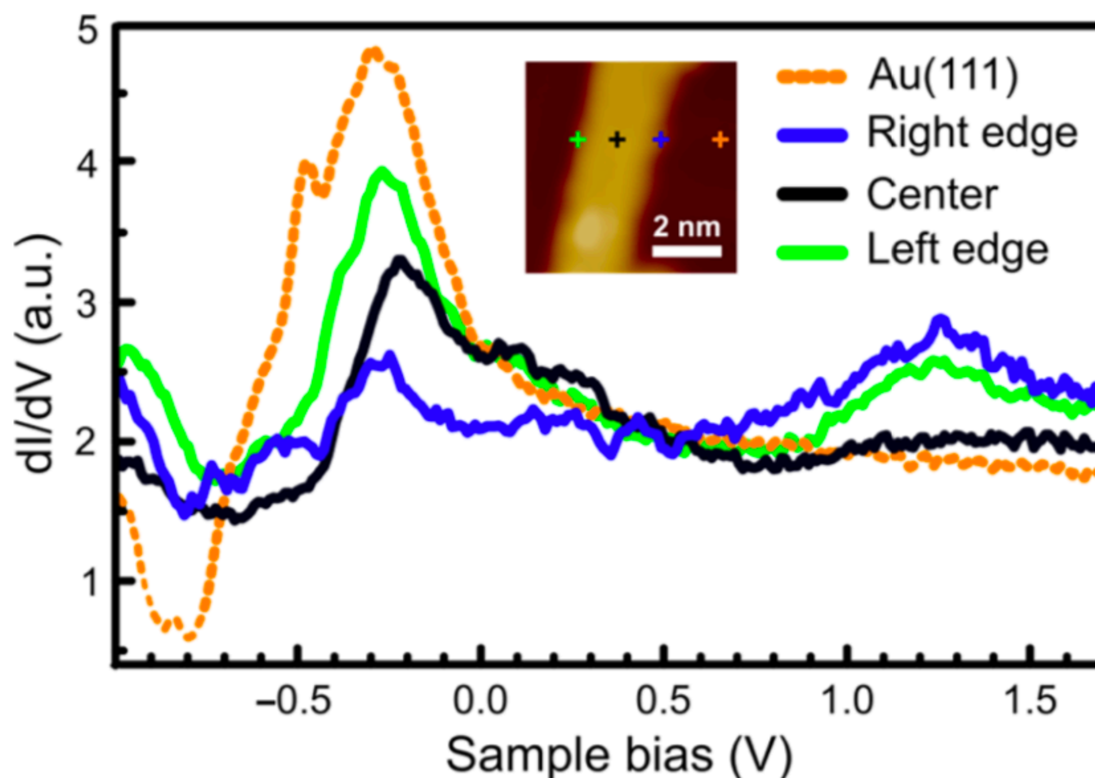

Figure 3.15| STM dI/dV spectroscopy of S-13-AGNRs. Measured dI/dV spectra of S-13-AGNRs at different spatial positions compared to the reference spectrum obtained on bare Au(111). Crosses in the topographic STM image (inset) indicate the positions of recorded spectra (T = 13 K).

3.3.3 Theoretical Calculations and Comparison to Experimental Results

In order to better understand how the electronic properties of 13-AGNRs are affected by substitutional sulfur edge-doping, we performed DFT calculations using LDA for both S-doped (Fig. 3.16a) and undoped (Fig. 3.16b) free-standing 13-AGNRs (all calculations were performed by T. Cao and S. G. Louie). Our calculations suggest that incorporation of sulfur atoms into the armchair edges only slightly reduces the band gap (at the DFT-LDA level) of a pristine 13-AGNR, from 0.90 to 0.76 eV. In addition, when referenced to the vacuum potential, the CB minimum and VB maximum of S-13-AGNRs have similar energy alignment compared to pristine 13-AGNRs. This behavior is quite different from the previously studied case of nitrogen edge-doped chevron GNRs, whose band edges undergo a nearly rigid shift of ~−0.5 eV compared to undoped chevron GNRs.[30] This difference in behavior for N-doped and S-doped GNRs can be explained by the small difference in electronegativity between sulfur and carbon as compared to the large difference between nitrogen and carbon.[112] Furthermore, the sulfur edge-doping causes a significant increase in the energy difference between the CB and CB+1 band edges, as well as between the VB and VB−1 band edges, when compared with pristine 13-AGNRs (Fig. 3.16). This modification to the electronic structure is due to the strong hybridization of S- dopant orbitals with the aromatic network in S-13-AGNRs (Fig. 3.16c) (due

to conjugation of the S lone pair with the π- system).

The calculated band structure of S-13-AGNRs is consistent with the experimentally observed dI/dV spectra of Fig. 3.16d. The experimental CB edge of S-13-AGNRs is very closely aligned with the CB edge observed for undoped 13-AGNRs (similar to the simulated DOS depicted in Fig. 3.16c). The significant broadening of the experimental CB feature for S-13-AGNRs compared to that for undoped 13-AGNRs is consistent with the predicted increase in energy separation between the CB and CB+1 band edges for S-13-AGNRs as compared to that for undoped 13-AGNRs (Fig. 3.16). The reason that the experimental measurement shows only a single feature instead of two peaks is likely due to broadening arising from interaction between S-13-AGNRs and the gold substrate.[111]

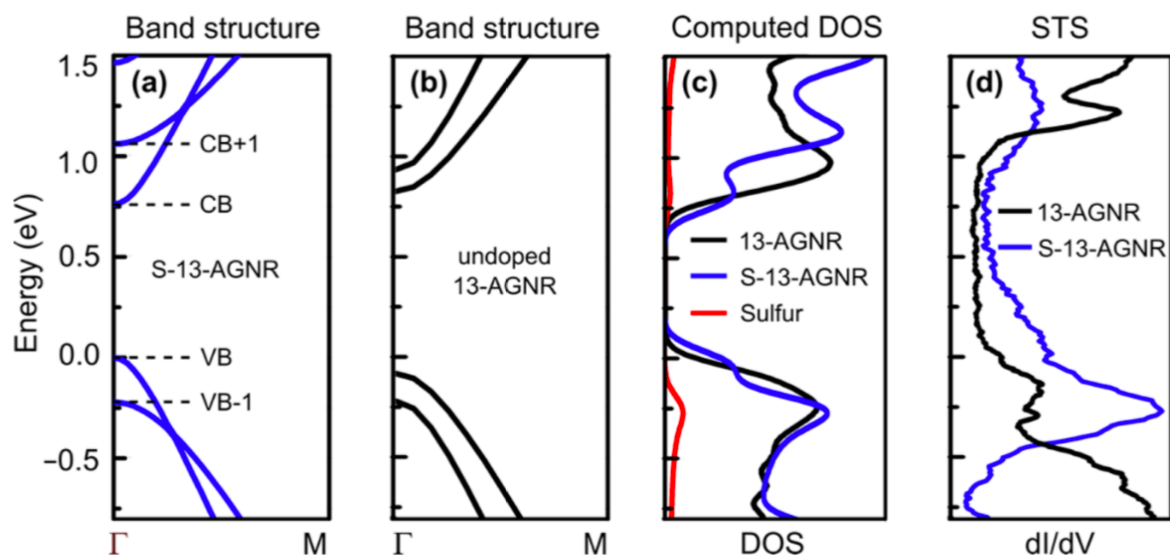

Figure 3.16| Theoretical electronic structure of S-13-AGNRs. Computed band structures of (a) a S-13-AGNR and (b) a pristine 13-AGNR. (c) Calculated DOS of a S-13-AGNR (blue), the partial density of states (PDOS) of sulfur orbitals (red), and the DOS of a pristine 13-AGNR (black) (Gaussian broadened by 0.1 eV). (d) Experimental dI/dV spectrum for a S-13-AGNR (blue) compared to the dI/dV spectrum for a pristine 13-AGNR (black).

3.3.3.1 Computational Methods

First-principles calculations of sulfur-doped GNRs were performed using DFT in the local density approximation implemented in the Quantum Espresso package.[107] A supercell arrangement was used, with the cell dimension carefully tested to avoid interactions between the nanoribbon and its periodic image. We used norm-conserving pseudopotentials,[113] with a plane wave energy cutoff of 60 Ry. The structure was fully relaxed until the force on each atom was smaller than 0.02 eV $Å^{-1}$. All of the σ dangling bonds of carbon atoms on the edge of the nanoribbon were capped by hydrogen atoms. The unit cell dimension along the periodic direction was fully relaxed. The cell sizes along the nanoribbon plane normal direction and edge normal direction were set to 13 and 30 Å, respectively, in order to avoid interactions between the S-13-AGNR and its periodic images. The Gaussian broadening used in plotting the DOS was 0.1 eV.

3.3.4 Conclusion

In conclusion, we have demonstrated the successful bottom-up synthesis of substitutional sulfur edge-doped 13-AGNRs on Au(111), as well as determination of the effect of sulfur edge-doping on the electronic structure of N = 13 AGNRs. Both the theoretically determined and experimentally measured S-13- AGNR electronic structures are consistent with the hybridization of sulfur orbitals with the conjugated π-system of the extended carbon network. This characteristic leads to enhanced energy separation of the CB (VB) and CB+1 (VB−1) band edges, but because sulfur and carbon electronegativities are similar, the energy alignments of N = 13 AGNR bands remain relatively unchanged by sulfur doping.

Chapter 4. Quantum spin Hall Insulator Projects

Here I will describe my work involving the exploration of topological quantum spin Hall (QSH) insulators. QSH insulators host gapped bulk band structures as well as helical edge states that are protected from backscattering via time-reversal symmetry. Transition metal dichalcogenides (TMDs) were predicted to be the perfect platform for realizing freestanding 2D QSH insulators.[46, 66, 114] In this section we report the successful growth and characterization of topological insulators in two different TMD materials: 1T'–WTe_2 and 1T'–WSe_2.[74, 75] Topologically protected helical edge states are observed at 1T'–vacuum and 1T'–1H interfaces (in the case of mixed-phase WSe_2), which are both interfaces between materials having different topological classification. We have successfully created and manipulated different structural phase boundaries by means of STM tip pulses in the single-layer quantum spin Hall insulator 1T'–WSe_2. We observed the formation of one-dimensional interfaces between non-trivial 1T' domains having different rotational orientations as well as induced interfaces between topologically non-trivial 1T' and topologically trivial 1H phases. These two different interface systems were characterized using a combination of STM, STS, and first-principles calculations.[76]

4.1 Quantum Spin Hall State in Monolayer 1T'–WTe_2

4.1.1 Introduction

In this section, we describe the a successful growth of monolayer 1T'–WTe_2 using molecular beam epitaxy (MBE) on a bilayer graphene (BLG) substrate. In-situ ARPES measurements show band inversion as well as the opening of a 55meV bulk bandgap, which is an order of magnitude larger than gaps seen in quantum well QSH insulators using 3D semiconductors.[55, 56] STS spectra show evidence of the insulating bulk and conductive edge nature of 1T'–WTe_2. Our results provide compelling experimental evidence for the existance of a QSH insulator phase in monolayer 1T'–WTe_2.

4.1.2 Topological Phase of 1T'–WTe_2.

Figure 4.1a presents the crystal structure of monolayer 1T'–WTe_2. MX_2 material typically have three different phases, namely 1H, 1T and 1T'. 1T–WTe_2 is composed of three hexagonally packed atomic layers in an ABC stacking. The metal atoms are in octahedral coordination with the chalcogenide atoms. This is not a stable phase in free-standing form and undergoes a spontaneous lattice distortion into the 1T' phase via a doubling of the periodicity in the X direction. W atoms are dislocated from the original octahedral positions to form zigzag chains in the Y direction. The lattice distortion from the 1T phase to the 1T' phase induces band inversion and causes 1T'–WTe_2 to become topologically nontrivial[65, 66, 115].

Figure 4.1b schematically summarizes this topological phase transition in 1T'–WTe_2. Without spin-orbit coupling (SOC), the inverted bands cross at a momentum point along the Γ-Y direction, forming a Dirac cone. Strong SOC lifts the degeneracy at the Dirac point, opening a bulk bandgap. Following the bulk boundary correspondence [45, 116], a helical edge state is guaranteed by the gapped topologically non-trivial bulk band structure.

Our first-principles band structure calculations for 1T– and 1T'–WTe_2 are presented in Fig. 4.1c-e, and are generally consistent with the literature.[48, 65, 66, 117] The key bands for the band inversion are marked to track their evolution (including parity). In 1T–WTe_2, the bands from $5d_{xz}$ and $5d_{z}^2$ orbitals of W are separated by E_F (Fig. 4.1c). Symmetry breaking through the lattice distortion from 1T to 1T' causes these orbitals to hybridize substantially. Figure 1d shows that the d_z^2 orbital is lowered below E_F whereas the d_{xz} orbital lifts in the opposite direction near the Γ point. Because these two inverted bands have different parity at the Γ point, the Z_2 invariant v (where by $(-1)^v$ is determined by the product of all occupied band parity eigenvalues[48]), changes from 0 (trivial) to 1 (non-trivial). The valence band maximum in the 1T' phase is mainly from the W d_{yz} orbital, with an even parity at the Γ point. When its degeneracy with the d_{xz} orbital in the 1T phase is lifted by the lattice distortion, the band stays below E_F and does not involve any band inversion. With the inclusion of SOC (Fig. 4.1e), the bands further hybridize

with each other and the degeneracies at the Dirac cones formed by the band inversion are lifted, opening a bandgap in the bulk states. We note here that different calculation methods give different estimates of the size of the bandgap for strain-free 1T'–WTe_2 monolayers. The generalized gradient approximation (Perdew-Burke-Ernzerhof, PBE) usually underestimates the bandgap and gives a negative bandgap value[65], while PBE with hybrid function (HSE06) gives a positive value[117].

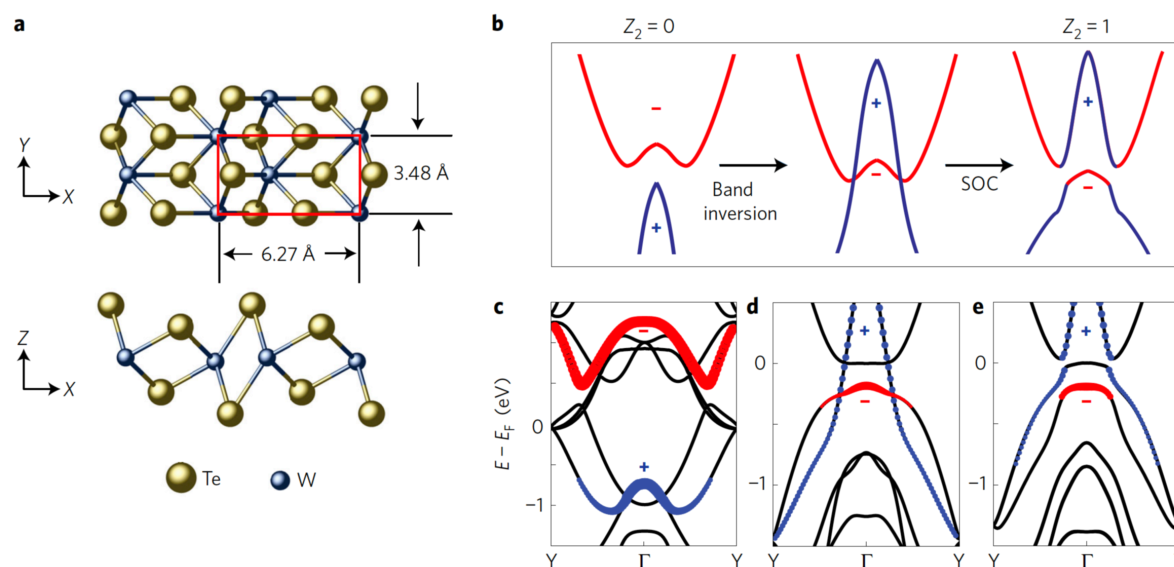

Figure 4.1 | Topological phase transition in 1T'–WTe_2. a, Crystal structure of 1T'–WTe_2. The doubled period due to the spontaneous lattice distortion from 1T phase is indicated by the red rectangle. b, Schematic diagram to show the bulk band evolution from a topologically trivial phase, to a non-trivial phase, and then to a bulk band opening due to SOC. c–e, Calculated band structures for WTe_2 to show the evolution from 1T–WTe_2 along the Γ–Y direction (c), 1T'–WTe_2 without SOC (d) and 1T'–WTe_2 with SOC (e). Red and blue dotted bands highlight the two bands involved in band inversion, which mainly contain the $5d_{z^2}$ and $5d_{xz}$ orbital contents, respectively. + and − signs denote the parity of the Bloch states at the Γ point.

4.1.3 Growth and Surface Characterization

Figure 4.2 summarizes the MBE growth and the characterization of 1T'–WTe_2 on BLG/SiC (0001). The monolayer 1T′–WTe_2 films were grown by MBE on bilayer graphene (BLG) epitaxially grown on 6H-SiC32. Growth was performed at Beamline 10.0.1, Advanced Light Source, Lawrence Berkeley National Laboratory (all the growth and ARPES characterizations were carried out by S. Tang, C. Zhang, C. Jia, H. Ryu, H. Yan, R. G. Moore, Z. Hussain, S.-K. Mo, and Z. X. Shen). The base pressure of the MBE chamber was ~4 × 10−10 torr. Ultrahigh-purity tellurium (99.999%) and tungsten (99.999%) was evaporated from an effusion cell and an electron beam evaporator, respectively. The flux ratio between tungsten and tellurium is set between 1:10 ~ 1:20. We found that the quality of the sample does not depend much on the ratio. However, it depends critically on the substrate temperature. The substrate

temperature was held at 280 °C during growth. The growth process was monitored by RHEED. The growth rate was ~40 min per monolayer. After growth we annealed the sample at 300 °C for 2 h to improve the film quality.[109] The reflection high-energy electron diffraction (RHEED) pattern of the BLG substrate and the monolayer 1T'–WTe_2 are presented in Fig. 4.2a. Clean vertical line profiles after the deposition of W and Te clearly indicate the layer-by-layer growth mode. Using the lattice constant of BLG (a = 2.46 Å) as a reference, the lattice constant of the grown film is estimated to be ~ 6.3Å ± 0.2 Å, consistentwith the expected value for monolayer 1T'–WTe_2.[117] The angle-integrated core level photoemission spectrum (Fig. 4.2b) exhibits the characteristic peaks of Wand Te for the 1T' phase. Two differently coordinated types of Te contribute two sets of Te 4d peaks, while the clean doublet feature of the W 4f peaks indicates a pure 1T' phase rather than a mixed phase of 1T' and 1H.[118] Figure 4.2c is an atomically resolved STM image of 1T'–WTe_2, from which a ~7.5° angle distortion is observed, which is universal in bulk 1T' phase MX_2.[118, 119] Fig. 4d,e show a typical morphology of the 1T'–WTe_2 on BLG substrate. A typical diameter for a branched island is ~50 nm, with branches having sizes larger than 20nm×20 nm. Since the growth is edge-diffusion limited, the edge geometry is random.

The measured Fermi surface (FS) from the in-situ ARPES is shown in Fig. 4.2e. Due to the symmetry mismatch between the two-fold rotational symmetry of the sample and the three-fold symmetry of the substrate, there exist three energetically equivalent domains rotated by 120 with respect to each other, and each domain contributes two electron pockets along the Γ-Y direction of their respective Brillouin zones.[74] The experimental band dispersion along Γ-Y cutting the FS electron pockets is inevitably superposed with the contributions from Γ-P and Γ-P'. However, as shown in Fig. 4.2f-h, the valence bands from Γ-P' and Γ-P directions are enclosed by the Γ-Y band. Therefore, the existence of multiple domains does not affect the characterization of the gap size and the separation between valence and conduction bands. Overall band structure measured with ARPES (Fig. 4.2f,g) gives a nice agreement with the HSE06 calculation (Fig. 4.2g), demonstrating the 1T' nature and the high quality of our thin-film samples.

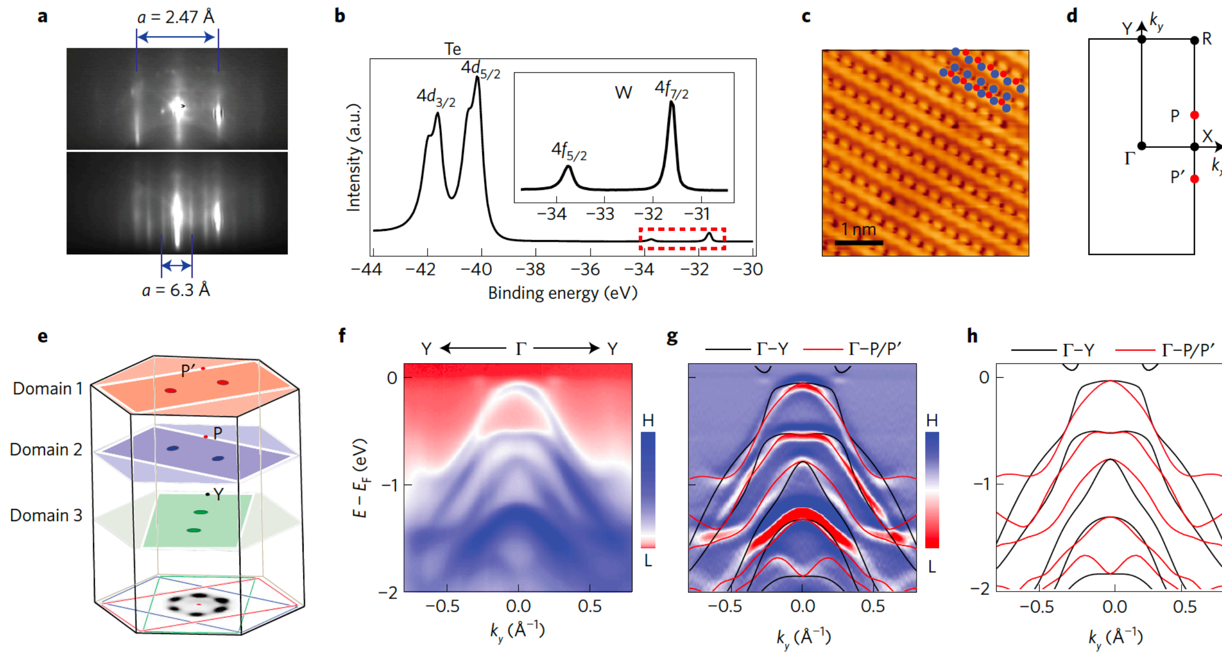

Figure 4.2 | Characterization of epitaxially grown 1T'–WTe_2 and overall electronic structure from ARPES. a, RHEED pattern of graphene substrate (top) and sub-monolayer 1T'–WTe_2 (bottom). b, Core level spectra of 1T'–WTe_2. The inset is a close-up for the region marked by the red dashed rectangle. c, Atomically resolved STM topographic image of 1T'–WTe_2. Blue and red dots represent W and Te atoms, respectively. d, Brillouin zone of 1T'–WTe_2. Time reversal invariant momenta Γ, X, Y, R are labelled by black dots. e, Fermi surface map of 1T'–WTe_2. The intensity is integrated within a ±10 meV window around E_F. There are three domains rotated with respect to each other by 120 due to difference in the symmetry of the sample and the substrate. The measured data along the Γ–Y high-symmetry direction is unavoidably mixed with the signals from the Γ–P and P' directions. The schematic contributions from different domains are represented by different colour panes above the real Fermi surface map at the bottom. f, Overall band structure measured along the experimental Γ–Y direction. g, Second derivative spectra to enhance low-intensity features. The overlaid black lines are the calculated band structure along the Γ–Y direction. h, Calculated band structure along the Γ–Y (black) and Γ–P/P' (red) directions, respectively. The low-energy electronic structure around the Γ point is dominated by the contributions from the Γ–Y bands.

4.1.4 Polarization Dependent ARPES

A powerful and direct way to discern the orbital characters of particular bands is the polarization dependent ARPES measurements. The matrix element of a photoemission process can be written as $\left|M_{f,i}^{k}\right|^{2} \propto \left|\langle\phi_f^k|\hat{\varepsilon}.\boldsymbol{r}|\phi_i^k\rangle\right|^{2}$, where $\hat{\varepsilon}$ is the unit vector of the electric field of the light, ϕ_f^k and ϕ_i^k are the initial and final state wave functions of the photoelectron, and $\boldsymbol{r}$ is the position of electrons. By changing $\hat{\varepsilon}$ with respect to other geometric factors, one may enhance or

suppress the ARPES signal from the orbitals of particular symmetry. Within our experimental configuration sketched in Fig. 4.3a, both the analyzer slit and incident light are in the mirror plane defined by the analyzer slit and the sample surface normal. In such a setup, P and S polarized photons make $\hat{\varepsilon}.\boldsymbol{r}$ even and odd, respectively. With the final state of photoelectron approximated as an even parity plane-wave state $e^{i\boldsymbol{k}.\boldsymbol{r}}$with respect to the mirror plane, the photoemission signal from an initial state with even (odd) parity with respect to mirror plan are always enhanced (depressed) under P polarized photon excitation. The reverse is true for S polarized incident light. The measured polarization dependence can be directly compared to the orbital characters from the band calculation (Fig. 4.3b).[66] Figures. 4.3c and d are ARPES data along the ΓY direction with P and S polarized incident light. To see the low energy electronic structure including the conduction band more clearly, we performed potassium (K) surface doping on the sample, which is known to inject electrons to a sample and raise chemical potential. Figs. 4.3e and f only focus on the low energy band structure along ΓY from the surface K-doped samples with P and S polarizations, respectively. To guide the eye, we marked three segments on different bands by red dots in Fig. 4.3c and e. It is clear that the red dotted segments show high intensity only with P polarization but can hardly be seen with S polarization. By rotating the azimuthal angle of the sample, one can change the orbital reflected on the mirror plane and get more information on the orbital characters of the bands. We focus on the predicted inverted band, the second valence band from the Fermi energy. Different ARPES data are taken with the different azimuthal angle, 0, 29 and 90 degrees in Fig. 4.3. The intensity of second valence band is always suppressed at S-polarization and enhanced at P-polarization. This indicates the symmetry of this band is always even with respect to the mirror plane we chose. We thus conclude that the only orbital satisfying this criterion is the d_z^2 orbital, which agrees well with the calculation (red dotted band in Fig. 4.3b). At the same time, intensity from the orbitals with in-plane character is clearly enhanced for S polarization as can be seen in Figs. S1d and f. Our polarization dependent ARPES gives strong evidences that band inversion occurs in our 1T'–WTe_2 monolayer films. Hence, the predicted band inversion in 1T'–WTe_2 is well established experimentally by a polarization-dependent ARPES measurement, from which one can clearly distinguish in- and out-of-plane orbital characters and their inversion around the Γ point (see Figs. S1 and 2 of supplementary information of ref [75])*. This indicates the non-trivial topology of 1T'–WTe_2.

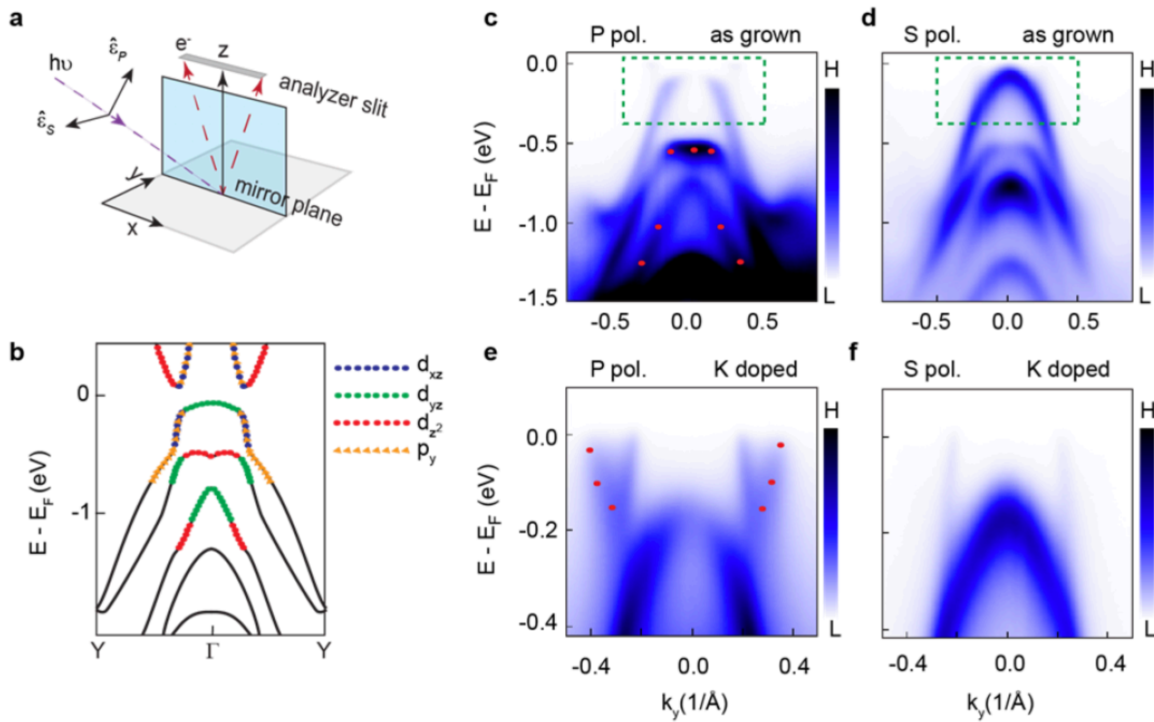

Fig. 4.3| Polarization dependent ARPES. a, Experiment setup for polarization dependent ARPES measurement. b, Calculated contribution (reproduced from (20)) from different orbitals for the valence and conduction bands of 1T'–WTe_2. c-d, ARPES data along ΓY direction taken with P-polarized and S-polarized light, respectively. e-f, Polarization dependent ARPES data along ΓY direction measured on a surface K-doped samples to clearly observe the conduction band only within the enlarged area of the blue boxes in c and d. The red dots in c and e are added as a guide to the eye to mark orbitals with out-of-plane character. The K adatoms not only transfer charge to the film underneath, but also create extra scattering and thus broaden the FWHM of peaks. Broadened valence band and conduction band contribute a relatively high residual spectral weight between them. In the case of e, due to the complete suppression of the half of the conduction band from the orbital selection through a polarization dependent matrix element, residual spectral weight between the conduction band and valence band makes a false impression that they were connected.

4.1.5 Electronic Structure Characterization of Bulk and Edge

The signature of strong SOC in 1T'–WTe_2 is the lifting of state degeneracy at the Dirac cones along the Γ-Y direction, resulting in an opening of the bulk gap as illustrated in Fig. 4.4a. This can be seen more clearly in the energy distribution curves (EDCs) extracted at the valence band top and the conduction band bottom. Since the ARPES data in Fig. 4.2 show only faint tails of the bulk conduction band, we deposited potassium (K) onto the surface to raise E_F[110] and make the conduction band more clearly visible to ARPES. Figure 3b focuses only on the low-energy electronic structure of surface K-doped 1T'–WTe_2, with E_F raised~70meV to reveal the

conduction band bottom more clearly. The corresponding EDCs in Fig. 4.4c show that the conduction band and the valence band are well separated from each other. To quantify the size of the bandgap, we extracted two EDCs from the momentum positions at the conduction band bottom and valence band top, labelled by the dashed lines in Fig. 4.4b, and overlaid the min Fig. 4.4d. The red and green peaks in Fig. 4.4d correspond to the energy positions of the conduction band bottom and the valence band top, respectively. We estimate the size of the bandgap to be 55 $\pm$ 20meV and 45 $\pm$ 20meV in intrinsic and K-doped samples, respectively (see Fig. S3 of supplementary information of ref [75]). This is in clear contrast to the bulk 1T'–WTe_2, which is a semimetal with a complex band structure near EF exhibiting multiple Fermi pockets[120]. The stacking of energy momentum dispersions with fine momentum steps parallel to the Γ-Y direction (Fig. 4.4e,f) further establish the effect of SOC by showing that the gap never closes for any momentum across the FS.

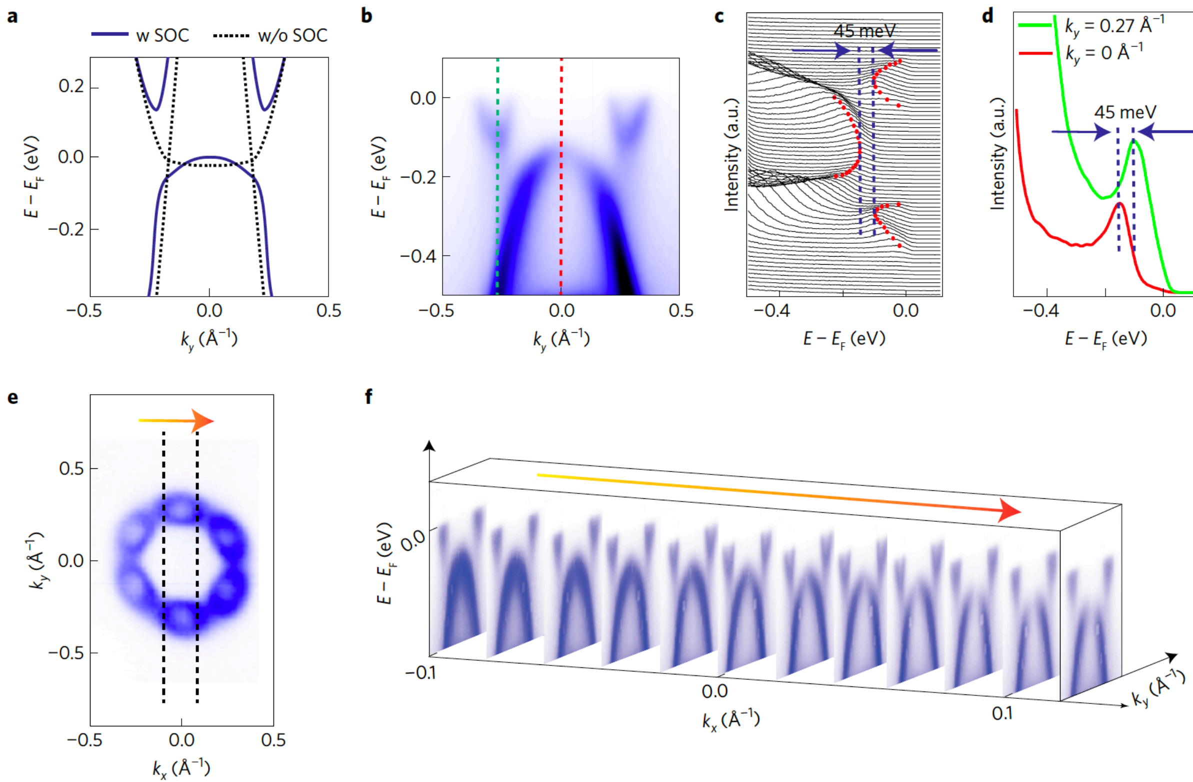

Figure 4.4 | Bandgap opening in monolayer 1T'–WTe_2. a, Calculated band structure along the Γ–Y direction. b, ARPES data along the Γ–Y direction taken from surface K-doped sample. c, EDCs for the data in b. d, EDCs from the momentum positions marked with green and red lines in b. The green line corresponds to the conduction band bottom and the red line corresponds to the valence band top. e, Fermi surface map of K-doped sample. Six electron pockets are due to the three rotational domains as explained for Fig. 4.2e. We focus only on the FS from a single domain. f, Stacking plot of cuts between the parallel dotted lines labelled in e.

Now that we have established band inversion and the opening of a bandgap due to the strong SOC, the remaining signature of a QSH insulator is the conductive edge state in contrast to the insulating bulk, which can be better examined by STS. Figure 4.5a shows the local differential conductance (dI/dV) spectrum taken at a point far away from the WTe_2 edges, which

represents the bulk LDOS. The peak positions in dI/dV are in good agreement with the band edges found in ARPES. The agreement between ARPES and STS further extends to the size of the gap, as the mean gap size determined by STS is 56 ± 14meV (Fig. 4.6).

In contrast to the gap in the bulk, dI/dV at a 1T'–WTe_2 edge is very different, showing a `V-shape' spectrum with states filling in the bulk gap (Fig. 4.5b), which may indicate the existence of a conductive edge state. Indeed, similar dI/dV spectral line shapes have been reported for other topological systems with distinct edge states[64, 121] and have been attributed to the one-dimensional (1D) nature of the edge states and the emergence of a Luttinger liquid or coulomb gap[64]. Figure 4.5c shows dI/dV as a function of energy and distance away from an edge, which demonstrates that the V-shaped conductance is localized at the edge of the WTe_2. We observe that such localized edge states run continuously along our sample edges (Fig. 4.7), with only small variations in the fine details of the spectra, regardless of the size, shape, and edge roughness of samples. This provides evidence of the edge state's topologically non-trivial nature.[121, 122]

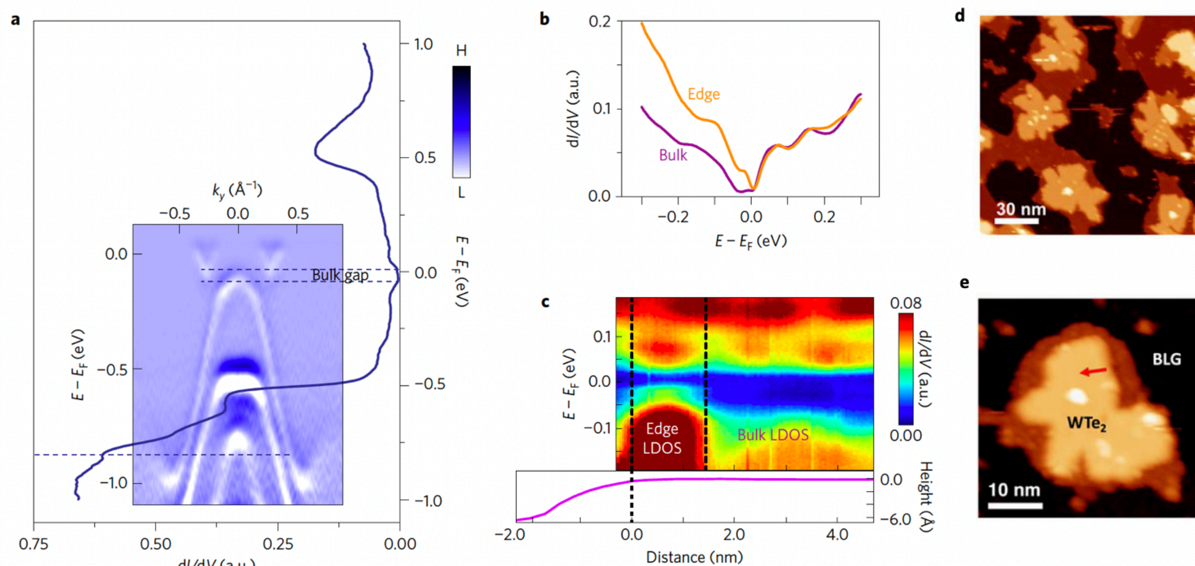

Figure 4.5 | Tunneling spectroscopy in the bulk and at the edge of 1T'–WTe_2. a, STM dI/dV spectrum acquired in the bulk of monolayer 1T'–WTe_2. The inset is the high-symmetry ARPES cut along the Γ-Y direction aligned in energy with the STS spectrum (acquired from a K-doped sample). Since the surface K-doping raises the position of E_F by 70 meV, the whole ARPES spectrum is shifted by that amount for proper comparison with STS. b, Representative dI/dV spectra taken at the edge (orange) and in the bulk (purple), respectively. c, dI/dV spectra taken across the step edge of a 1T'–WTe_2 monolayer island (top), and corresponding height profile (bottom). d, STM topographic image of 1T'–WTe_2 film on BLG. The growth process was halted before reaching to continuous film in a deliberate effort to maximize the number of edges. The black area is bare graphene substrate. The dark brown area is a contamination layer which sits on the bare graphene and tends to be amorphous and somewhat mobile. The light orange area is monolayer WTe_2. There is a SiC step near the top right corner which lightens the relative colors

of 180 the graphene, contamination, and WTe_2 in that region. e, STM topographic image of a single domain. The red arrow is the line along which the spectroscopy in Fig. 4.5c was acquired.

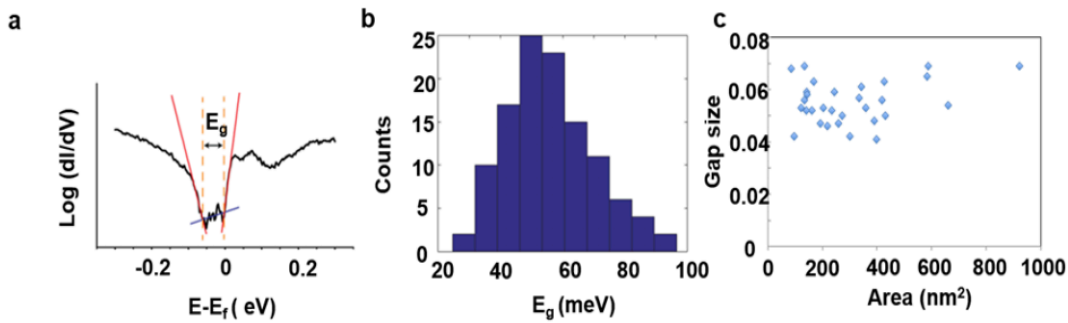

Fig. 4.6| Determining the bulk gap size from STS. a, The bulk gap size is determined 189 by linear fits to the two sides and the bottom of the gap. The gap width E_g is the difference in the energies of the intersection points. b, Histogram of gap sizes. c, Size of the bulk gap as a function of domain size as measured by STS.

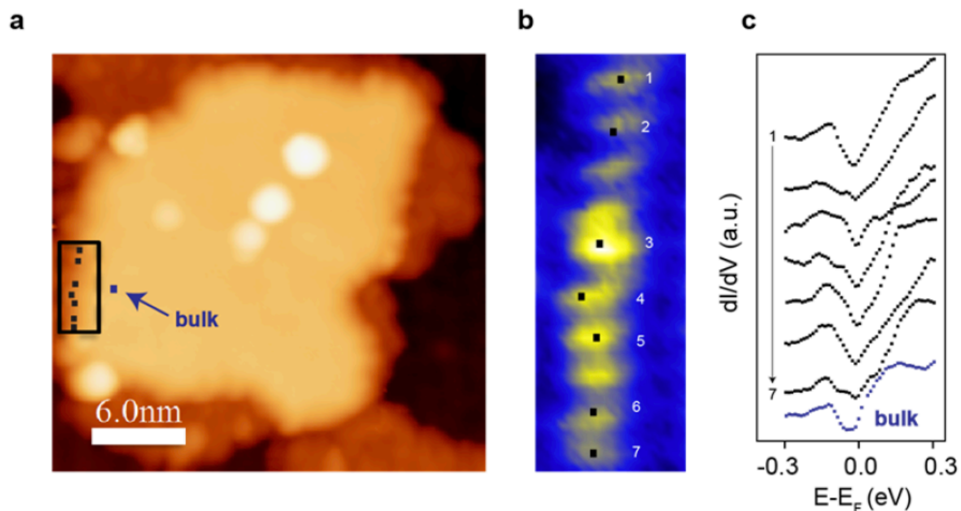

Fig. 4.7| Continuous edge states on irregularly shaped edges. a, STM image of a monolayer 1T'–WTe_2 domain. b, dI/dV map at the edge of WTe_2 domain shown in a within the black rectangular box. c, Corresponding dI/dV curves labeled in b except for the blue curve which is a bulk reference curve obtained at the point marked with a blue dot in a.

4.1.6 Conclusion

By combining ARPES and STS results, we provide strong evidence supporting the direct observation of all the characteristic electronic properties of a QSH state with a large energy gap in 1T'–WTe_2, confirming the theoretical prediction.[65] Such a robust platform for a QSH insulator in 2D TMDs should provide new opportunities for fundamental studies and novel device applications. Since TMDs are inert, widely available, can be exfoliated for transport experiments, and be made into few-layer and van der Waals heterostructure devices, we expect them to be the

material of choice for a much expanded, multimodal effort to understand and utilize QSH systems.

4.2 Observation of Topologically Protected States at Crystalline Phase Boundaries in Single-Layer WSe_2

4.2.1 Introduction

As shown in the previous section, monolayer 1T′–WTe_2 films have been shown to exhibit all of the hallmarks of the QSH effect (e.g., band inversion, helical edge states, and edge state quantum conduction)[75, 123-125]. However, they do pose challenges for quantitative microscopy of topological edge states due to the high degree of structural disorder in the edges of 2D 1T′–WTe_2 islands produced by MBE. Although the existence of topological edge states is protected against disorder, quantitative characterization of their decay lengths, dispersion features, and defect interactions requires crystallographically well-ordered edges since these properties strongly depend on edge orientation,[121, 126, 127] strain, and chemical environment.[128] In order to achieve structurally well-defined boundaries in a fully accessible QSHI, we grew mixed-phase WSe_2 monolayers on SiC (0001) using MBE growth techniques. Single-layer WSe_2 is bimorphic with two stable crystalline phases (1H and 1T′ (Fig. 4.8a)) that are close in energy,[65] thus enabling the growth of mixed topological/ trivial phases with crystallographically defined phase boundary interfaces. The 1H phase (which is the structural ground state of WSe_2) has a much larger electronic bandgap[129, 130] than the 1T′ phase, thus allowing the two phases to be easily distinguished. The onset of the QSHE in mixed-phase WSe_2 thus results in topologically protected states at crystallographically well-defined 1T′–1H phase boundary interfaces.

We have verified the QSHI ground state of 1T′–WSe_2 using ARPES, STM/STS, and first-principles calculations. ARPES reveals the existence of inverted bands at the E_F and the presence of a bulk bandgap. STS measurements confirm the bulk bandgap seen by ARPES and further demonstrate the existence of topological interface states within this bandgap that are spatially localized at 1T′–WSe_2 boundaries. These boundary states are easily observable at crystallographically well-ordered 1T′–1H interfaces, but can also be seen at the irregular 1T′ edges. The structural perfection of the 1T′–1H boundary allows us to measure an interface state decay length of 2 nm into bulk 1T′–WSe_2, agreeing with the results of ab initio numerical simulations

4.2.2 Structural Characterization of Single-Layer 1T′–WSe_2.

Our experiments were carried out on high-quality single layers of WSe_2 grown on epitaxial bilayer graphene (BLG) on 6H-SiC(0001) by MBE. In order to obtain the metastable 1T′–WSe_2 phase, the temperature of the BLG/SiC(0001) substrate was held at 500 K during growth, a significantly lower temperature than required to grow the more stable 1H phase (675 K). Under these growth conditions the RHEED pattern of single-layer WSe_2 (Fig. 4.8b) shows

the formation of an additional large lattice periodicity (5.8 Å) consistent with the 1T′ phase that coexists with the shorter 1H phase periodicity (3.3 Å). XPS measurements of the WSe_2 layers (Fig. 4.8c) reveal the emergence of two new pairs of peaks ($d^{T'}$ and $f^{T'}$) near the characteristic Se (d^{H}) and W (f^{H}) peaks for the 1H phase[129], suggesting the presence of an additional lattice symmetry for W and Se.[131] STM imaging confirms that our WSe_2 layers are composed of coexisting domains of 1H and 1T′ phase (see Figs. S1 supplementary information of ref [74]). Figure 1d shows an atomically resolved STM image of the 1T′ phase of WSe_2, which is characterized by straight atomic rows of two nonequivalent zigzag atomic chains. The 1T′ phase of Fig. 4.8d exhibits a period enlargement to 5.73 ± 0.09Å along the x direction compared to the 1H phase, in good agreement with the RHEED spectra. Adjacent atomic rows in 1T′–WSe_2 exhibit a slight translational shift along the y-direction due to a shear angle that varies between 2° and 6° depending on the domain, similar to that observed previously for other TMD materials.[118, 132] We identify the atomic rows in the STM images of Fig. 4.8d, e as originating from W-Se zigzag chains (see sketch in Fig. 4.8e), in good agreement with the expected structural distortion of the 1T′ phase.[65] The ball-and-stick model shown in Figs. 4.8a, e corresponds to our calculated relaxed atomic structure of 1T′–WSe_2.

We experimentally characterized the electronic structure of coexisting 1H and 1T′ phases of single-layer WSe_2 via ARPES and STS (where all the growth and ARPES characterizations were carried out by S. Tang, H. Ryu, S.-K. Mo, and Z. X. Shen). Figure 4.9c shows the Fermi surface (FS) intensity map for a 0.8 monolayer (ML) coverage of mixed-phase WSe_2 measured via ARPES. The observed FS structure is entirely due to the 1T′ phase since the valence band (VB) maximum of 1H–WSe_2 has a much higher binding energy at $E = -1.1$ eV.[129] The FS is composed of two small elliptical electron pockets at the Λ points located along ΓY (Fig. 4.9a). The three equivalent rotational domains of the 1T′ phase on BLG leads to the emergence of three pairs of these features rotated by 120° (Fig. 4.9b), thus forming a ring-like FS around the Γ point. Figure 4.9d shows the measured band dispersion along the ΓY direction of the Brillouin zone (BZ). Due to the rotational domains, contributions from both the ΓY and ΓP directions can be resolved. The VB maximum is approximately 170 ± 20 meV below the E_F and exhibits a flattened, nonparabolic onset shape along ΓY. Naturally occurring n-type doping in our samples shifts the conduction band (CB) below E_F, which is why the electron pockets at Λ are visible in the ARPES spectrum. This reveals the existence of an indirect bandgap (E_g) that can be quantified by taking the difference of the energy positions of the CB minimum (at the Λ point) and the VB maximum (at the Γ point) from two energy distribution curves (EDCs) of the ARPES spectrum (taken along the dashed lines in Fig. 4.9d). As shown in Fig. 4.9f, we extract a bandgap value of $E_g = 120 \pm 20$ meV centered at $E = -110$ meV ± 20 meV. The observed band dispersion and gap value is characteristic of band inversions predicted for 1T′–TMD materials.[65]

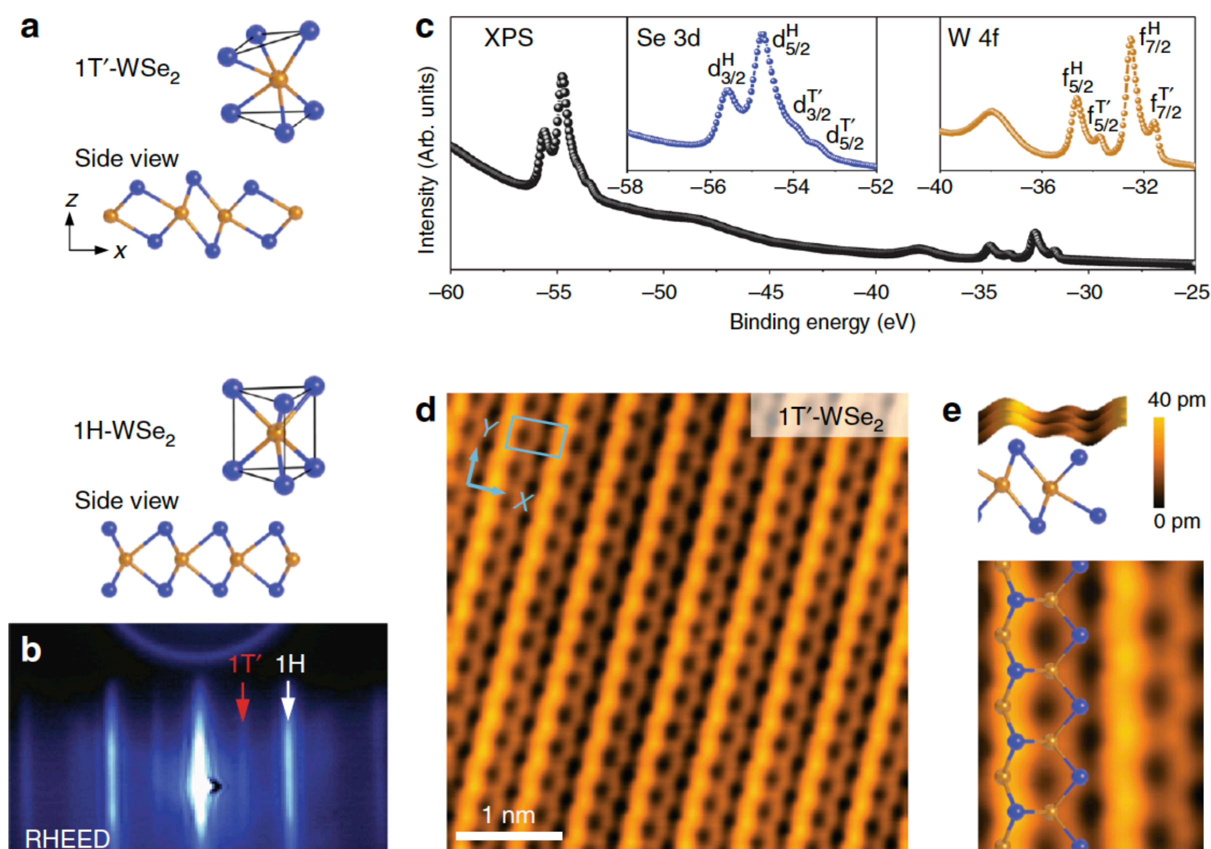

Figure 4.8| Atomic structure of mixed-phase single-layer WSe_2. a, Calculated unit cells and side-view sketches of the 1T′ and 1H phases of single-layer WSe_2. Se (W) atoms are depicted in blue (orange). b, RHEED pattern of single-layer 1T′/1H-mixed-phase WSe_2. Red and white arrows indicate diffraction stripes from 1T′ and 1H phases, respectively. c, Core-level XPS spectrum of single-layer 1T′/1H mixed-phase WSe_2. Insets show zoom-in of the Se (blue) and W (orange) peaks for the 1T′ ($d^{T'}$, $f^{T'}$) and 1H (d^{H}, f^{H}) phases. d Atomically resolved STM image of single-layer 1T′–WSe_2. The unit cell is indicated in blue (V_s = +500 mV, I_t =1 nA). e, Side and top view close-up of the 1T′–WSe_2 STM image with a sketch of calculated 1T′-WSe_2 (only upper-layer Se atoms are depicted in top view).

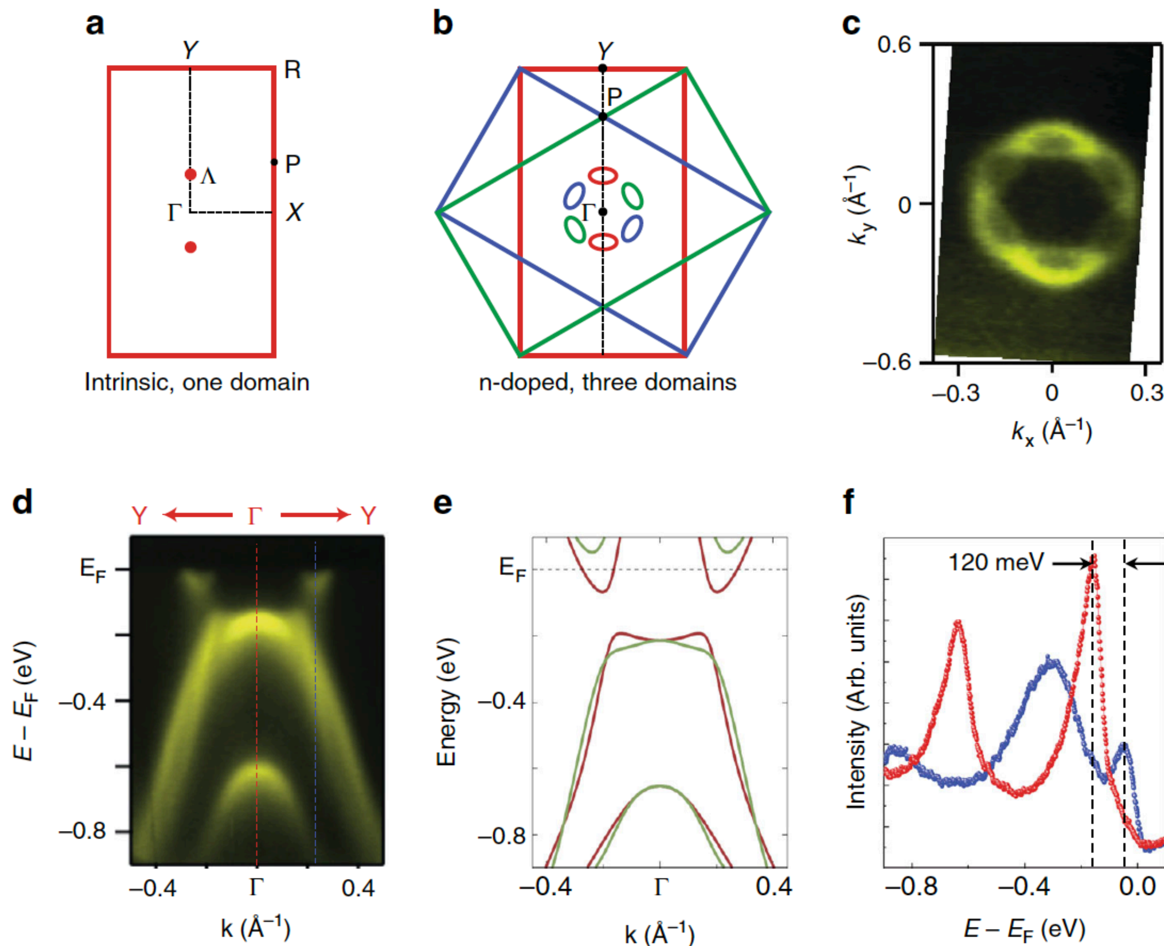

Figure 4.9| ARPES characterization of single-layer 1T′–WSe$_2$. a, Sketch of the first Brillouin zone of 1T′–WSe$_2$. Relevant high-symmetry points are indicated. b, Three surface Brillouin zones corresponding to the three rotational 1T′–WSe$_2$ domains on the BLG surface represented by three different colors. The Fermi surface pockets from each rotational domain are indicated by ellipses of corresponding colors. Black dashed line represents the experimental ARPES line cut shown in d. c, Experimental 1T′–WSe$_2$ Fermi surface measured by ARPES. d, High-resolution ARPES band dispersion along the Y-Γ-Y direction. Due to the presence of rotational domains, contributions from both Γ-Y and Γ-P directions are observed in a single ARPES measurement (T = 60 K and photon energy E = 75 eV). e, Calculated bands for the 1T′ phase of single-layer WSe$_2$ along Γ-Y (brown) and Γ-P (green) directions. A downward rigid shift of 130 meV has been added to account for n-doping seen in the experiment. f, EDCs from the momentum positions marked with dashed blue and red lines in d.

4.2.3 Electronic Characterization of Single-Layer 1T′–WSe_2.

The LDOS of mixed-phase, single-layer WSe_2 was measured via STS point spectroscopy, as seen in Fig. 4.10a. The 1H phase of monolayer WSe_2 shows a bandgap of 1.94 eV, in good agreement with previous measurements19, but the 1T′ phase reveals a finite, asymmetric LDOS that extends across both the occupied state and unoccupied state regions. The most pronounced feature in the unoccupied state region of the 1T ′ phase is a broad, asymmetric peak centered around + 0.24 V. The finite LDOS seen in the occupied state region of the 1T′ phase (-1 V<V_s < 0 V) confirms that the bands observed in ARPES at low binding energy (Fig. 4.9d) belong to the 1T′ phase since this energy range is clearly gapped out for the 1H phase. Also prominent in the electronic structure of the 1T′ phase is a gap-like feature located at $V_s = -130 \pm 5$ mV. Figure 3c shows a close-up of this feature (the boxed region of Fig. 4.10a). The width of this 1T′ gap feature can vary depending on surface position, but it has an average FWHM = 85 mV ± 21 meV (see Supplementary Note 3 for gap statistics of ref[74]). A second dip feature located at EF can be seen in the dI/dV curves taken for 1T′–WSe_2. A similar zero bias feature has also been seen in 1T′–WTe2 and has been attributed to the opening of a Coulomb gap.[133] These characteristic features are seen throughout the 1T′ bulk region for islands with the narrowest widths larger than ~8 nm. For 1T′ islands of smaller widths the zero-bias feature is replaced by a larger size dependent energy gap that opens at E_F and dominates the electronic structure, ostensibly due to size quantization effects24. The bulk gap feature observed by STM spectroscopy at $V_s = -130$ mV is consistent with the ARPES bulk bandgap for 1T′–WSe_2 when lifetime broadening effects are taken into account (See Supplementary Note 3 of ref[74]). Such broadening likely arises from a combination of electronic, vibrational, and defect-based scattering, as well as coupling to the graphene substrate.[134]

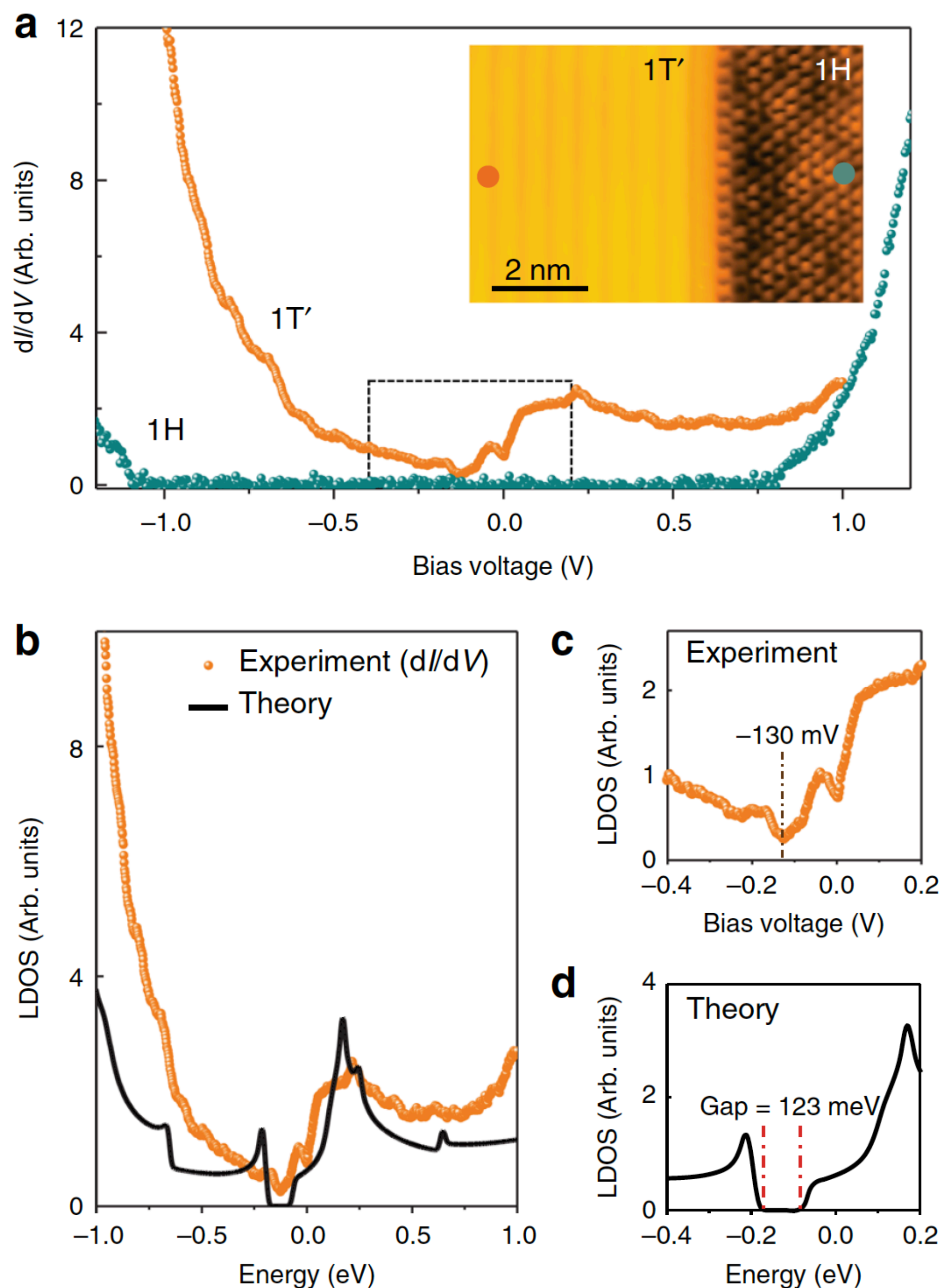

Figure 4.10| STS characterization of single-layer mixed-phase WSe_2. a, STS spectra obtained in the 1T′ (orange) and 1H (blue) regions of single-layer WSe_2 ($f = 614$ Hz, $I_t = 0.3$ nA, $V_{rms} =$ 4meV). The inset shows an STM image of coexisting 1T′ and 1H regions with a well-ordered interface between them ($V_s = +500$ mV, $I_t = 0.1$ nA). b, Calculated LDOS(E) of bulk single-layer 1T′–WSe_2 (black curve) compared to experimental STS spectrum (orange curve). c, Close-up view of the boxed region in a shows low-energy experimental STS spectrum taken for 1T′–WSe_2 phase. d, Calculated LDOS (E) for 1T′–WSe_2 over the same energy range as in c.

In order to further understand the electronic structure of single-layer 1T′–WSe_2, we also characterized its quasiparticle interference (QPI) patterns near E_F via Fourier transform (FFT) analysis of dI/dV images. Figure 4.11b–d show constant-bias dI/dV maps taken in the same pristine region of 1T′–WSe_2 for energies within the CB (b and c) as well as in the VB (d). The QPI patterns observed in the dI/dV maps exhibit long-range oscillations with wave fronts parallel to the x-direction and closely spaced rows aligned parallel to the y-direction (i.e., the atomic rows). The corresponding FFT images of the conductance maps (Fig. 4.11e–g) show distinct features that reflect the band structure contours at these different energies.

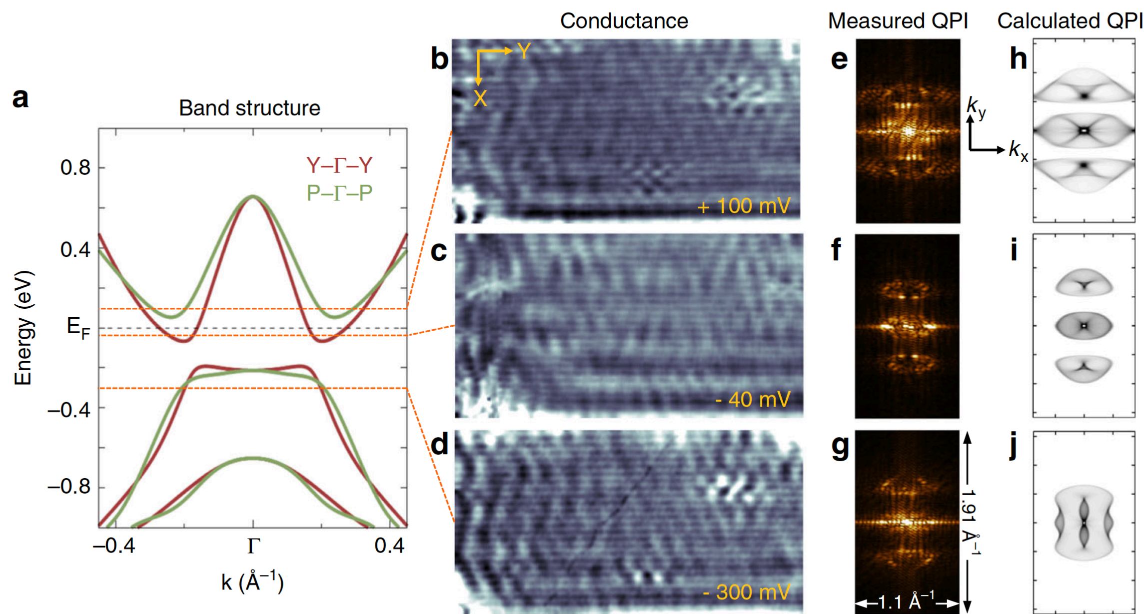

Figure 4.11| Quasiparticle interference patterns in single-layer 1T′–WSe_2. a, Calculated band structure of single-layer 1T′–WSe_2 along Γ-Y (brown) and Γ-P (green) directions in the ± 1 eV range. b–d, Experimental dI/dV conductance maps taken at b, V_s=+100 mV, I_t = 0.15 nA, c, V_s= − 40 mV, I_t = 0.15 nA, and d, V_s = − 300 mV, I_t = 0.15 nA (14 nm × 26.4 nm, f= 614 Hz, V_{rms} = 4 meV). e–g, FFTs of the conductance maps in b–d. h–j, Calculated QPI patterns for h E = +100 meV, i, E = − 40 meV, and j, E = − 300 meV.

The electronic features we have described up to now for bulk single-layer 1T′–WSe_2 are consistent with an inverted bandgap and the occurrence of the QSHI phase. A key feature of QSHIs, however, is the existence of helical states at the boundaries. WSe_2 is particularly well-suited to explore the existence of such states due to the coexistence of the 1T′ and 1H phases, which leads to straight, defect-free interfaces as shown in Figs. 4.10a, 4.12a. Figure 4.12b shows a color-coded series of dI/dV spectra measured along the 5.3 nm-long black arrow in Fig. 4.12a oriented perpendicular to the 1T′–1H interface (the interface is marked by a dashed white line). The 1T′–1H interface is defined as the point where the STM topograph height reaches 50% of the height difference from the 1H average terrace height to the 1T′ average terrace height for V_s = − 0.52 V, I = 0.2 nA. This definition is also valid for other biases within the range −0.6 V < V_s

< −0.1 V and $I_t \leq 0.5$ nA (the 1T′ terrace is 2.9 ± 0.2 Å higher than the 1H terrace under these standard tunneling conditions). Figure 4.12b shows that the STS feature identified as the bulk bandgap at −130 meV is present in the bulk 1T′ material only for distances greater than 2 nm from the 1T′–1H interface.

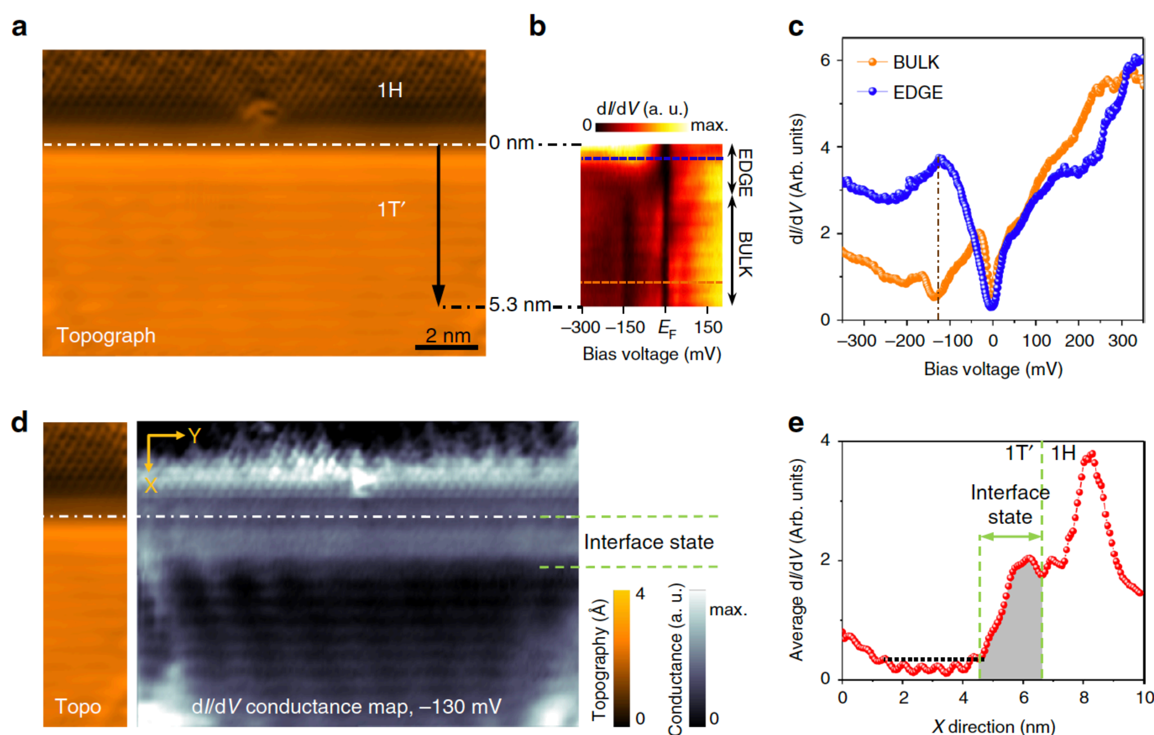

Figure 4.12| Spatial extent of atomically well-ordered 1D interface state in single-layer 1T′–WSe_2. a, STM topograph of the 1T′–1H interface (V_s = − 525 mV, I_t =0.2 nA). Dashed line shows interface location (see text). b, Color-coded dI/dV spectra taken along the path marked by the arrow in a (f = 614 Hz, I_t= 0.6 nA, V_{rms} =4 meV). c, dI/dV curves extracted from b. d, Experimental dI/dV map taken in the same region as a for V_s = − 130 meV. Dashed line shows same interface location as in a. e, Average dI/dV line scan oriented along the X direction in d for V_s = −130 mV.

The 1T′–WSe_2 bulk gap disappears at distances closer than 2 nm from the 1T′–1H interface and a prominent peak emerges in the LDOS at the same energy that previously showed a gap. This is illustrated in Fig. 4.12c which shows dI/dV curves taken in the bulk region (orange curve) and in the edge region (blue curve) as indicated by the dashed lines in Fig. 4.12b. The emergence of this peak is consistent with the existence of a 1D topologically protected edge state as expected for a QSHI. In order to resolve the spatial extent of the interface state, we mapped the dI/dV conductance near the 1T′–1H interface with sub-nm resolution. Figure 5d shows a dI/dV map of the same region shown in Fig. 4.12a at the bias voltage at the center of the interface-state peak (V_s = −130 meV). This map shows bright intensity in the 1H phase region

above the 1T′–1H interface. This is due to electronic states from the 1T′ phase leaking into the gapped 1H phase, similar to the phenomenon of metal-induced-gap-states (MIGS)[135]. Below the 1T′–1H interface in the 1T′ phase region a very uniform band of increased dI/dV intensity can be seen that penetrates 2 nm into the 1T′ bulk (marked interface state). This reveals the spatial extent of the topological interface state that resides in the bulk energy gap of single-layer 1T′–WSe_2 (see Fig. 4.12e for average line scan profile). The penetration depth of 2 nm that we extract from this line scan is in reasonable agreement with previous predictions for topological edge states.[65] (STM spectroscopy performed at the disordered edges of 1T′–WSe_2 islands also show the spectral signature of topologically protected edge states, but in this case disorder prevent any quantitative determination of edge-state width (see Supplementary Note 4 of ref[74]).

4.2.4 Density Functional Theory Calculations and Comparison with the Experiments.

In order to better understand the topological behavior of this mixed-phase system, we performed ab initio calculations using DFT (all the calculations were carried out by A. Pulkin, Q. Wu, and O. V. Yazyev). The resulting relaxed structure (Fig. 4.8a) is consistent with previous calculations for this phase[65] and agrees well with our STM topographic images (Fig. 4.8e). Figures 4.9e, 4.11a show the band structure along Y-Γ-Y (red) and P-Γ-P (green) directions over a wide energy range calculated using a hybrid functional. The results of our band structure calculations agree well with the ARPES results shown in Fig. 4.9 after performing a rigid shift of –130meV to account for the n-type doping observed in our samples. The non-parabolic flattened shape of the VB near the Γ-point closely follows the expected band structure arising from the inversion of bands having opposite parity[66], a prerequisite for topologically non-trivial electronic structure. The calculated band structure also shows an energy gap of 123meV with band edges along the ΓY direction, in reasonable agreement with both our ARPES and STS results.

Comparison of the calculated bulk 1T′–WSe_2 LDOS(E) with experimental STM dI/dV spectra shows qualitative agreement over a broad energy range as seen in Fig. 4.10b. The gap structure, the rise in VB LDOS as energy is decreased, and the CB peak feature near 0.2 eV are all observed. However, a quantitative comparison here would require calculating lifetime broadening effects (Supplementary Note 3 of ref[74]) as well as energy-dependent tunneling transmission probabilities. The dip feature observed in the STS at E_F is also not captured by our calculations, likely due to its origin from, either phonon-assisted inelastic tunneling28 or electron-electron interactions due to the Efros-Shklovskii mechanism.[133, 136] We have also simulated 1T′–WSe_2 QPI patterns that take into account the band inversion and gap opening seen in Fig. 4.11a. Figure 4.11h–j show the calculated QPI patterns for energies at + 100 meV, −40 meV, and −300 meV in comparison to the experimental QPI patterns of Fig. 4.11e–g. Here the agreement is reasonable for features such as the multi-lobe structure along ky and the elongation along kx, which are clearly seen for energies in the CB (Figs. 4.11e, h and 4.11f, i). In the VB (Fig. 4.11g, j), however, several high-intensity features in the calculated FFT are absent in the experimental data. The origin for this discrepancy may be due to either a lack of experimental resolution (due to limitations in the size of the 1T′ phase domains that were imaged to obtain the experimental FFTs) or to differences between the theoretical and experimental Fermi contours.

The calculated electronic structure for a single-layer WSe_2 1T′–1H interface model structure is shown in Fig. 4.13. The proposed interface model (Fig. 4.13a) was chosen because its electronic structure best matches our experimental data. Although the experimental interface has a well-defined crystallographic orientation, it is not possible to verify its atomic structure due to limitations in experimentally resolving the chemical bonds. Our calculation of the interface electronic structure was performed using a standard DFT approach due to the large model size. This results in a reduced band gap (29meV) compared to the more realistic bandgap (123 meV) of the more accurate hybrid functional calculations shown in Figs. 4.9–4.11. Despite this bandgap discrepancy, it is still useful to examine the wavefunction behavior resulting from this interface structure. Figure 4.13b shows the calculated dispersion of topologically protected interface states running parallel to the 1T′–1H interface shown in Fig. 4.11a. A total of three bands span the bulk band gap. The odd number of bands is consistent with a topological origin and spin-momentum locking is clearly manifested. The pair of bands at higher energy can be attributed to Rashba-split states derived from the bulk conduction band, but the band at lower energy is topological in origin since it connects bulk valence and conduction bands. Figure 6c demonstrates how extrema in the dispersion of these interface-state bands give rise to a large LDOS intensity within the bulk bandgap (marked by the black arrow), consistent with the experimental dI/dV curve in Fig. 4.12c. The decay of LDOS(E) with distance from the 1T′–1H interface (Fig. 4.13d, black curve) shows that these states are localized within approximately 2 nm of the interface in the 1T′ domain, consistent with the experimental interface-state decay length shown in Fig. 4.12d, e.

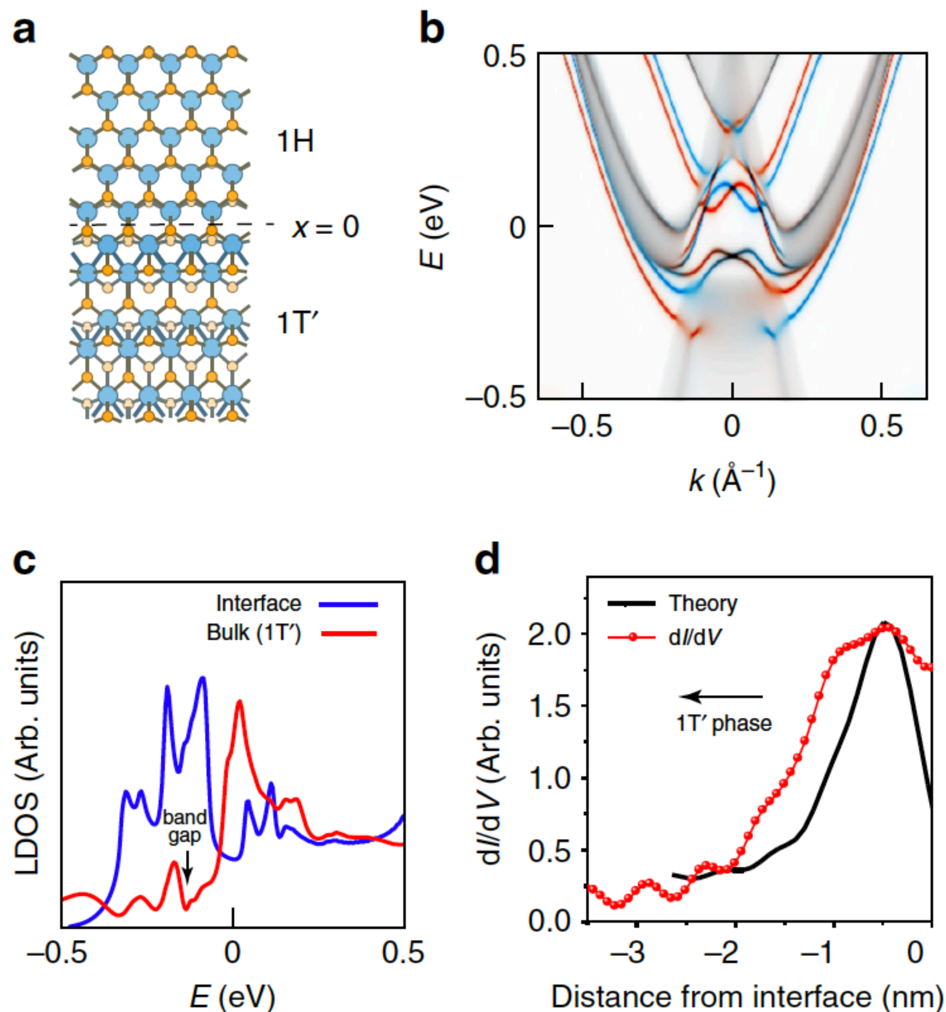

Figure 4.13| WSe_2 1T′–1H interface electronic structure. a, Sketch of the structural model used to theoretically investigate the 1T′–1H interface in single-layer WSe_2. The interface position x = 0 is indicated. b, Momentum- and spin resolved LDOS(E) at the 1T′–1H interface shows the dispersion and spin momentum locking of the interface states (blue/red curves show different spin polarizations). c, Energy-resolved LDOS at the 1T′–1H interface (blue curve) in single-layer WSe_2 compared to the LDOS at a point well within the 1T′ bulk region (red curve). d, Dependence of LDOS at the band gap energy on distance from the 1T′–1H interface compared to experimental dI/ dV line cut at $V_s = -130$ mV (from Fig. 4.12e)

4.2.5 Conclusion

Our measurements support the results of first principles calculations and provide evidence for the presence of the QSHI phase in single-layer 1T′–WSe_2. The ability to observe 1D interface-states at atomically well-ordered boundaries between trivial and nontrivial phases allows us to extract new quantitative information on these novel states, such as their penetration

depth into the 1T′–WSe_2 bulk, a previously inaccessible parameter due to edge disorder. This creates new opportunities for investigating topologically non-trivial electronic phases in 2D TMDs and takes us a step closer to the integration of 2D QSH layers into more complex heterostructures that exploit topologically protected charge and spin transport.

4.3 Manipulating Topological Domain Boundaries in the Single-layer Quantum Spin Hall Insulator 1T'–WSe_2

4.3.1 Introduction

As presented in sections 4.1 and 4.2, recent experimental studies have reported observation of the QSH effect in single layers of the TMDs WTe_2 and WSe_2 in the 1T' structural phase.[74, 75, 124, 125, 137] Moreover, QSH edge states have been observed to reside at 1T'/1H and 1T'/vacuum boundaries [74, 75, 125] in these materials. This is because the Z_2 invariant across these interfaces changes, and so they are expected to host topologically protected edge states. [45, 46, 58, 65, 66, 114]

A less well-studied type of boundary in quantum spin Hall insulator (QSHI) materials is the interface between different non-trivial domains where the Z_2 invariant does *not* change across the interface. We refer to a domain boundary as "topological" when there is a change in the topological invariant across the interface, and "trivial" when the invariant is the same on either side of the domain wall. A recent theoretical study of charge transport in quantum Hall insulators with trivial interfaces predicted that conduction through otherwise dissipationless quantum Hall edge states can be controllably deflected into the trivial interface states, thus enabling gate-tunable charge and spin transport.[67] Single-layer TMD materials create new opportunities for observing this predicted mixed topological interface behavior because they are known to switch between different phases under various stimuli.[115, 138-141] The 1T' phase, in particular, has recently been predicted to be ferroelastic in single layers, suggesting that it should be "switchable" between different dimerization orientations under applied stress, thus providing a potential mechanism for creating new interface types having different topological classification.[142, 143] Such switching has yet to be experimentally reported.

Here we report the local phase manipulation of single-layer 1T'–WSe_2 to create two kinds of one-dimensional interfaces: (1) trivial interfaces between two 1T' domains and (2) topological interfaces between 1T' and 1H domains. By using STM tip pulses we are able to locally switch from the 1T' to the 1H phase of WSe_2, as well as between different energetically equivalent orientations of the 1T' phase. 1T'/1T' domain-boundary formation is observed to be reversible, supporting the conjecture that 1T'–WSe_2 is a ferroelastic material.[143] Our STM measurements show that 1T'/1T' domain boundaries are well-ordered interfaces that exhibit several different symmetries. By combining STS measurements and first-principles calculations, we have determined that 1T'/1T' domain boundaries exhibit conducting, topologically unprotected 1D states that are dispersive in energy near the Fermi level. These states reside both inside the 1T'–bulk bandgap as well as in continuum regions of the bulk band structure, but their bands begin and end on the same side of the QSHI bandgap. This contrasts with 1T'/1H interface states which connect the conduction and valence bands of bulk 1T'–WSe_2.

4.3.2 STM Manipulation to Create Domain Boundaries in 1T'–WSe_2.

Mixed-phase single layers of WSe_2 were grown using molecular beam epitaxy (MBE) on bilayer graphene (BLG) supported by SiC. These samples exhibit islands that are single domains of either 1T' or 1H phase, as well as mixed-phase islands with coexisting 1T' and 1H domains.[74] Voltage pulses applied between the STM tip and monolayer 1T'–WSe_2 islands were used to manipulate the WSe_2 structural phase. Fig. 4.14 shows STM topographic images of a 1T'–WSe_2 island before and after application of STM tip pulses. The "before" image (Fig. 4.14a) shows a single-domain region of the 1T' phase with a uniform orientation of atomic rows running from top to bottom (each row contains a zigzag chain of W atoms[65, 66, 74, 75]). Fig. 4.14b shows the same region after a voltage pulse of 10 V was applied for 100 ms between the tip and surface at a constant tip-surface separation of ~6 Å. After the pulse the island exhibits multiple domains having different rotational orientation that are separated by 1T'/1T' domain boundaries (such tip pulses also cause the formation of adsorbate clusters near domain boundaries, as shown in Fig. 4.15).

The 1T' phase can exist in three orientational variants that result from spontaneous Peierls distortion of its C_3-symmetric 1T parent phase, and so 1T'/1T' domain boundaries are expected to exhibit different symmetries depending on the relative orientation of the adjacent 1T' domains.[143] The most commonly observed 1T'/1T' interface (> 85% in our samples) is the 120° domain boundary that occurs when the zigzag chains of the neighboring domains meet at a 120° angle with a slight lateral shift (Figs. 4.18a,b). Other observed domain boundaries occur when the zigzag chains meet at 60° and 0° (further details are discussed in section 4.3.6). These well-ordered domain boundaries are straight-line defects that we have observed to extend up to 20 nm in length. The formation of 1T'/1T' domain boundaries is reversible through application of a high current raster scan (300mV, 1nA). Such scans remove the adsorbate clusters that form during the generation of 1T'/1T' domains, likely changing local strain distributions. This provides additional evidence of the ferroelastic nature of 1T'–WSe_2 (further details are discussed in section 4.3.3).

Local conversion of single-layer WSe_2 from the 1T' phase to the 1H phase can also be induced using the same voltage pulse method. Fig. 4.14c shows a different single-phase 1T' island where the dimer chains run from top to bottom before applying a tip pulse, while Fig. 4.14d shows the same region after applying a voltage pulse of 10 V for 100 ms. Here the tip pulse causes an extended region of the island to convert to a new phase that exhibits reduced apparent height. Further investigation allows this region to be identified as 1H phase WSe_2 (see Fig. 4.16). Such 1T' to 1H phase conversion was only observed in "confined" regions as seen here (i.e., fabricated 1H domains were always surrounded by 1T' or 1H material).

While 1T'/1T' domain boundaries could be created by applying tip pulses with $V_{pulse} \geq 6$ V, stronger tip pulses ($V_{pulse} \geq 10$ V) were required to locally induce the 1T' to 1H phase transition. These observations are in agreement with predictions that the transition barrier for 1T' orientational variant switching should be much lower than the barrier associated with 1T'→1H phase transitions.[143] Tip pulses with $V_{pulse} > 6$ V often caused damage to 1T' islands. However,

we found that successfully induced 1T'/1T' and 1T'/1H domain structures are stable under normal scan conditions.

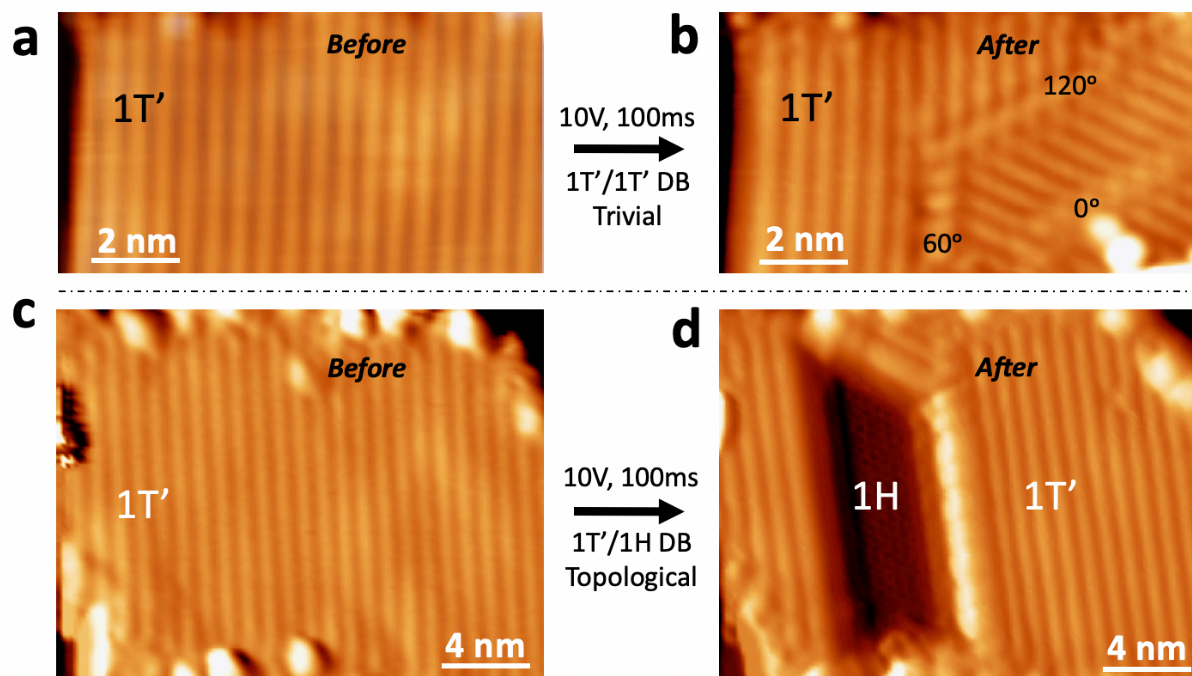

Figure 4.14| STM tip-induced structural change in monolayer 1T'–WSe_2. STM topographic images of a monolayer 1T'–WSe_2 island a, before and b, after applying a tip voltage pulse (V_{pulse}= 10 V, Δt = 100ms, tip-surface separation = 6 Å). The tip pulse creates 1T'/1T' domain boundaries (DBs) having different rotational orientations. STM topographic images show a different island c, before and d, after an applied tip voltage pulse (V_{pulse}= 10 V, Δt = 100 ms, tip-surface separation = 6 Å) induces a 1T' to 1H structural phase transition near the center of the island. V_s = 1V , I_t =10 pA, T = 4.5 K for all images. (Image intensity here is proportional to dz/dx (where z is height) in order to enhance contrast between regions having different structural phases.)

4.3.3 Evidence for Ferroelasticity

Fig. 4.15a shows a topographic STM image after applying a 10 V tip voltage pulse on a single-domain island. Contaminants appear on the island and multiple 1T' rotated domains separated by 1T'/1T' domain boundaries are formed. Fig. 4.15b shows the same area after positioning the tip close to the surface and raster-scanning over the sample with relatively large tunnel current (1 nA). The contaminants on the substrate our now mostly gone and the island no longer exhibits any 1T'/1T' domain boundaries. The island is now a single, homogeneous 1T' domain with only one orientation. Similar behavior was observed numerous times in large islands, where contaminants on the surface appeared to aid in 1T'/1T' domain boundary

formation and removal of the contaminants caused restoration of the original single 1T' domain. These measurements provide evidence that 1T'–WSe_2 is ferroelastic since the contaminants likely cause strain in the 1T' layer, thus explaining why their removal restores the island to its original state. Strain signatures are also present in the 1T' to 1H phase transition process. 1T'/1T' domain boundaries are observed in all islands that underwent the phase transition from 1T' to 1H (1T'/1T' domain boundaries in Fig. 4.14b are boxed by dashed lines in Fig. 4.16).

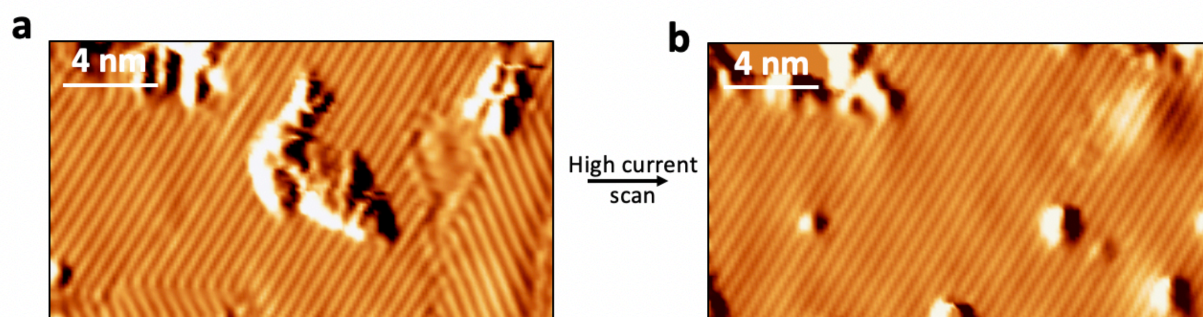

Figure 4.15| Reversibility of 1T'/1T' domain formations. a, STM topographic image of a monolayer 1T'–WSe_2 island after applying a voltage pulse (V_{pulse} = 10 V). b, STM topographic image of the same island imaged after scanning with high current (1 nA). (Tunneling parameters: V_s = 1V; I_t =10 pA; T = 4.5 K for all measurements, image intensity proportional to magnitude of dz/dx where z is STM tip height.)

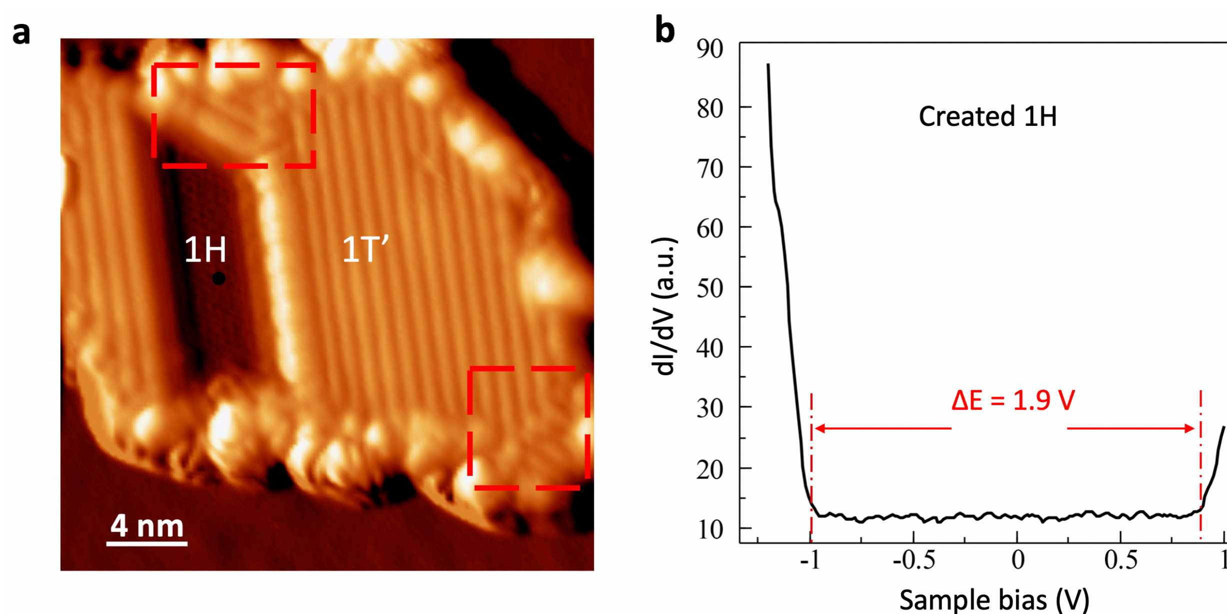

Figure 4.16| 1T' to 1H phase transition. a, STM image of a 1H domain created by applying a tip voltage pulse (V_{pulse} = 10 V, Δt = 100 ms, tip height ~ 6 Å) to monolayer 1T'–WSe_2. Red dashed boxes indicate small 1T'/1T' domain boundaries. b, STM dI/dV spectroscopy measured at the black circle reflects the semiconducting nature of the 1H domain. (Initial tunneling

parameters: f = 613.7 Hz, V_{ac} = 40 mV, I = 100 pA, V_s = –1.3 eV, T = 4.5 K, image intensity proportional to dz/dx where z is STM tip height).

4.3.4 Electronic Characterization of 120° 1T'/1T' Domain Boundaries

In order to explore the electronic structure of topologically unprotected interfaces in a QSHI, we performed STS on the 1T'/1T' WSe_2 rotational domain boundaries. We focus here on the behavior of 120° domain boundaries, which are by far the most numerous (see Supplementary sections 1 and 2 for discussion of the 60° and 0° domain boundaries of ref. [76]). Fig. 4.17c shows dI/dV spectroscopy measurements taken in the 2D bulk of the upper 1T' domain bracketing the 1T'/1T' domain boundary seen in Fig. 4.17a (red dot), as well as spectroscopy taken directly on the 120° 1T'/1T' domain boundary (black dot). The dI/dV spectrum obtained in the 1T' bulk (red curve in Fig. 4.17a) reflects the 1T'–WSe_2 bulk bandgap which has a size of 85 ± 21 mV centered at –130 ± 5 mV mV (this offset is due to n-doping of the 1T'–WSe_2 by the substrate[74]). The narrow dip at E_F is a pseudogap that has been reported in other STM studies of 1T'–TMD materials and has been suggested to be a Coulomb gap.[74, 125, 133, 144] The dI/dV spectrum measured at the 120° 1T'/1T' domain boundary is very different from the bulk 1T' measured spectra. Here the dI/dV spectrum exhibits a steep slope starting from V_s = 0 V that extends over a broad energy range into the filled state regime (–400 mV < V_s< 0 V), and the 1T'–WSe_2 bulk bandgap is not seen. There is also no sign of the topologically protected edge state that is observed at 1T'/vacuum and 1T'/1H interfaces[74, 75, 125] (as reference the topological edge state at the 1T'/vacuum interface for this island was also measured using dI/dV spectroscopy (see Fig. S8 in Supplementary of ref. [76]).

We mapped the spatial distribution of states at the 1T'/1T' domain boundary by performing dI/dV imaging over the energy range –400 mV < V_s < 150 mV. Fig. 4.18a shows an STM topograph of a mixed-phase WSe_2 island where a 1T'/1H boundary is marked by a vertical dashed line (the 1T' phase is to the right) and a 120° domain boundary created via tip pulse is marked by a dashed oval. This region is used to directly compare the electronic structure of "topological" and "trivial" domain boundaries.

Fig. 4.18b shows a dI/dV map measured at –400 mV, which corresponds to an energy below the bottom of the bulk 1T'–WSe_2 bandgap shown in Fig. 4.17c, i.e. the valence band states. Bright regions corresponding to a high LDOS are observed at the 120° domain boundary while the LDOS near the 1T'/1H interface shows low intensity. Fig. 4.18c shows a dI/dV map at –120 mV, an energy that lies inside the 1T' bulk bandgap. At this energy high LDOS intensity is observed at both the 120° domain boundary and the 1T'/1H interface (where the topologically protected interface state is marked with a white dashed box). Fig. 4.18d shows a dI/dV map measured at –60 mV, which corresponds to an energy near the upper edge of the bulk bandgap. Here high-intensity LDOS is observed near the 1T'/1H interface due to the topologically protected edge state, while the LDOS at the 120° domain boundary shows no intensity. Fig. 4.18e shows a dI/dV map measured at +150 mV, which corresponds to an energy well outside the 1T'–bulk bandgap. At this energy neither the topologically protected 1T'/1H interface state nor the trivial 120° domain boundary shows any intensity. These images show how topologically protected interface states co-exist with trivial defect modes in some energy windows but not in

others (such behavior has been predicted to provide a means of switching between different transport regimes by tuning a gate voltage, as discussed in ref. [67]).

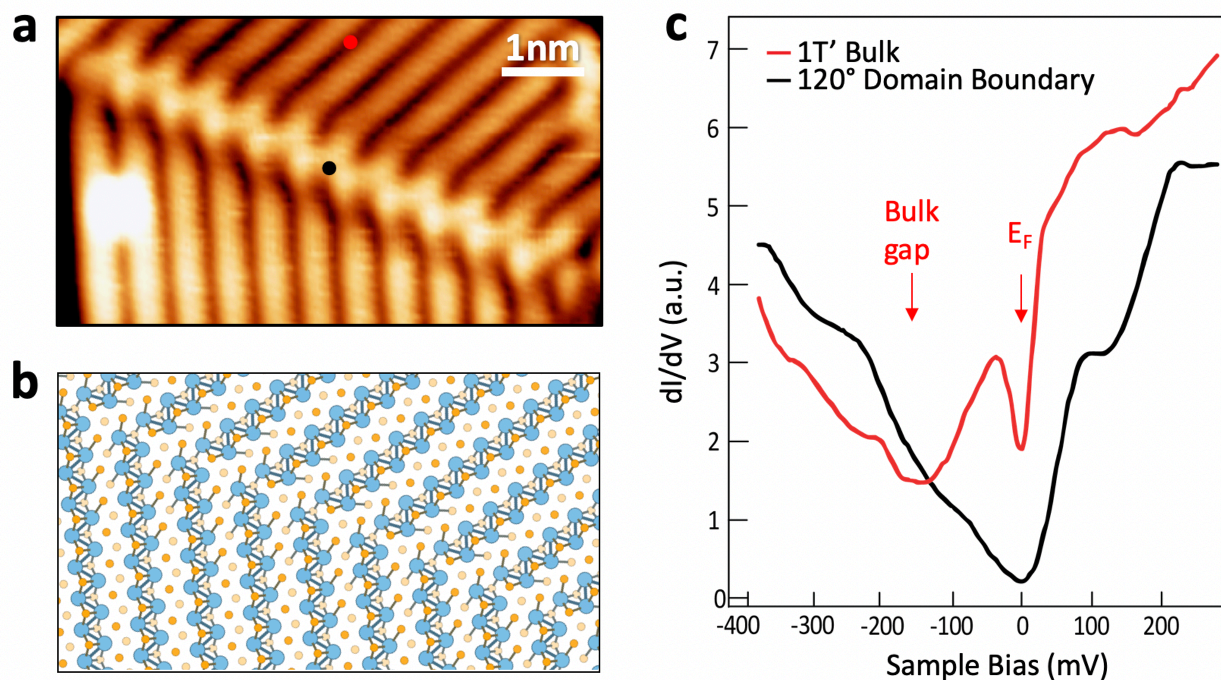

Figure 4.17| Structural and electronic properties of a 120° 1T'/1T' domain boundary. a, STM image of a 120° 1T'/1T' domain boundary in 1T'–WSe_2 (V_s = 1 V, I_t = 10 pA, standard STM topographic). b, Relaxed structure of the 120° domain boundary in 1T'–WSe_2 calculated using DFT. c, STM d*I*/d*V* spectroscopy measured at the 120° domain boundary in a, as well as in the island bulk (spectroscopy positions marked by black and red dots in a) (f = 613.7 Hz, V_{ac} = 4 mV, T = 4.5 K. Initial tunneling parameters for spectroscopy measurements: V_s = –400 mV, I = 100 pA).

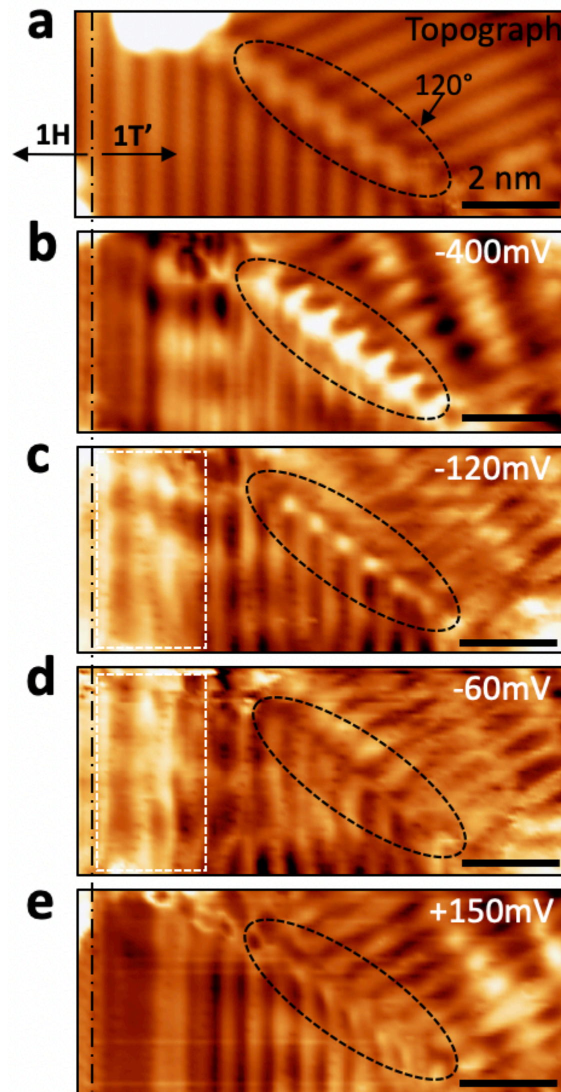

Figure 4.18| Comparison of electronic properties of 120° 1T'/1T' domain boundary and 1T'/1H boundary. a, STM topographic image of a mixed-phase WSe_2 island with a 120° 1T'/1T' domain boundary. The 1T'/1H interface is marked by a vertical dashed line while the 1T'/1T' interface is outlined by a dashed oval ($V_s = 1$ V, $I_t = 10$ pA). dI/dV maps of the same area are shown for b, $V_s = -400$ mV, c, –120 mV, d, –60 mV, and e, +150 mV. Spectroscopy parameters: $f = 613.7$ Hz, $V_{ac} = 4$ mV, I = 100pA, $T = 4.5$ K. Dashed white box outlines the topologically-protected edge-state.

4.3.5 Density Functional Theory Calculations and Comparison with the Experiments.

In order to clarify the origin of the features observed here for different classes of topological interfaces, we performed first-principles calculations using DFT. A schematic illustration of the different possible interface state electronic behavior (trivial and non-trivial) is given in Figs. 4.19a,b, where ballistic flow of charge carriers having different spin polarization is indicated. Our simulations of WSe_2 domain boundaries and edges were performed in two steps. First, the atomic structures of the interfaces were relaxed using periodic boundary conditions in a ribbon geometry using a plane-wave basis set[107] (the resulting relaxed structures are shown in the insets to Figs. 4.19c,d). Second, we used the non-equilibrium Green's function method (NEGF) to model line defects with semi-infinite boundary conditions. The Hamiltonian matrix elements for the second step were obtained in a localized basis set using the OpenMX package[145, 146].

The calculated electronic structure of the different interfaces is presented in Figs. 4.19c,d as a function of energy, spin, and wavenumber. Vacuum-terminated 1T'–WSe_2 (Fig. 4.19c) exhibits gapless topological edge states spanning the bulk bandgap, consistent with the non-trivial Z_2 index of this phase (this has been demonstrated previously for other 1T'–MX_2 materials[74, 75, 125]). In contrast, interface states at the 120° 1T'/1T' boundary shown in Fig. 4.19d do not close the bulk bandgap. Charge carries with either spin polarization traveling along the interface here are able to backscatter (as illustrated in the sketch of Fig. 4.19b) as a consequence of the non-zero energy gap value ≈ 20 mV. Our calculations show that the 120° domain boundary has four localized modes, consistent with the broad spectroscopic feature observed experimentally for 120° domain boundaries in Fig. 4.17c (the absence of a clear gap feature in the experimental data likely arises from lifetime effects and strain which can close small energy gaps[134]). The 1T'/1T' domain boundary states are spin-polarized out of plane, (colors in Figs. 4.19c,d). The spin polarization and band dispersion of these states show a typical Rashba-type splitting[147] consistent with the fact that 1T'/1T' domain boundaries do not possess an inversion center.

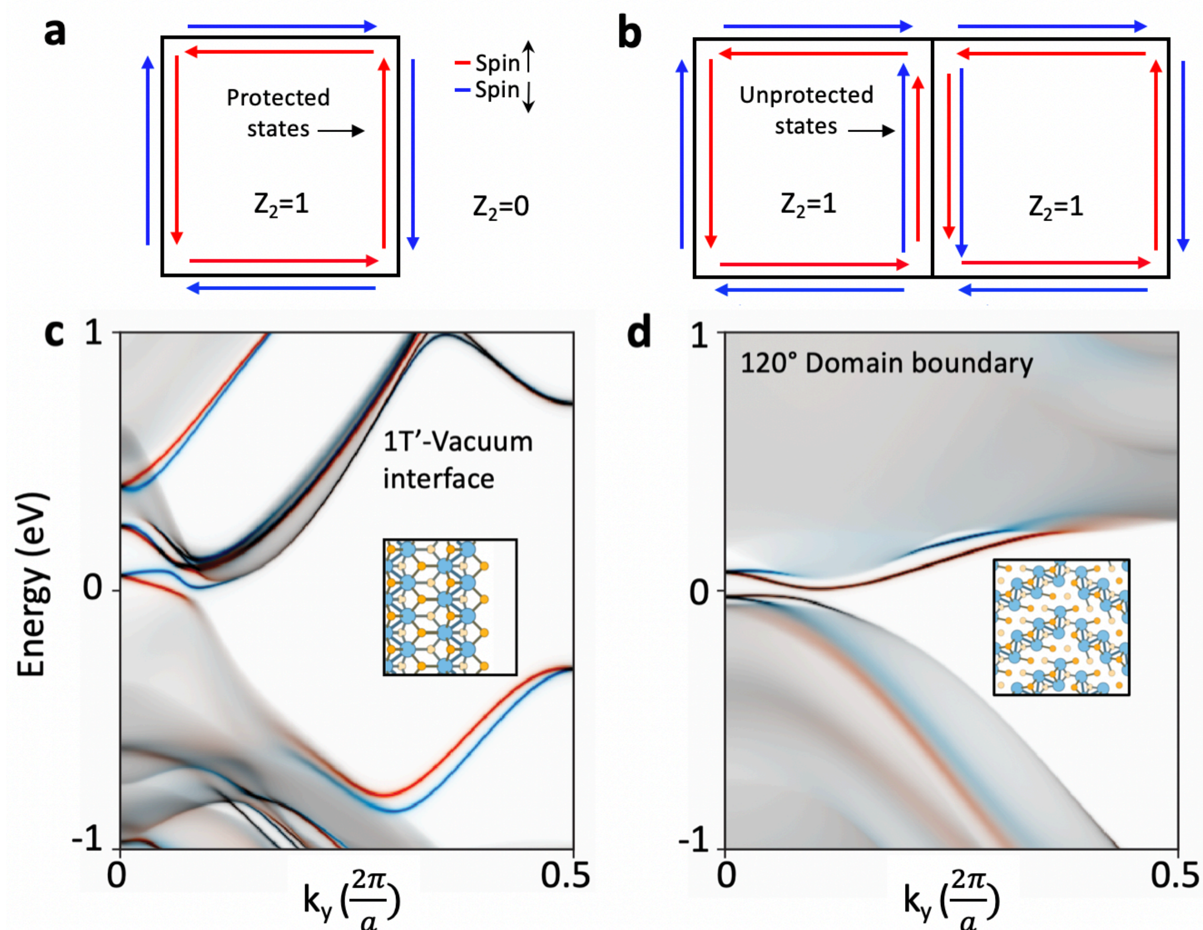

Figure 4.19| Band Structure of 1T'/vacuum and 120° 1T'/1T' domain boundaries in single-layer WSe_2. a, Schematic representation of a QSHI terminated by vacuum. b, Schematic representation of two different QSHIs fused at a single interface. c, Calculated band structure of zigzag edge of vacuum-terminated 1T'–WSe_2 monolayer (inset shows relaxed chemical structure). d, Calculated band structure of 120° 1T'/1T' domain boundary for 1T'–WSe_2 monolayer (inset shows relaxed chemical structure). Bulk states are grey and spin-polarized interface modes are red and blue.

4.3.6 Theoretical and Experimental Characterization of 60° and 0° 1T'/1T' Domain Boundaries

Structural and electronic data regarding 0° and 60° domain boundaries are presented in Fig. 20. The 0° domain boundary is the second most common type of induced 1T'/1T' domain boundary, comprising ~ 13% of observed domain boundaries, while the 60° domain boundary is the least common type (~2% of observed domain boundaries). STM spectroscopy measured on 60° domain boundaries exhibits a broad spectroscopic feature that fills the bulk bandgap (Fig. 20c). This is similar to STS measurements of the 120° domain boundary shown in Fig. 4.17 of the manuscript. STS measurements of the 0° domain boundary are quite different. Such measurements still exhibit the bulk bandgap as seen in Fig. 20f. Detailed position-dependent

spectroscopic measurements show that the signature of the bulk gap is always observed in STS measured at 0° domain boundaries (Fig. 4.21).

To better understand the nature of 60° and 0° 1T'/1T' domain boundaries in WSe_2, first principles calculations with open boundary conditions using the Green's function method were carried out. Fig. 4.22a presents the calculated band structure for a 60° domain boundary. The results of our structural calculation are shown in Fig. 4.20b and predict that the two domains near the 60° line defect have a slight lattice mismatch, resulting in a slight shift in the bulk band structure. This is the reason why the calculated bulk band structure in Fig S3a is more complicated than the other two domain boundary cases (Fig. 4.18b and Fig. 4.19d). Here the colored bands are the trivial states that exist at the domain boundary, with the different colors indicative of spin polarization. These trivial states can be thought of as arising from the mixing of topological edge states on the boundaries of each 1T' domain. Because the two 1T' domains have the same Z_2 invariant, currents of the same spin travel in opposite directions at the boundary, and thus backscattering is allowed. The number of bands explains the broad energy features measured by STS at the domain boundary. Although the band structure for the 60°domain boundary looks more complicated than the band structure for the 120° domain boundary, qualitatively they are very similar since they both lift the spin degeneracy of the topological edge state, they both exhibit trivial states that reside in the bulk gap and extend to lower energies in the bulk band structure, and they both exhibit an STS feature that is broad in energy and very localized to the domain boundary.

The calculated band structure of the 0° domain boundary is presented in Fig. 4.22b. This calculation shows no new domain boundary states inside the bulk bandgap. At the 0° domain boundary, the spin degeneracy of the topological edge state is also lifted. However, here the hybridization of states creates bands that coincide with the VB and CB edges, which is why no domain boundary states are observed. This is in agreement with our experimental measurements which always exhibit the bulk gap when STS spectroscopy is performed on 0° domain boundaries.

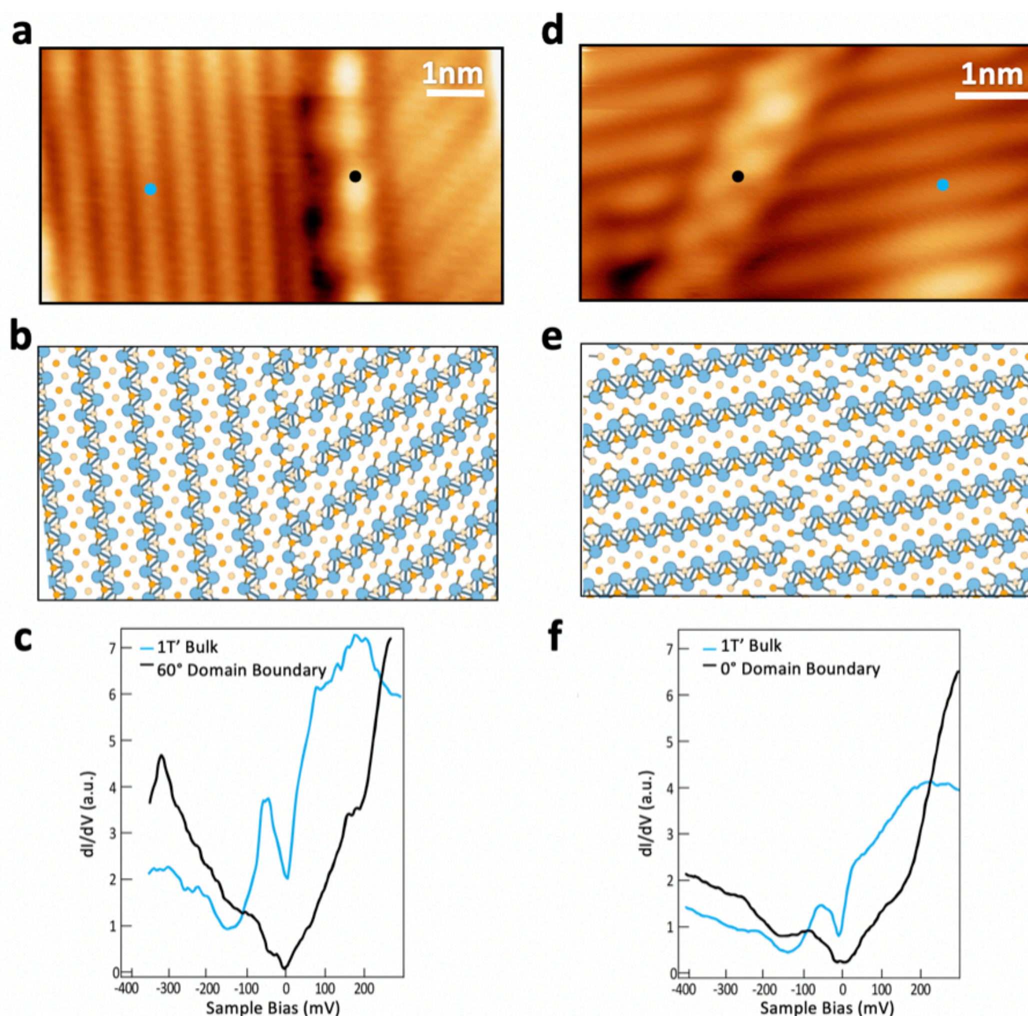

Figure 4.20| Structural and electronic properties of the 60° and 0° domain boundaries. a, STM image of 60° domain boundary (V_s = 1.6 V, I_t =10 pA, standard STM topograph). b, Calculated relaxed structure of the 60° domain boundary. c, STM d*I*/d*V* spectroscopy measured at the 60° domain boundary as well as the bulk of the 1T'–WSe_2 island (positions indicated by black and blue dots in a). (Initial tunneling parameters: *f* = 613.7 Hz, V_{ac} = 4 mV, I=100 pA, V_s = –350 mV). d, STM topographic image of 0° domain boundary (V_s = 1 V, I_t =10 pA). e, Calculated relaxed structure of the 0° domain boundary. f, STM d*I*/d*V* spectroscopy measured at the 0° domain boundary as well as the bulk of the 1T'–WSe_2 island (positions indicated by black and blue dots in d) (*f* =613.7 Hz, V_{ac} = 4 mV, I = 100 pA, V_s = –400 mV). *T* = 4.5 K for all measurements.

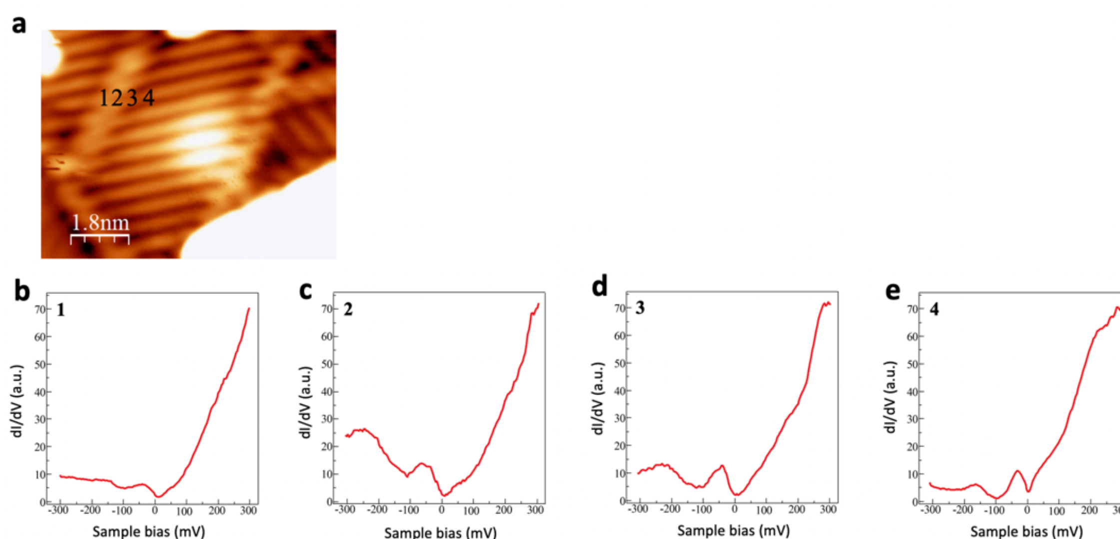

Figure 4.21| Position-dependent STS of 0° 1T'/1T' domain boundary in single layer 1T'–WSe_2. a, STM image of 1T'–WSe_2 with 0° domain boundary (standard STM topograph). b-d, dI/dV spectra obtained at locations on and near 0° domain boundary as marked in a (initial tunneling parameters: f = 613.7 Hz, V_{ac} = 4 mV, I = 100 pA, V_s = –400 mV, T = 4.5 K).

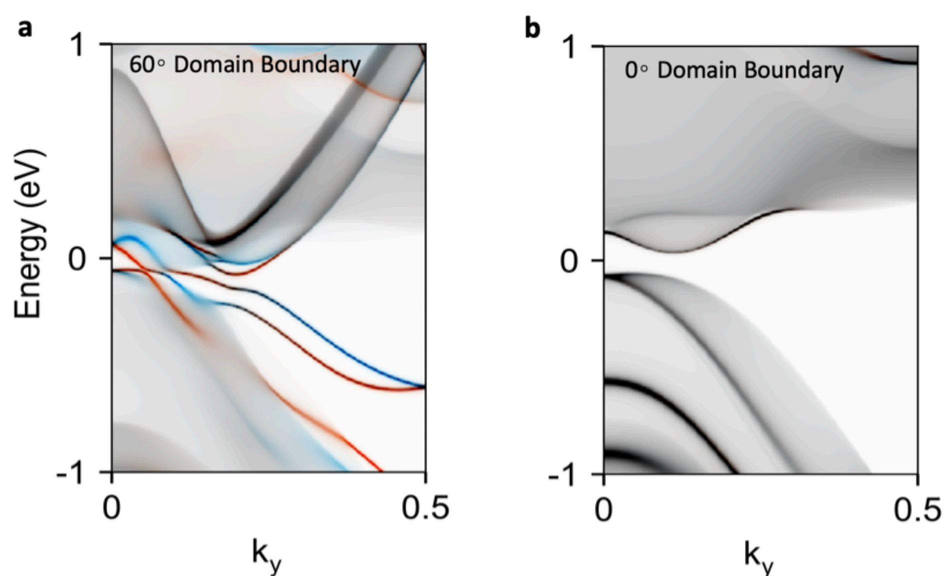

Figure 4.22| Calculated band structures for 60° and 0° 1T'/1T' domain boundaries in single-layer WSe_2. Band structures of a, 60° domain boundary and b, 0° domain boundary are calculated using the non-equilibrium Green's function method. Shaded gray areas indicate bulk band structure while the colored bands are domain-boundary states. The 0° domain boundary does not exhibit any interface states in the gap.

4.3.7 Non-Trivial and Trivial Two-Channel System

Here we describe how trivial 1T'/1T' domain boundaries could potentially provide a useful conduction channel in a hypothetical two-channel device made from single-layer 1T'–WSe_2. For simplicity we will focus on only one spin direction. Following the reasoning described in ref. 12, a trivial domain boundary channel can act as a pathway that short-circuits QSH edge states. Backscattering is allowed in the domain boundary channel but is suppressed if the boundary is sufficiently clean. QSH channels bisected by such trivial domain boundaries can be turned "on and off" by tuning the chemical potential into and out of an energy range that coincides with domain boundary states (Fig. 4.23). At energies near the top of the bulk gap (close to where the 120° domain boundary is expected to have a small bandgap (Figs. 4.18d, 4.19d)) the trivial channel is turned off. However, at slightly lower energies (Fig. 4.18c) outside the small bandgap, the 120° domain boundary hosts states and hence could reroute QSH current either fully or partially, similar to behavior predicted for graphene in the quantum Hall regime[67] (Fig. 4.23).

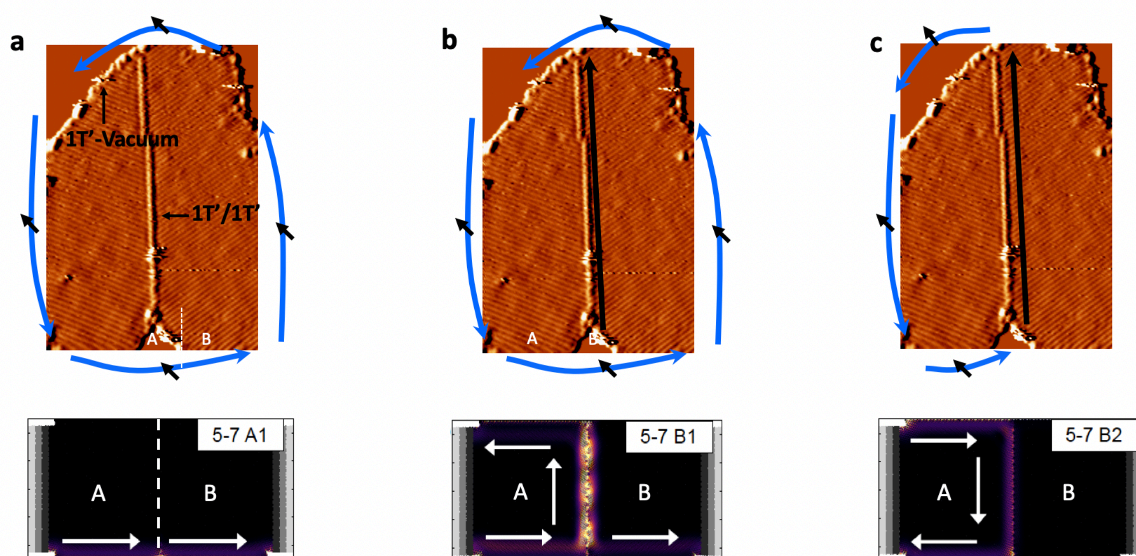

Figure 4.23| Trivial/topological two-channel system. a-c, Upper images are the same STM image of a single 120° domain boundary connecting QSH edge states for 1T'–WSe_2 (V_s = 1V, I = 10 pA, T = 4.5 K, image intensity proportional to magnitude of dz/dx where z is STM tip height). Arrows are drawn to indicate the possible direction of spin-polarized current in a hypothetical device which (depending on gate voltage) could either a, bypass the trivial domain boundary state, or b, be rerouted partially, or c, be rerouted fully. The lower images are model calculations of an analogous graphene device structure taken from Philips et al.[67] Here the A and B regions are graphene domains separated by a 5-7 grain boundary located at the position of the white dashed line.

4.3.8 Conclusion

We have demonstrated successful manipulation of the electronic and structural properties of monolayer 1T'–WSe_2 by applying local voltage pulses to induce several kinds of topological and trivial domain boundaries co-existing on the same sample. The domain boundaries observed are ordered and host one-dimensional modes (protected or unprotected), as evidenced by spectroscopic measurements and density functional theory. The reversibility of 1T'/1T' domain boundary creation provides evidence for the ferroelastic nature of 1T'–WSe_2.

These results point toward a possible means of realizing two-channel conductance involving different classes of topological boundaries (Fig. 4.23). The energy-dependent dI/dV maps in Fig. 4.18, for example, indicate that the chemical potential of a single-layer TMD device could be tuned to access both unprotected and protected channels either separately (Figs. 4.18b, d) or simultaneously (Fig. 4.18c), thus deflecting current in QSH edge states either fully (Fig. 4.23c) or partially (Fig. 4.23b) into 120° domain boundary states. This provides a mechanism to turn off the conductance of QSH edge states through the manipulation of topological domains in 2D materials. The spin-polarized nature of the 120° domain boundary states creates opportunity for future spin-based devices.[67]

Bibliography

1. Miyamoto, Y.; Nakada, K.; Fujita, M. *Physical Review B* **1999,** 59, (15), 9858-9861.

2. Wakabayashi, K.; Fujita, M.; Ajiki, H.; Sigrist, M. *Physical Review B* **1999,** 59, (12), 8271-8282.

3. Nakada, K.; Fujita, M.; Dresselhaus, G.; Dresselhaus, M. S. *Physical Review B* **1996,** 54, (24), 17954-17961.

4. Brey, L.; Fertig, H. A. *Physical Review B* **2006,** 73, (23), 235411.

5. Ezawa, M. *Physical Review B* **2006,** 73, (4), 045432.

6. Sasaki, K.-i.; Murakami, S.; Saito, R. *Journal of the Physical Society of Japan* **2006,** 75, (7), 074713.

7. Okada, S.; Oshiyama, A. *Physical Review Letters* **2001,** 87, (14), 146803.

8. Lee, H.; Son, Y.-W.; Park, N.; Han, S.; Yu, J. *Physical Review B* **2005,** 72, (17), 174431.

9. Fujita, M.; Wakabayashi, K.; Nakada, K.; Kusakabe, K. *Journal of the Physical Society of Japan* **1996,** 65, (7), 1920-1923.

10. Abanin, D. A.; Lee, P. A.; Levitov, L. S. *Physical Review Letters* **2006,** 96, (17), 176803.

11. Chen, Y.-C.; de Oteyza, D. G.; Pedramrazi, Z.; Chen, C.; Fischer, F. R.; Crommie, M. F. *ACS Nano* **2013,** 7, (7), 6123-6128.

12. Castro Neto, A. H.; Guinea, F.; Peres, N. M. R.; Novoselov, K. S.; Geim, A. K. *Reviews of Modern Physics* **2009,** 81, (1), 109-162.

13. Son, Y.-W.; Cohen, M. L.; Louie, S. G. *Physical Review Letters* **2006,** 97, (21), 216803.

14. Son, Y.-W.; Cohen, M. L.; Louie, S. G. *Nature* **2006,** 444, 347.

15. Yang, L.; Park, C.-H.; Son, Y.-W.; Cohen, M. L.; Louie, S. G. *Physical Review Letters* **2007,** 99, (18), 186801.

16. Cai, J.; Ruffieux, P.; Jaafar, R.; Bieri, M.; Braun, T.; Blankenburg, S.; Muoth, M.; Seitsonen, A. P.; Saleh, M.; Feng, X.; Müllen, K.; Fasel, R. *Nature* **2010,** 466, 470.

17. Dong, L.; Liu, P. N.; Lin, N. *Accounts of Chemical Research* **2015,** 48, (10), 2765-2774.

18. Sambiagio, C.; Marsden, S. P.; Blacker, A. J.; McGowan, P. C. *Chemical Society Reviews* **2014,** 43, (10), 3525-3550.

19. Xi, M.; Bent, B. E. *Surface Science* **1992,** 278, (1), 19-32.

20. Xi, M.; Bent, B. E. *Journal of the American Chemical Society* **1993,** 115, (16), 7426-7433.

21. Chen, Y.-C.; Cao, T.; Chen, C.; Pedramrazi, Z.; Haberer, D.; de Oteyza, D. G.; Fischer, F. R.; Louie, S. G.; Crommie, M. F. *Nature Nanotechnology* **2015,** 10, 156.

22. Pedramrazi, Z.; Chen, C.; Zhao, F.; Cao, T.; Nguyen, G. D.; Omrani, A. A.; Tsai, H.-Z.; Cloke, R. R.; Marangoni, T.; Rizzo, D. J.; Joshi, T.; Bronner, C.; Choi, W.-W.; Fischer, F. R.; Louie, S. G.; Crommie, M. F. *Nano Letters* **2018,** 18, (6), 3550-3556.

23. Nguyen, G. D.; Toma, F. M.; Cao, T.; Pedramrazi, Z.; Chen, C.; Rizzo, D. J.; Joshi, T.; Bronner, C.; Chen, Y.-C.; Favaro, M.; Louie, S. G.; Fischer, F. R.; Crommie, M. F. *The Journal of Physical Chemistry C* **2016,** 120, (5), 2684-2687.

24. Nguyen, G. D.; Tsai, H.-Z.; Omrani, A. A.; Marangoni, T.; Wu, M.; Rizzo, D. J.; Rodgers, G. F.; Cloke, R. R.; Durr, R. A.; Sakai, Y.; Liou, F.; Aikawa, A. S.; Chelikowsky, J. R.; Louie, S. G.; Fischer, F. R.; Crommie, M. F. *Nature Nanotechnology* **2017,** 12, 1077.

25. Ruffieux, P.; Wang, S.; Yang, B.; Sánchez-Sánchez, C.; Liu, J.; Dienel, T.; Talirz, L.; Shinde, P.; Pignedoli, C. A.; Passerone, D.; Dumslaff, T.; Feng, X.; Müllen, K.; Fasel, R. *Nature* **2016,** 531, 489.

26. Ruffieux, P.; Cai, J.; Plumb, N. C.; Patthey, L.; Prezzi, D.; Ferretti, A.; Molinari, E.; Feng, X.; Müllen, K.; Pignedoli, C. A.; Fasel, R. *ACS Nano* **2012,** 6, (8), 6930-6935.

27. Cloke, R. R.; Marangoni, T.; Nguyen, G. D.; Joshi, T.; Rizzo, D. J.; Bronner, C.; Cao, T.; Louie, S. G.; Crommie, M. F.; Fischer, F. R. *Journal of the American Chemical Society* **2015,** 137, (28), 8872-8875.

28. Kawai, S.; Saito, S.; Osumi, S.; Yamaguchi, S.; Foster, A. S.; Spijker, P.; Meyer, E. *Nature Communications* **2015,** 6, 8098.

29. Koch, M.; , F. A., Christian Joachim and Leonhard Grill. *Nature Nanotechnology* **2012,** 7, 713.

30. Cai, J.; Pignedoli, C. A.; Talirz, L.; Ruffieux, P.; Söde, H.; Liang, L.; Meunier, V.; Berger, R.; Li, R.; Feng, X.; Müllen, K.; Fasel, R. *Nature Nanotechnology* **2014,** 9, 896.

31. Fukui, T.; Hatsugai, Y.; Suzuki, H. *Journal of the Physical Society of Japan* **2005,** 74, (6), 1674-1677.

32. Holstein, B. R. *American Journal of Physics* **1989,** 57, (12), 1079-1084.

33. Nakahara, M., *Geometry, Topology and Physics* Adam Hilger, Bristol: 1990.

34. Berry Michael, V. *Proceedings of the Royal Society of London. A. Mathematical and Physical Sciences* **1984,** 392, (1802), 45-57.

35. Garg, A. *American Journal of Physics* **2010,** 78, (7), 661-670.

36. Resta, R.; TroisiËme cycle de la physique en Suisse, r., *Berry phase in electronic wavefunctions*. UniversitÈ, B,timent des sciences physiques, M.D. Reymond: Lausanne-Dorigny, 1996.

37. Xiao, D.; Chang, M.-C.; Niu, Q. *Reviews of Modern Physics* **2010,** 82, (3), 1959-2007.

38. *Advances in Physics* **1995,** 44, (5), 405-473.

39. Thouless, D. J. *Physical Review B* **1983,** 27, (10), 6083-6087.

40. Klitzing, K. v.; Dorda, G.; Pepper, M. *Physical Review Letters* **1980,** 45, (6), 494-497.

41. Richard E. Prange; ; Girvin, S. M., *The Quantum Hall Effect*. 2 ed.; Springer-Verlag New York: 1990.

42. Thouless, D. J.; Kohmoto, M.; Nightingale, M. P.; den Nijs, M. *Physical Review Letters* **1982,** 49, (6), 405-408.

43. von Klitzing, K. *Philosophical Transactions of the Royal Society A: Mathematical, Physical and Engineering Sciences* **2005,** 363, (1834), 2203-2219.

44. Haldane, F. D. M. *Physical Review Letters* **1988,** 61, (18), 2015-2018.

45. Hasan, M. Z.; Kane, C. L. *Reviews of Modern Physics* **2010,** 82, (4), 3045-3067.

46. Kane, C. L.; Mele, E. J. *Physical Review Letters* **2005,** 95, (22), 226801.

47. Fu, L.; Kane, C. L.; Mele, E. J. *Physical Review Letters* **2007,** 98, (10), 106803.

48. Fu, L.; Kane, C. L. *Physical Review B* **2007,** 76, (4), 045302.

49. Qi, X.-L.; Zhang, S.-C. *Reviews of Modern Physics* **2011,** 83, (4), 1057-1110.

50. Roy, R. *Physical Review B* **2009,** 79, (19), 195322.

51. Moore, J. E.; Balents, L. *Physical Review B* **2007,** 75, (12), 121306.

52. Murakami, S. *Journal of Physics: Conference Series* **2011,** 302, 012019.

53. Fukui, T.; Fujiwara, T.; Hatsugai, Y. *Journal of the Physical Society of Japan* **2008,** 77, (12), 123705.

54. Qi, X.-L.; Hughes, T. L.; Zhang, S.-C. *Physical Review B* **2008,** 78, (19), 195424.

55. König, M.; Wiedmann, S.; Brüne, C.; Roth, A.; Buhmann, H.; Molenkamp, L. W.; Qi, X.-L.; Zhang, S.-C. *Science* **2007,** 318, (5851), 766.

56. Knez, I.; Du, R.-R.; Sullivan, G. *Physical Review Letters* **2011,** 107, (13), 136603.

57. Nowack, K. C.; Spanton, E. M.; Baenninger, M.; König, M.; Kirtley, J. R.; Kalisky, B.; Ames, C.; Leubner, P.; Brüne, C.; Buhmann, H.; Molenkamp, L. W.; Goldhaber-Gordon, D.; Moler, K. A. *Nature Materials* **2013,** 12, 787.

58. Ma, Y.; Kou, L.; Li, X.; Dai, Y.; Smith, S. C.; Heine, T. *Physical Review B* **2015,** 92, (8), 085427.

59. Fabrizio, N.; Henri, J. S.; Morten, K.; Charles, M. M.; Ebrahim, S.; Joshua, A. F.; Fanming, Q.; Arjan, J. A. B.; Folkert, K. d. V.; Jasper van, V.; Stevan, N.-P.; Leo, P. K.; Binh-Minh, N.; Andrey, A. K.; Wei, Y.; Marko, S.; Michael, J. M.; Eric, M. S.; Kathryn, A. M. *New Journal of Physics* **2016,** 18, (8), 083005.

60. Liu, Z.; Liu, C.-X.; Wu, Y.-S.; Duan, W.-H.; Liu, F.; Wu, J. *Physical Review Letters* **2011,** 107, (13), 136805.

61. Xu, Y.; Yan, B.; Zhang, H.-J.; Wang, J.; Xu, G.; Tang, P.; Duan, W.; Zhang, S.-C. *Physical Review Letters* **2013,** 111, (13), 136804.

62. Weng, H.; Dai, X.; Fang, Z. *Physical Review X* **2014,** 4, (1), 011002.

63. Drozdov, I. K.; Alexandradinata, A.; Jeon, S.; Nadj-Perge, S.; Ji, H.; Cava, R. J.; Andrei Bernevig, B.; Yazdani, A. *Nature Physics* **2014,** 10, 664.

64. Reis, F.; Li, G.; Dudy, L.; Bauernfeind, M.; Glass, S.; Hanke, W.; Thomale, R.; Schäfer, J.; Claessen, R. *Science* **2017,** 357, (6348), 287.

65. Qian, X.; Liu, J.; Fu, L.; Li, J. *Science* **2014,** 346, (6215), 1344-1347.

66. Choe, D.-H.; Sung, H.-J.; Chang, K. J. *Physical Review B* **2016,** 93, (12), 125109.

67. Phillips, M.; Mele, E. J. *Physical Review B* **2017,** 96, (4), 041403.

68. Chen, C. J., *Introduction to Scanning Tunneling Microscopy*. 2nd ed.; Oxford University Press: **2008**.

69. Yamachika, R. T. Probing atomic-scale properties of organic and organometallic molecules by scanning tunneling spectroscopy. PhD thesis, University of California, Berkeley, **2009**.

70. Sakurai, J. J., *Moden Quantum Mechanics*. Inc., revised edition ed.; Addison-Wesley Publishing Company: **1994**.

71. Bardeen, J. *Physical Review Letters* **1961,** 6, (2), 57-59.

72. Tersoff, J.; Hamann, D. R. *Physical Review B* **1985,** 31, (2), 805-813.

73. Tersoff, J.; Hamann, D. R. *Physical Review Letters* **1983,** 50, (25), 1998-2001.

74. Ugeda, M. M.; Pulkin, A.; Tang, S.; Ryu, H.; Wu, Q.; Zhang, Y.; Wong, D.; Pedramrazi, Z.; Martín-Recio, A.; Chen, Y.; Wang, F.; Shen, Z.-X.; Mo, S.-K.; Yazyev, O. V.; Crommie, M. F. *Nature Communications* **2018,** 9, (1), 3401.

75. Tang, S.; Zhang, C.; Wong, D.; Pedramrazi, Z.; Tsai, H.-Z.; Jia, C.; Moritz, B.; Claassen, M.; Ryu, H.; Kahn, S.; Jiang, J.; Yan, H.; Hashimoto, M.; Lu, D.; Moore, R. G.; Hwang, C.-C.; Hwang, C.; Hussain, Z.; Chen, Y.; Ugeda, M. M.; Liu, Z.; Xie, X.; Devereaux, T. P.; Crommie, M. F.; Mo, S.-K.; Shen, Z.-X. *Nature Physics* **2017,** 13, 683.

76. Pedramrazi, Z.; Herbig, C.; Pulkin, A.; Tang, S.; Philips, M.; Wong, D.; Ryu, H.; Pizzochero, M.; Chen, Y.; Wang, F.; Mele, E. J.; Shen, Z. X.; Mo, S.-K.; Yazyev, O. V.; Crommie, M. F., Manipulating Topological Domain Boundaries in the Single-layer Quantum Spin Hall Insulator 1T’–WSe2

.

77. Chen, Y.-C. Exploring graphene nanoribbons using scanning probe microscopy and spectroscopy. PhD Thesis, University of California, Berkeley, 2014.

78. Chen, C. On-Surface Synthesis and Local Electronic Structure Characterization of Low-Dimensional Nano-Materials. PhD thesis, University of California, Berkeley, 2018.

79. Zhang, X. Probing Atomic-Scale Properties of Magnetic and Optoelectronic Nanostructures. PhD Thesis, University of California, Berkeley, 2012.

80. Grobis, M. Scanning Tunneling Spectroscopy of Fullerene Nanostructures. PhD Thesis, University of California, Berkeley, 2005.

81. Zwanenburg, F. A.; Dzurak, A. S.; Morello, A.; Simmons, M. Y.; Hollenberg, L. C. L.; Klimeck, G.; Rogge, S.; Coppersmith, S. N.; Eriksson, M. A. *Reviews of Modern Physics* **2013,** 85, (3), 961-1019.

82. Guter, W.; Schöne, J.; Philipps, S. P.; Steiner, M.; Siefer, G.; Wekkeli, A.; Welser, E.; Oliva, E.; Bett, A. W.; Dimroth, F. *Applied Physics Letters* **2009,** 94, (22), 223504.

83. Green, M. A.; Emery, K.; Hishikawa, Y.; Warta, W.; Dunlop, E. D. *Progress in Photovoltaics: Research and Applications* **2012,** 20, (5), 606-614.

84. Frank, D. J.; Dennard, R. H.; Nowak, E.; Solomon, P. M.; Taur, Y.; Hon-Sum Philip, W. *Proceedings of the IEEE* **2001,** 89, (3), 259-288.

85. Schwierz, F. *Nature Nanotechnology* **2010,** 5, 487.

86. van der Lit, J.; Boneschanscher, M. P.; Vanmaekelbergh, D.; Ijäs, M.; Uppstu, A.; Ervasti, M.; Harju, A.; Liljeroth, P.; Swart, I. *Nature Communications* **2013,** 4, 2023.

87. Bennett, P. B.; Pedramrazi, Z.; Madani, A.; Chen, Y.-C.; de Oteyza, D. G.; Chen, C.; Fischer, F. R.; Crommie, M. F.; Bokor, J. *Applied Physics Letters* **2013,** 103, (25), 253114.

88. Blankenburg, S.; Cai, J.; Ruffieux, P.; Jaafar, R.; Passerone, D.; Feng, X.; Müllen, K.; Fasel, R.; Pignedoli, C. A. *ACS Nano* **2012,** 6, (3), 2020-2025.

89. Han, M. Y.; Özyilmaz, B.; Zhang, Y.; Kim, P. *Physical Review Letters* **2007,** 98, (20), 206805.

90. Prezzi, D.; Varsano, D.; Ruini, A.; Molinari, E. *Physical Review B* **2011,** 84, (4), 041401.

91. Sevinçli, H.; Topsakal, M.; Ciraci, S. *Physical Review B* **2008,** 78, (24), 245402.

92. Xu, Z.; Zheng, Q.-S.; Chen, G. *Applied Physics Letters* **2007,** 90, (22), 223115.

93. Franc, G.; Gourdon, A. *Physical Chemistry Chemical Physics* **2011,** 13, (32), 14283-14292.

94. Ijäs, M.; Ervasti, M.; Uppstu, A.; Liljeroth, P.; van der Lit, J.; Swart, I.; Harju, A. *Physical Review B* **2013,** 88, (7), 075429.

95. Hod, O.; Peralta, J. E.; Scuseria, G. E. *Physical Review B* **2007,** 76, (23), 233401.

96. Bronner, C.; Stremlau, S.; Gille, M.; Brauße, F.; Haase, A.; Hecht, S.; Tegeder, P. *Angewandte Chemie International Edition* **2013,** 52, (16), 4422-4425.

97. Martins, T. B.; Miwa, R. H.; da Silva, A. J. R.; Fazzio, A. *Physical Review Letters* **2007,** 98, (19), 196803.

98. Li, Y.; Zhou, Z.; Shen, P.; Chen, Z. *ACS Nano* **2009,** 3, (7), 1952-1958.

99. Cervantes-Sodi, F.; Csányi, G.; Piscanec, S.; Ferrari, A. C. *Physical Review B* **2008,** 77, (16), 165427.

100. Biel, B.; Blase, X.; Triozon, F.; Roche, S. *Physical Review Letters* **2009,** 102, (9), 096803.

101. Talirz, L.; Söde, H.; Dumslaff, T.; Wang, S.; Sanchez-Valencia, J. R.; Liu, J.; Shinde, P.; Pignedoli, C. A.; Liang, L.; Meunier, V.; Plumb, N. C.; Shi, M.; Feng, X.; Narita, A.; Müllen, K.; Fasel, R.; Ruffieux, P. *ACS Nano* **2017,** 11, (2), 1380-1388.

102. Zhang, H.; Lin, H.; Sun, K.; Chen, L.; Zagranyarski, Y.; Aghdassi, N.; Duhm, S.; Li, Q.; Zhong, D.; Li, Y.; Müllen, K.; Fuchs, H.; Chi, L. *Journal of the American Chemical Society* **2015,** 137, (12), 4022-4025.

103. Carbonell-Sanromà, E.; Brandimarte, P.; Balog, R.; Corso, M.; Kawai, S.; Garcia-Lekue, A.; Saito, S.; Yamaguchi, S.; Meyer, E.; Sánchez-Portal, D.; Pascual, J. I. *Nano Letters* **2017,** 17, (1), 50-56.

104. Hybertsen, M. S.; Louie, S. G. *Physical Review B* **1986,** 34, (8), 5390-5413.

105. Cao, T.; Zhao, F.; Louie, S. G. *Physical Review Letters* **2017,** 119, (7), 076401.

106. Horcas, I.; Fernández, R.; Gómez-Rodríguez, J. M.; Colchero, J.; Gómez-Herrero, J.; Baro, A. M. *Review of Scientific Instruments* **2007,** 78, (1), 013705.

107. Paolo, G.; Stefano, B.; Nicola, B.; Matteo, C.; Roberto, C.; Carlo, C.; Davide, C.; Guido, L. C.; Matteo, C.; Ismaila, D.; Andrea Dal, C.; Stefano de, G.; Stefano, F.; Guido, F.; Ralph, G.; Uwe, G.; Christos, G.; Anton, K.; Michele, L.; Layla, M.-S.; Nicola, M.; Francesco, M.; Riccardo, M.; Stefano, P.; Alfredo, P.; Lorenzo, P.; Carlo, S.; Sandro, S.; Gabriele, S.; Ari, P. S.; Alexander, S.; Paolo, U.; Renata, M. W. *Journal of Physics: Condensed Matter* **2009,** 21, (39), 395502.

108. Deslippe, J.; Samsonidze, G.; Strubbe, D. A.; Jain, M.; Cohen, M. L.; Louie, S. G. *Computer Physics Communications* **2012,** 183, (6), 1269-1289.

109. Zhang, Y.; Brar, V. W.; Wang, F.; Girit, C.; Yayon, Y.; Panlasigui, M.; Zettl, A.; Crommie, M. F. *Nature Physics* **2008,** 4, 627.

110. Zhang, Y.; Zhang, Y.; Li, G.; Lu, J.; Lin, X.; Du, S.; Berger, R.; Feng, X.; Müllen, K.; Gao, H.-J. *Applied Physics Letters* **2014,** 105, (2), 023101.

111. Chen, W.; Madhavan, V.; Jamneala, T.; Crommie, M. F. *Physical Review Letters* **1998,** 80, (7), 1469-1472.

112. Yang, Z.; Yao, Z.; Li, G.; Fang, G.; Nie, H.; Liu, Z.; Zhou, X.; Chen, X. a.; Huang, S. *ACS Nano* **2012,** 6, (1), 205-211.

113. Troullier, N.; Martins, J. L. *Physical Review B* **1991,** 43, (3), 1993-2006.

114. Bernevig, B. A.; Zhang, S.-C. *Physical Review Letters* **2006,** 96, (10), 106802.

115. Keum, D. H.; Cho, S.; Kim, J. H.; Choe, D.-H.; Sung, H.-J.; Kan, M.; Kang, H.; Hwang, J.-Y.; Kim, S. W.; Yang, H.; Chang, K. J.; Lee, Y. H. *Nature Physics* **2015,** 11, 482.

116. Essin, A. M.; Gurarie, V. *Physical Review B* **2011,** 84, (12), 125132.

117. Zheng, F.; Cai, C.; Ge, S.; Zhang, X.; Liu, X.; Lu, H.; Zhang, Y.; Qiu, J.; Taniguchi, T.; Watanabe, K.; Jia, S.; Qi, J.; Chen, J.-H.; Sun, D.; Feng, J. *Advanced Materials* **2016,** 28, (24), 4845-4851.

118. Das, P. K.; Di Sante, D.; Vobornik, I.; Fujii, J.; Okuda, T.; Bruyer, E.; Gyenis, A.; Feldman, B. E.; Tao, J.; Ciancio, R.; Rossi, G.; Ali, M. N.; Picozzi, S.; Yadzani, A.; Panaccione, G.; Cava, R. J. *Nature Communications* **2016,** 7, 10847.

119. Hla, S. W.; Marinković, V.; Prodan, A.; Muševič, I. *Surface Science* **1996,** 352-354, 105-111.

120. Jiang, J.; Tang, F.; Pan, X. C.; Liu, H. M.; Niu, X. H.; Wang, Y. X.; Xu, D. F.; Yang, H. F.; Xie, B. P.; Song, F. Q.; Dudin, P.; Kim, T. K.; Hoesch, M.; Das, P. K.; Vobornik, I.; Wan, X. G.; Feng, D. L. *Physical Review Letters* **2015,** 115, (16), 166601.

121. Pauly, C.; Rasche, B.; Koepernik, K.; Liebmann, M.; Pratzer, M.; Richter, M.; Kellner, J.; Eschbach, M.; Kaufmann, B.; Plucinski, L.; Schneider, Claus M.; Ruck, M.; van den Brink, J.; Morgenstern, M. *Nature Physics* **2015,** 11, 338.

122. Lin, H.; Das, T.; Okada, Y.; Boyer, M. C.; Wise, W. D.; Tomasik, M.; Zhen, B.; Hudson, E. W.; Zhou, W.; Madhavan, V.; Ren, C.-Y.; Ikuta, H.; Bansil, A. *Nano Letters* **2013,** 13, (5), 1915-1919.

123. Chen, J.; Wang, G.; Tang, Y.; Tian, H.; Xu, J.; Dai, X.; Xu, H.; Jia, J.; Ho, W.; Xie, M. *ACS Nano* **2017,** 11, (3), 3282-3288.

124. Fei, Z.; Palomaki, T.; Wu, S.; Zhao, W.; Cai, X.; Sun, B.; Nguyen, P.; Finney, J.; Xu, X.; Cobden, D. H. *Nature Physics* **2017,** 13, 677.

125. Jia, Z.-Y.; Song, Y.-H.; Li, X.-B.; Ran, K.; Lu, P.; Zheng, H.-J.; Zhu, X.-Y.; Shi, Z.-Q.; Sun, J.; Wen, J.; Xing, D.; Li, S.-C. *Physical Review B* **2017,** 96, (4), 041108.

126. Wang, Z. F.; Zhang, H.; Liu, D.; Liu, C.; Tang, C.; Song, C.; Zhong, Y.; Peng, J.; Li, F.; Nie, C.; Wang, L.; Zhou, X. J.; Ma, X.; Xue, Q. K.; Liu, F. *Nature Materials* **2016,** 15, 968.

127. Sessi, P.; Di Sante, D.; Szczerbakow, A.; Glott, F.; Wilfert, S.; Schmidt, H.; Bathon, T.; Dziawa, P.; Greiter, M.; Neupert, T.; Sangiovanni, G.; Story, T.; Thomale, R.; Bode, M. *Science* **2016,** 354, (6317), 1269.

128. Wang, Z. F.; Chen, L.; Liu, F. *Nano Letters* **2014,** 14, (5), 2879-2883.

129. Zhang, Y.; Ugeda, M. M.; Jin, C.; Shi, S.-F.; Bradley, A. J.; Martín-Recio, A.; Ryu, H.; Kim, J.; Tang, S.; Kim, Y.; Zhou, B.; Hwang, C.; Chen, Y.; Wang, F.; Crommie, M. F.; Hussain, Z.; Shen, Z.-X.; Mo, S.-K. *Nano Letters* **2016,** 16, (4), 2485-2491.

130. Ugeda, M. M.; Bradley, A. J.; Shi, S.-F.; da Jornada, F. H.; Zhang, Y.; Qiu, D. Y.; Ruan, W.; Mo, S.-K.; Hussain, Z.; Shen, Z.-X.; Wang, F.; Louie, S. G.; Crommie, M. F. *Nature Materials* **2014,** 13, 1091.

131. Cho, S.; Kim, S.; Kim, J. H.; Zhao, J.; Seok, J.; Keum, D. H.; Baik, J.; Choe, D.-H.; Chang, K. J.; Suenaga, K.; Kim, S. W.; Lee, Y. H.; Yang, H. *Science* **2015,** 349, (6248), 625.

132. Qin, X. R.; Yang, D.; Frindt, R. F.; Irwin, J. C. *Physical Review B* **1991,** 44, (7), 3490-3493.

133. Song, Y.-H.; Jia, Z.-Y.; Zhang, D.; Zhu, X.-Y.; Shi, Z.-Q.; Wang, H.; Zhu, L.; Yuan, Q.-Q.; Zhang, H.; Xing, D.-Y.; Li, S.-C. *Nature Communications* **2018,** 9, (1), 4071.

134. Brar, V. W.; Wickenburg, S.; Panlasigui, M.; Park, C.-H.; Wehling, T. O.; Zhang, Y.; Decker, R.; Girit, Ç.; Balatsky, A. V.; Louie, S. G.; Zettl, A.; Crommie, M. F. *Physical Review Letters* **2010,** 104, (3), 036805.

135. Tersoff, J. *Physical Review Letters* **1984,** 52, (6), 465-468.

136. Efros, A. L.; Shklovskii, B. I. *Journal of Physics C: Solid State Physics* **1975,** 8, (4), L49.

137. Wu, S.; Fatemi, V.; Gibson, Q. D.; Watanabe, K.; Taniguchi, T.; Cava, R. J.; Jarillo-Herrero, P. *Science* **2018,** 359, (6371), 76-79.

138. Wang, Y.; Xiao, J.; Zhu, H.; Li, Y.; Alsaid, Y.; Fong, K. Y.; Zhou, Y.; Wang, S.; Shi, W.; Wang, Y.; Zettl, A.; Reed, E. J.; Zhang, X. *Nature* **2017,** 550, 487.

139. Lin, Y.-C.; Dumcenco, D. O.; Huang, Y.-S.; Suenaga, K. *Nature Nanotechnology* **2014,** 9, 391.

140. Kappera, R.; Voiry, D.; Yalcin, S. E.; Branch, B.; Gupta, G.; Mohite, A. D.; Chhowalla, M. *Nature Materials* **2014,** 13, 1128.

141. Li, Y.; Duerloo, K.-A. N.; Wauson, K.; Reed, E. J. *Nature Communications* **2016,** 7, 10671.

142. Duerloo, K.-A. N.; Li, Y.; Reed, E. J. *Nature Communications* **2014,** 5, 4214.

143. Li, W.; Li, J. *Nature Communications* **2016,** 7, 10843.

144. Massey, J. G.; Lee, M. *Physical Review Letters* **1995,** 75, (23), 4266-4269.

145. Ozaki, T. *Physical Review B* **2003,** 67, (15), 155108.

146. Ozaki, T.; Kino, H. *Physical Review B* **2004,** 69, (19), 195113.

147. Bychkov, Y. A.; Rashba, E. I. *Phys. -JETP Lett.* **1984,** 39, 78.